Available online at www.sciencedirect.com
SCIENCE DIRECT®
Icarus 170 (2004) 365–403
ICARUS
www.elsevier.com/locate/icarus

Traveling waves in the martian atmosphere from MGS TES Nadir data

D. Banfield [a,*], B.J. Conrath [a], P.J. Gierasch [a], R. John Wilson [b], M.D. Smith [c]

[a] *Department of Astronomy, Cornell University, Ithaca, NY 14853, USA*
[b] *NOAA/Geophysical Fluid Dynamics Laboratory, Princeton, NJ 08542, USA*
[c] *NASA/Goddard Space Flight Center, Code 690 Greenbelt, MD 20771, USA*

Received 15 January 2003; revised 13 January 2004

Available online 4 June 2004

Abstract

We have characterized the annual behavior of martian atmospheric traveling waves in the MGS TES data set from the first two martian years of mapping. There is a high degree of repeatability between the two years. They are dominated by strong low zonal wavenumber waves with high amplitudes near the polar jets, strongest in late northern fall and early northern winter. The $m = 1$ waves have amplitudes up to about 20 K, are vertically extended, and occasionally extend even into the tropics. Periods for $m = 1$ range from 2.5 to 30 sols. Much weaker waves were identified in the south, with amplitudes less than about 3.5 K. Traveling waves with $m = 2$ and $m = 3$ are also seen, but their amplitudes are typically limited to less than 4 K, and are generally more confined near the surface. In the north, they are more evident in fall and spring rather than winter solstice, which is clearly dominated by $m = 1$ waves. Some evidence of storm tracks has been identified in the data, with accentuated weather-related temperature perturbations near longitudes 200° to 320° E for both the southern and northern hemispheres near latitude ±65° at the surface. Some evidence was also found for a sharpening of longitudinal gradients into what may be frontal systems. EP flux divergences show the waves extracting energy from the zonal mean winds. When the $m = 1$ waves were strongest, decelerations of the zonal jet of order 30 m/(s sol) were measured. Above 1 scale height, the waves extract energy from the jet predominately through barotropic processes, but their character is overall mixed barotropic/baroclinic. Inertial instabilities may exist at altitude on the equatorward flanks of the polar jets, and marginal stability extends through to the tropics. This may explain the coordination of the tropical behavior of the waves with that centered along the polar jet, consistent with the ideas expressed in Wilson et al. (2002, Geophys. Res. Lett. 29, #1684) and similar to those in Barnes et al. (1993, J. Geophys. Res. 98, 3125–3148). Throughout the year, there exist large regions with the meridional gradient of PV less than zero, but they are strongest near winter solstice. Poleward of the winter jet, the regions of instability reach the surface, equatorward they do not. These regions, satisfying a necessary criterion for instability, likely explain the genesis of the waves, and perhaps also their bimodal character between surface (faster waves) and altitude (slow $m = 1$ waves).

Keywords: Atmospheres, dynamics; Atmospheres, structure; Mars, atmosphere; Meteorology

1. Introduction

We have examined two full Mars years of Mars Global Surveyor (MGS) Thermal Emission Spectrometer (TES) nadir spectra temperature retrievals for evidence of traveling waves (excluding solar-forced tides) in Mars' atmosphere. This analysis is the most complete documentation of the traveling waves in Mars' atmosphere that has been performed to date. Credit for this goes to the unprecedented duration and completeness of sampling by the TES instrument.

The first scientific speculation that Mars' atmosphere may have traveling waves in many ways similar to Earth was by Hess (1950). Leovy (1969) was more quantitative and calculated that baroclinic waves with zonal wavenumbers of 2–4 would have the highest growth rates in midlatitudes in a 2-layer quasi-geostrophic model. He also suggested that the short radiative damping time on Mars would have little influence on the length scales of the waves or their growth rates. Leovy and Mintz (1969) adapted an early General Circulation Model to Mars conditions (without topography), and found traveling waves of length scales similar to those predicted by Leovy (1969). They also found that their modeled traveling waves carried significant angular momentum and heat in the winter hemisphere near solstice, and

* Corresponding author.
E-mail address: banfield@astro.cornell.edu (D. Banfield).

0019-1035/$ – see front matter
doi:10.1016/j.icarus.2004.03.015

in midlatitudes in both hemispheres at equinox. Blumsack and Gierasch (1972) examined the effects of the significant topographic slopes on Mars on the traveling waves. They found that the slopes could reduce both the length scales and growth rates of the most unstable waves. Leovy (1979), motivated by Viking Lander observations, discussed the regularity of the martian waves relative to those on Earth. He suggested that, by analogy with rotating tank experiments, the greater atmospheric stability and smaller size of Mars cause its waves to be far more regular than those on Earth. Pollack et al. (1981), establishing the NASA Ames GCM by updating the general circulation model from Leovy and Mintz (1969) to include topography, found little differences in the transient waves, somewhat in conflict with the predictions of Blumsack and Gierasch (1972). Barnes (1984) used a more accurate representation of the zonal mean state in a quasi-geostrophic numerical model to confirm that zonal wavenumbers of 2–4 are favored. Michelangeli et al. (1987) attempted to model the barotropic instability of the winter polar jets for Mars, finding that waves with zonal wavenumbers of 1 or 2 and periods of 0.75–2.5 sols are favored. These perturbations would be mainly notable away from the surface where an orbital atmospheric sounder would be the ideal instrument for detection. Barnes et al. (1993) reported transient wave results from the next update on the NASA Ames general circulation model. In this, the most complete model description of transient waves, they again confirm the wavenumbers, amplitudes and periods from previous, less sophisticated, models as generally being accurate. In particular, however, their greater vertical resolution allowed a more detailed examination of the spatial structure of the transient waves. They found zonal wavenumbers 1 and 2 dominated the higher altitudes, with 1–4 having significant amplitude near the surface. They also noted that not only did the waves have significant amplitudes along the axis of the polar jets, but also they showed activity at upper levels crossing the equator that was coherent with the more polar waves. Wavenumbers were found to increase slightly away from solstice, and with increasing dust loading. The southern hemisphere winter's transient waves were weaker than those of the north by a factor of 2 or more. Hourdin et al. (1995) noted a seasonal dependence in the variance of surface pressure in the Viking Lander data, and had some success reproducing it with the French LMD GCM. Northern transient wave surface pressure variance showed a two peak structure with a relative minimum at northern winter solstice, the depth of which Hourdin et al. showed to increase with the atmospheric dust opacity. Collins et al. (1996) used the Oxford GCM and Viking Lander data to show that Mars' atmosphere apparently flips between two dominant transient wave modes, one with period near 2–4 sols and the other near 5–7 sols. They demonstrated that the diurnal forcing stimulates the mode flipping.

Concurrent with these theoretical investigations, several spacecraft returned atmospheric data from Mars. Mariner 9 returned both atmospheric spectra and visible images relevant to the question of transient waves. Briggs and Leovy (1974) discuss images of winter cloud forms in the north polar hood which suggest the growth, motion and decay of baroclinic waves, possibly sharpening into fronts. Conrath (1981) identified an atmospheric wave centered on the axis of the northern polar vortex in Mariner 9 IRIS data. Unfortunately, the space–time sampling of that data set did not allow an unambiguous identification. The wave could have either been a zonal wavenumber 2 stationary wave or one of several wavenumber phase speed combinations of traveling waves. The Viking Landers returned several Mars years worth of surface observations filled with evidence of traveling waves. Ryan et al. (1978), Barnes (1980, 1981), and Murphy et al. (1990) analyzed the meteorological data to better characterize the traveling waves. They found surface pressure variations of up to $\sim 5\%$ and periods between 2 and 6 (or more) sols with coherence times of 20 sols or more. Using the wind and pressure variations together allowed them to estimate the scale of the waves, finding wavenumbers of about 1–6, with 2–4 being favored. Murphy et al. (1990) compared results between the two landers and suggested that the wave modes were globally coherent. Tillman et al. (1979) interpreted a small subset of the meteorological data in terms of the passing of a frontal system associated with global-scale traveling waves passing over the lander. Mars Pathfinder, while outfitted with meteorological sensors, landed near the equator near equinox ($L_s \sim 150°$), and hence did not capture the signatures of any significant traveling waves (Schofield et al., 1997). Most recently, Hinson and Wilson (2002) and Wilson et al. (2002) have identified traveling waves from Mars Global Surveyor data. Hinson and Wilson identified a zonal wavenumber 3, 2-sol wave at high latitudes in the southern mid-winter from radio science occultations. Wilson et al. identified two different period (~ 6 and ~ 20 sols) zonal wavenumber 1 waves in northern winter centered along the axis of the polar vortex in TES data and reproduced similar behavior in the GFDL GCM. The long period wave also had significant amplitude extending across the equator to the southern tropics. Their analysis showed the TES data dominated by $m = 1$ waves, while the Viking lander surface pressure analyses typically show wavenumbers $m = 2$–4 being dominant.

These theoretical and observational efforts have taught us much about the nature of traveling waves on Mars and helped us to understand their role in maintaining the general circulation and climate. However, they are very incomplete. Using the Mars Global Surveyor Thermal Emission Spectrometer atmospheric temperature retrievals, we present three dimensionally resolved, unambiguous identifications and quantifications of traveling waves with good seasonal resolution. We will discuss the nature of the data set, the limitations of the retrievals, and the technique we have developed to identify the waves. The waves themselves will be discussed for both the northern and southern hemispheres as they change with season and their asymmetries between the hemispheres. Finally, we will address questions about their

role in heat and momentum budgets, and the instabilities that create them.

2. Data set

This study uses retrieved temperatures from the infrared spectra taken by the TES instrument on the MGS spacecraft. Specifically, the data we have analyzed in this work were taken from when Mars Global Surveyor entered its mapping orbit from March 1999 to February 2003, or two Mars years. This data set is an extended version of that used in Banfield et al. (2003) for forced wave analysis. Details of the data set and its coverage and limitations are discussed in Banfield et al. (2003).

We use observations from both the ascending and descending halves of the orbit, yielding 12 regularly spaced longitudes sampled in half a sol. Thus, ideally waves of zonal wavenumber up to about $m = 5$ can be well described twice a sol, allowing us to resolve even fairly fast-moving waves. In practice, dropouts from limb scans and downlink limitations impact the information content of the data set, reducing it slightly from the theoretical maximum suggested above (i.e., effectively limiting us to $m \leqslant 4$). Perhaps more seriously, they influence the choice of technique in extracting the traveling waves from the data set. Techniques like Fast-Fourier Synoptic Mapping (Salby, 1982; Barnes, private communication, 2003) have the advantage of optimally using the data, casting them onto orthogonal basis functions tuned to the spacecraft ground track. This reduces the noise in the end product analysis. However, they require absolutely regular observations to work, and gaps must be filled in, which is somewhat troublesome in that full orbits are frequently missing in the TES data set. We have instead used a convolution technique which is much more tolerant of data gaps, and still allows waves over ~ 0.6 K to be followed.

We have only used nadir data, which limits the vertical resolution and maximum height of the retrieved temperatures compared to limb scans, but affords better latitudinal resolution. Conrath et al. (2000) detail the algorithm that the TES team used to produce the temperature retrievals that we used in this study. Contribution functions are about 1 scale height deep near the surface, but they become deeper near the top of the domain (~ 0.5 mbar). Thus, the vertical resolution in the nadir temperature retrievals is about 1 scale height near the surface and perhaps almost 2 scale heights at a pressure of 0.5 mbar. This limitation has serious implications for our ability to resolve perturbations in the atmosphere with short vertical wavelengths (e.g., Wilson et al., 2002; Hinson et al., 2003; Banfield et al., 2003).

3. Analysis approach

We have chosen to keep our analysis tools as simple as possible, not only to make them more easily understood, but also to keep the algorithms robust against data dropouts. As mentioned above, significant dropouts occur in the TES data set (several orbits per sol), and this must be considered when designing an analysis algorithm. We have chosen to use binning and averaging to identify the local mean temperatures, analogous to the first part of the analysis in Banfield et al. (2003). Once we have removed the local mean temperatures and are left with the local temperature anomalies, we have used a correlation technique to identify traveling waves. The techniques described here were also used in the analysis in Wilson et al. (2002).

3.1. Local mean temperatures

The first phase of the analysis focuses on that portion of a given location's temperature signal that is fixed in time, or slowly varying on a seasonal timescale. This was the subject of the analysis in Banfield et al. (2003), in which the zonal mean temperature as well as the lowest wavenumber stationary waves and some specific thermal tides were quantified. While in the previous work we were interested directly in the mean fields, in this work we will simply subtract them from the observations to yield the local temperature anomalies from the means.

As in Banfield et al. (2003), we combined the data into bins in latitude, longitude, pressure level, and whether the observations were taken at 2 AM or 2 PM. Again, we used 4° wide bins in latitude totaling 45 bins, 30° wide bins in longitude totaling 12 bins, half-scale height wide bins in pressure totaling 8 bins, and one bin for 2 AM observations and one bin for 2 PM observations. This choice of bin sizes, the exact same as that used in Banfield et al. (2003) proved to be quite capable of well defining the mean states and the lowest zonal wavenumber stationary waves and tides, where essentially all of the power resides.

To resolve the traveling waves, we further binned the results in half sol bins. Binning the results in short time increments like this was unnecessary for the analysis in Banfield et al. (2003) as that work focused on the means themselves, but this work relies on the time dependence of the anomalies from the means. Choosing a time resolution of half a sol involved a trade off between longitudinal resolution and temporal resolution. If we had used a shorter time than half a sol, then the spatial resolution would not only be irregular in longitude for each time interval, but also would not have even 12 independent longitudes observed. This would clearly compromise the maximum zonal wavenumber that we would be able to resolve, as well as introduce possible aliasing problems due to the missing longitudes. Choosing a binning time longer than half a sol would have reduced our temporal resolution further than necessary, which would have reduced the maximum phase speed wave that we could resolve. Thus half a sol time bins are the optimal choice among these tradeoffs.

Discretizing the maps to once every half sol will introduce problems for waves with periods less than or of order

1 sol. Because the observations are not taken globally instantaneously every half sol, but rather serially over the full half a sol, we are moving some observations by up to a quarter sol in time. But for waves with periods well removed from 1 sol, the effects are negligible. From our experience with the data set, the traveling waves' periods are significantly longer than a sol, and their representations are minimally perturbed by discretizing them in half a sol increments. To verify this, we tried performing our analysis with quarter sol timesteps, with negligible differences.

To define the local means, we computed a running mean of 50 sols centered on the time of interest. This was chosen to minimize the effects of seasonal trends, while still including enough observations to produce a statistically meaningful average and also to smooth over slowly moving waves. Our experience showed that waves with period of as long as about 20 sols are present in the martian atmosphere, and thus averaging for shorter than that would inadvertently remove those slow waves from consideration. With the local means so defined, we removed them from each timestep over all of the bins to yield a local temperature anomaly. The final step was to recombine the day and night anomalies into one, since presumably the effects that distinguish day from night were removed in defining the local means. This leaves the local temperature anomalies in bins of only latitude, longitude, pressure and time for further analysis to extract the traveling waves.

3.2. Identification of traveling waves

Once we have removed the local means from a temperature signal, we are left with the temperature anomalies which include the traveling wave perturbations we are interested in as well as noise. Furthermore, we do not know a priori what zonal wavenumber or phase speeds to expect. We have to determine these from the data. Because we are searching for waves that migrate predominately in the zonal direction, we examine each bin of latitude and pressure independently looking for the specific longitude-time dependence characteristic of a traveling wave. We do this by convolving (in longitude and time) the data with sine waves of varying zonal wavenumber and phase speed, and identifying those combinations with the highest covariance. Only after we have done this do we compare again between latitudes and pressures to look for spatial coherence meridionally and vertically. Results presenting accord in these directions will then increase the confidence in the results, particularly as different latitude bins will be examining data sets completely independent of one another. To describe this more fully, we will follow one latitude and pressure bin through processing.

3.3. Each latitude and pressure

We have selected the latitude 64° N, and the pressure level of 3.0 scale heights above 6.1 mbar (i.e., 0.3 mbar) to demonstrate the analysis. For clarity of the figures, we will limit the time of interest to $L_s = 200°$–$300°$, northern fall and winter when traveling waves are likely strongest at this location. Note also that this is the time and region focused on in Wilson et al. (2002). Figure 1a shows the data in the form of a Hovmoller diagram, that is longitude versus time, with temperature anomaly indicated by brightness. The limitation of 12 longitude bins is quite evident in this figure, making it somewhat hard to see the structure buried in the data. The much smaller time bins (half a sol) are less of a problem, especially for the slow waves that are present in this data subset. There are also some regions of missing data in this plot, which show up as pure black.

In this region, there are actually quite evident zonal wavenumber 1 waves traveling eastward with at least two distinct phase speeds at different times. The higher zonal wavenumbers are relatively minor in this data subset. To better visualize the waves, we have fit a zonal wavenumber 1 wave to each individual timestep, and rendered that with increased longitudinal resolution for each timestep. This appears as Fig. 1b. A slowly moving $m = 1$ wave is quite evident from $L_s \sim 240°$ to $L_s \sim 270°$, at which time the phase speed of the dominant $m = 1$ wave greatly increases. There is also evidence of a faster $m = 1$ wave before $L_s \sim 225°$. The slow wave has a period of about 18–30 sols, while the faster waves have periods of about 6 sols. The slow wave remains coherent over a time of about 50 sols, while the faster waves appear to be coherent for somewhat shorter times. Amplitudes of the slow wave are about 14 K, while those of the faster waves are about 10 K or less.

In the discussion above, we identified the waves visually by tracking the maxima with longitude and time. Our software does the same process, by convolving the data with a unit amplitude synthetic wave of a given zonal wavenumber, and a set of phase speeds. The software tries all phase speeds between the fastest westward phase speed that can be resolved, through zero (stationary), to the fastest eastward phase speed that can be resolved. These limitations on the phase speeds that can be resolved are set by the zonal wavenumber and the interval between maps. A zonal wavenumber 1 wave ($m = 1$) imaged every half sol would be well resolved up to about $\pm 180°$ of longitude per half a sol, or $\pm 360°$/sol (a period of 1 sol). For speeds exceeding this, the wave would alias into a slower wave. For higher zonal wavenumbers, the phase speed limits are more stringent, as the shorter wave would not need to propagate as far to cause ambiguity.

The synthetic traveling wave is convolved with the data over the specified interval, centered on the time in question. For longer intervals, the phase speeds of waves in the data can be more precisely determined. However, if the interval exceeds the coherence time of the waves, the convolution will be reduced. The balance between these two competing processes was found empirically with our analysis. We used an interval of 20 sols for $m = 1$, 17 sols for $m = 2$, and 15 sols for higher zonal wavenumbers, affording the best combination of precision in phase speeds and flexibility to

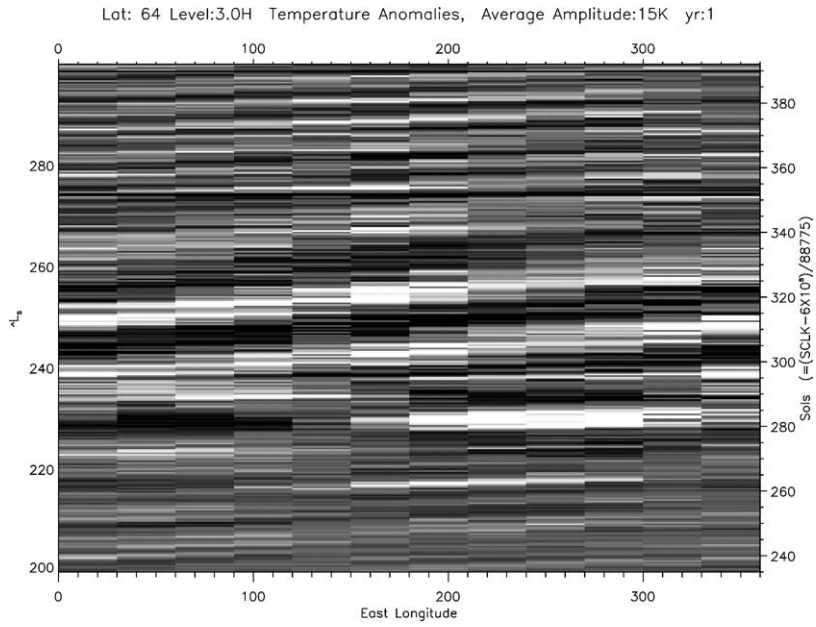

(a)

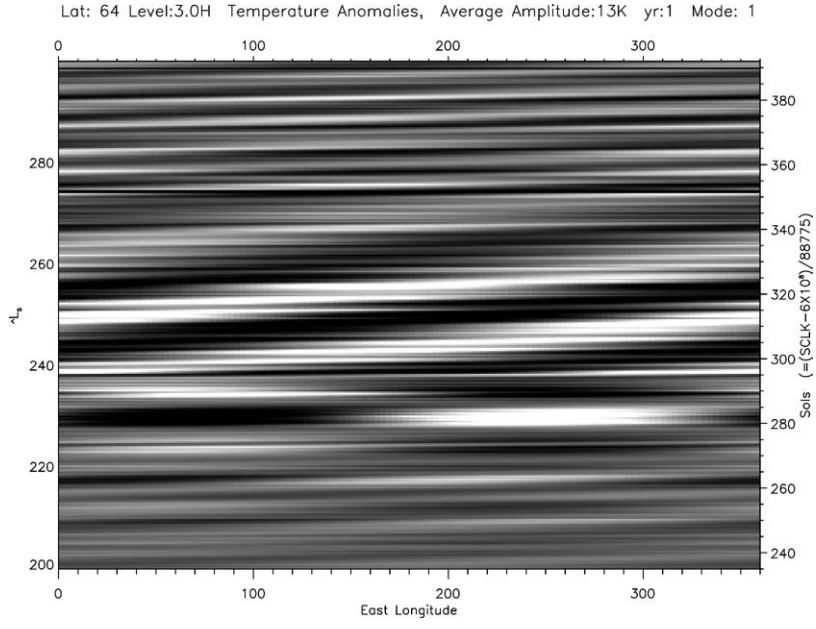

(b)

Fig. 1. Hovmoller diagrams for 64° N, 3 scale heights altitude for $L_s \sim 200°$–$300°$ of the first MGS mapping year. These plots show the time dependent temperature perturbations (bright = warm, dark = cool) as a function of longitude and time for a specific altitude and latitude. The average amplitude over this time is indicated in the title of the figure, in this case, 15 K. The right abscissa counts sols from an arbitrary starting time. It is the MGS SCLK spacecraft clock time -6×10^8 s/88775 s/sol. The left abscissa, L_s, is more useful, but is slightly imprecise due to the eccentricity of Mars' orbit. The zonal mean temperature and the stationary waves have been removed. (a) The raw data, binned into 12 longitude bins. (b) Only the zonal wavenumber 1 component of the data at each timestep. Note the long period eastward propagating wave around $L_s \sim 250°$, and a faster wave after about $L_s \sim 274°$. There are also indications of a standing wave at about $L_s \sim 230°$. Note that the $m = 1$ waves alone have an average amplitude of 13 K (compared to 15 K for all waves here).

capture short coherence time waves. This interval also determined the number of separate phase speeds that need be tested between the extremes. If two phase speeds differ by so little that over the convolution interval, their synthetic waves differ in phase by less than the width of a longitude bin, then they are essentially the same speed to our level of resolution. We have used this criterion to choose the number of phase speeds tried with the data, limiting the total number to 73 individual phase speeds for computational efficiency. This has proved to well resolve all of the observed waves.

Figure 2 shows an array of these synthetic waves convolved with the data from Fig. 1. Again, time increases up the right-hand side (with the approximate L_s indicated on the left), but the abscissa is now phase speed. Contoured

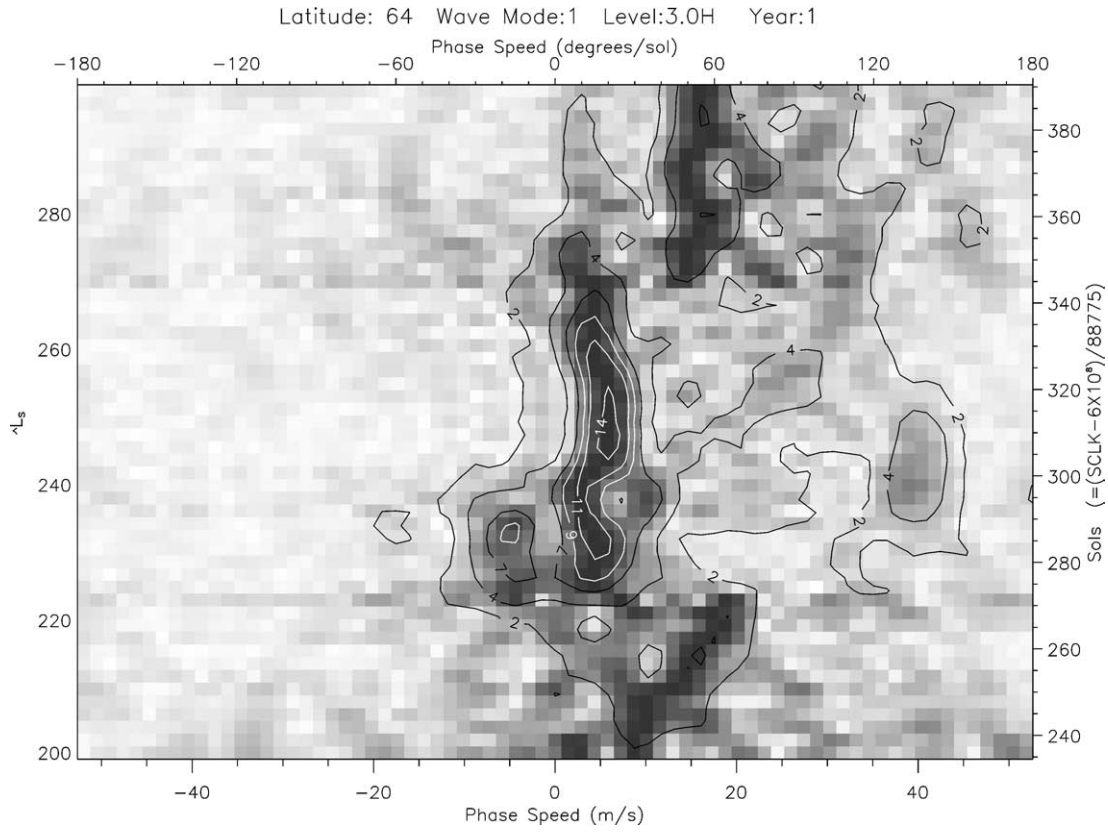

Fig. 2. Plot showing the amplitude of the $m = 1$ waves from Fig. 1 as a function of time and phase speed. See the text for details of this processing. Relative amplitude is indicated by the grayscale (dark = relatively high amplitude). Absolute amplitudes are indicated by the contours, labeled at 2, 4, 7, 9, 11, and 14 K. The wave reaches its maximum amplitude around $L_s \sim 250°$, with an eastward phase speed of about 20°/sol or a period of 18 sols. Note the jump in phase speed at $L_s \sim 273°$, also evident in Fig. 1.

throughout the field is the convolution of the synthetic waves with the data, which is representative of the amplitude of the waves present in the data with each phase speed for this zonal wavenumber ($m = 1$), averaged over the convolution interval. The gray scale is also the magnitude of the convolution, but in this case scaled by the maximum at each time interval. This highlights the dominant phase speed at each timestep, without letting those times with smaller overall wave amplitudes become swamped by the times with large amplitude. In this case, it is very interesting to note that the phase speed appears to decrease from $L_s \sim 240°$ to $L_s \sim 273°$, at which time it is about 10°/sol, or a period of 36 sols. Then there is an abrupt jump in phase speed at about $L_s \sim 273°$ to a phase speed of about 54°/sol, or a period of 6.7 sols. This transition, and the slow wave were the subject of the Wilson et al. (2002) work. It is interesting to note also that from $L_s \sim 220°$–$240°$ there is amplitude in a westward traveling wave with a phase speed almost exactly opposite to the eastward traveling wave. This is indicative of a standing wave, which is evident in Fig. 1 during this time. There are also several other instances of significant amplitude at other phase speeds beside the dominant ones mentioned. We will not generally discuss these secondary maxima in the convolutions any further, but they quite likely warrant further attention. Some of the cases where secondary maxima are present are analogous to the findings in Wilson et al. (2002) where they note fast and slow $m = 1$ waves co-existing near the surface. We will give these more attention.

At $L_s \sim 200°$, the dominant $m = 1$ wave's amplitude is ~ 2 K, but at its maximum it is about 16 K. Then, during the time in which it transitions abruptly to the faster (6 sol) wave, its amplitude sharply drops to about 3 K, then grows again to over 7 K by $L_s \sim 300°$. The secondary maxima have amplitude in this plot at times of over 4 K, while the noise level in the plot is less than about 1 K. Clearly, the maxima are well identified in phase speed and amplitude, and the secondary maxima are also quite likely significant. Our experience with this technique suggests that local maximum amplitudes of about 0.6 K or more are statistically significant. Of course, our ability to identify a wave depends on its steadiness and coherence time in addition to its amplitude.

The complex part of the convolution yields the phase of the wave. This detail is not important when examining only one latitude and pressure, but becomes quite interesting when comparing between latitudes and pressures.

3.4. Comparing among latitudes and pressures

To understand the spatial distribution of the amplitudes of the waves, their phase speeds, and (where they are co-

herent) their relative phases, we have to compare the results discussed above between different latitudes and pressures. For simplicity, we concentrate on only one particular wave phase speed for each latitude and pressure. We have chosen to distill each latitude and pressure to its dominant phase speed, defined by the greatest average amplitude over a specified time interval. This time interval must be chosen with some care. It must be short enough that variations due to the changing seasons, changing dustiness, or the vacillations of the waves themselves are adequately captured. However, it must be long enough to yield a manageable number of results, and also allow enough time to identify the traveling waves well. To achieve this, we have used a averaging interval of 30° of L_s, or about 60 sols. This is one third of a season, roughly the timescale for the effects of a dust storm to occur, and only a little longer than the coherence time of the waves we have observed. Its also about 3–4 times as long as the typical time we have used for convolving the synthetic waves with the data. Finally, it yields 12 visualizations of the traveling wave structure per year. This results in relatively complex but still readable plots.

Defining the dominant phase speed as that which has the maximum average amplitude over the time interval usually yields a good result, but occasionally, the results are poorly defined. If the maximum average amplitude is only marginally above the noise on the collection of average amplitudes for the different phase speeds, we discard the results from that cell entirely. Specifically, we compute the mean and standard deviation of the average amplitudes for all the different phase speeds. If the ratio of the difference between the maximum amplitude and the mean amplitude to the standard deviation of the amplitudes is less than about 1.4, then we consider that cell as having inconclusive results, and it is not included in the output. While these cases are relatively rare, performing this filtering insures robust results.

Rather than concentrate on the locally dominant phase speed, we could have chosen to follow the dependence of a *particular* phase speed across the meridional plane. However, in regions where the wave with this phase speed is a minor perturbation, this could be misleading. Because this work is focused on cataloging the main effects of the traveling waves, it is best to identify each cell by its locally dominant wave. The alternative could be a good choice if we were particularly interested in, e.g., the 20 sol wave discussed above. We will leave this type of analysis to later works.

Figure 3 presents the amplitude and period of the dominant waves over the meridional plane for $L_s = 225°$–$255°$. This time interval is a subset of that shown in Figs. 1 and 2, when the traveling wave at 64° N had a period of about 20–36 sols. Rather than present the phase speed itself, for the long periods of the $m = 1$ wave the period is more convenient to read. However, the actual phase speed (in m/s) is still valuable in identifying a steering level for the wave (comparing against the zonal mean winds). This form of plot represents the building block of many of the plots to follow, showing information on the meridional plane realized over many fractions of a martian year. We chose to blank regions with amplitude below 0.66 K because for amplitudes below that the fits are much more tenuous, and noise becomes a serious issue. For most regions with a fit amplitude of greater than about 0.66 K, the results are significant, except perhaps very near the surface where noise is larger. In this particular example, the maximum temperature amplitude is just over 12 K, at a pressure of about 0.3 mbar and latitude about 66° N. The region of largest amplitudes is centered on the polar front, and a region of significant amplitude and identical period extends all the way to south of the equator at the highest altitudes in our domain. The tropics, while less than 1 K in amplitude, are actually dominated by the same period wave as along the polar front. The color appears different here only because the wave's amplitude with time behaves differently in the tropics than along the polar front, thus causing a different period to dominate there over this full interval from the time changing period of this wave. Because all of these regions are dominated by the same wave, they are thus spatially coherent.

In the bottom half scale height of our analysis, there are regions that are not coherent with the broad wave at altitude. These near surface locations are the most difficult to retrieve accurately with TES, but they might also hold the most information about traveling waves confined to near the surface. Their interpretation must be done with care and in consideration of the difficulties associated with their retrievals. Wilson et al. (2002) used the GFDL GCM to aid in interpreting TES results in the bottom scale height. For the other regions of the map, where the amplitude is between 0.6 and 1 K, we are hesitant to call them noise, as there are spatial correlations found in the dominant wave periods, and the filter on the significance of the maximum average amplitude does not generally discard them. Nevertheless, the amplitudes are small enough that the effects of these possible waves are likely negligible. We will ignore them in this analysis, concentrating on waves with amplitude of at least 1 K or more.

We now examine the relative phase of the dominant wave between locations. This is of interest to understand the heat and momentum transports of the wave across the meridional plane. With that we can address the waves' effects on the general circulation and perhaps gain some insight into wave sources and sinks. We compute the relative phases for waves moving with the same phase speed as that at the location of maximum amplitude. In this case, that location is 66° N and about 0.3 mbar. We then compute the average phase difference between the wave at that location and all other locations for that specific phase speed. We can measure the relative phase even beyond the regions dominated by the maximum amplitude wave, but we refrain from displaying those results as more cautious interpretation must be exercised. We will however occasionally discuss these results beyond those shown on the plots. The relative phases in the region dominated by the same speed wave as the location of maximum amplitude is shown in Fig. 4.

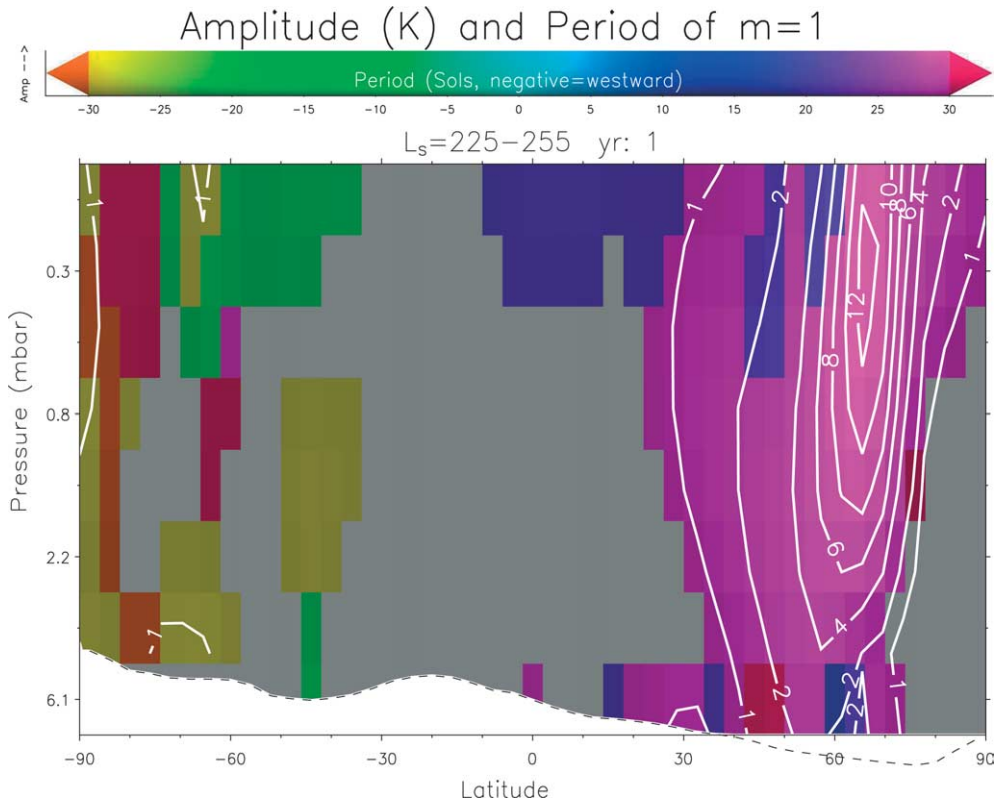

Fig. 3. Meridional cross section of $m = 1$ wave amplitude and dominant period for $L_s \sim 225°$–$255°$ of the first MGS mapping year. The abscissa runs from the south pole to the north pole, and the ordinate covers 4 scale heights, with 6.1 mbar at the bottom followed by 3.7, 2.2, 1.4, 0.8, 0.5, 0.3, and finally 0.18 mbar. Surface pressure for this season is indicated by the dashed line at and below the bottom of the plot. Amplitude is indicated by contours and brightness (bright = high amplitude). Contour levels are at 1, 2 K and even values above this. Amplitudes below 0.66 K appear gray on this plot, as they are not considered significantly above the noise. Colors indicate the dominant period of the $m = 1$ wave over this interval. A period scale bar appears at the top. Negative values are westward propagating waves, appearing as colors orange–green–light–blue. Positive values are eastward propagating waves, appearing as colors light blue–purple–red. Note the concentration of the wave amplitude along the polar front in the north. Throughout this region the dominant period is consistently 20–36 sols.

In this particular example, for $L_s \sim 225°$–$255°$, the location of maximum amplitude is 66° N, 0.3 mbar. The relative phase advances to the east for locations south and below the maximum, indicated by colors progressing to a deeper blue. These indicate a relative phase of up to almost 90° E for 36° N, 1.3 mbar. For locations south and higher than the maximum, the relative phase first regresses westward (green hues), then further south advances eastward again (not shown because the amplitude goes below our cutoff for certain significance of the results). At 45° N, 0.18 mbar, the relative phase is about 30° W, but farther south at 20° N, 0.18 mbar where the amplitude has dropped below 1 K, it has advanced to about 90° E. In the equatorial region, the phase continues to advance eastward descending in the tropics. Near the equator, at the top of our domain, the relative phase is about 140° E, while below that, it has advanced all the way around to a relative phase of about 90° W at 2.2 mbar over the equator, below which the results become questionable. Wilson et al. (2002) also noted this coherent extension of the (slow) traveling wave down into the tropics, and confirmed the results using TES limb data and the GFDL GCM.

This westward phase shift with increasing latitude that is evident between 30° and 60° N (except at the highest altitudes) is indicative of an equatorward momentum transport by these waves. Additionally, the slight westward phase tilt with height that is evident in that same region is indicative of a poleward heat transport. We will address both of these topics more fully later.

4. Results with season

The only further variable that needs to be addressed to complete the description of the traveling waves throughout the TES data set is the progression of seasons. As mentioned above, we first analyzed each latitude and altitude separately, then compared amplitudes, phase speeds and relative phases among them for 30° L_s bins. Breaking the data up into bins of $L_s = 30°$ was necessary to produce a readable figure, but occasionally it forced averages over intervals in which we know the waves dramatically change their character. In these cases, we will go back and use other types of plots to examine the quick changes in more detail. The composite plots will be comprised of 12 panels of the same format as those

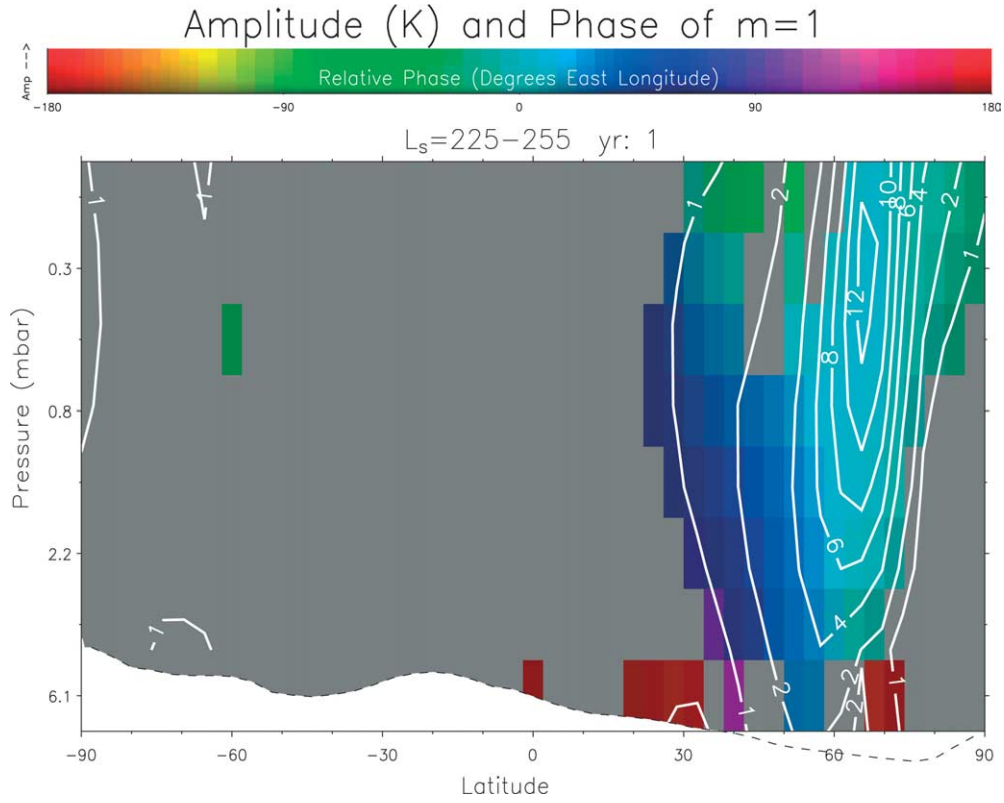

Fig. 4. Similar to Fig. 3, but instead showing the relative phases of the $m = 1$ waves for $L_s \sim 225°$–$255°$ of the first MGS mapping year. Again, contours and brightness indicate wave amplitude, but here color represents the average phase of a particular latitude and altitude relative to the location with the maximum amplitude. The color bar at the top gives the actual relative phases in terms of east longitude. A value of $+90°$ at a particular location means that the wave's maximum is found on average 90° of longitude east of where the wave's maximum is for the location of maximum amplitude. Values are only shown for places that were dominated by the same period wave as that of the location with the maximum amplitude, but careful analysis is still possible outside of these regions. Note the westward phase tilt with height near 50° N.

appearing in Figs. 3 and 4 with season progressing between panels. The discussion of the last section should serve as an introduction to the fundamentals of the more complex composite plots that follow.

We will address each zonal wavenumber in turn, up to zonal wavenumber 3. While this separate analysis for each zonal mode is mathematically and often physically convenient, it is awkward in cases of zonal modulation (storm tracks) or frontal systems. In these cases, there is a relationship between the phase speeds and amplitudes of different zonal wavenumbers, creating the different, non-sinusoidal behaviors. These phenomena will not be as obvious with our analysis approach, but we will return later to address cases where they occur.

4.1. Zonal wavenumber 1

Figure 5 shows the amplitude and period of the locally dominant waves as meridional cross sections for the first year of MGS mapping (from L_s 105°–360°–105°). We will discuss the most significant $m = 1$ traveling waves seen in the first mapping year's data, and also a few specific intervals where smaller amplitude, but still significant $m = 1$ traveling waves are also evident. We will then use the second year's data to assess interannual variability.

4.1.1. First year

Starting in the northern hemisphere, at $L_s = 105°$–$135°$ (upper left of Fig. 5), there is an ~ 11 sol wave (the period is poorly defined then) with a maximum amplitude of about 1.2 K centered at about 80° N. By $L_s \sim 140°$ this wave has shortened its period to about 6.5 sols. Its amplitude then falls below 1 K by $L_s \sim 165°$.

During northern fall equinox, there are two significant waves, one near the top of our domain, centered about 50° N, and the other in the lowest scale height of the atmosphere between 60° and 80° N. The high altitude one has a very long period of more than 30 sols, and an amplitude that exceeds 2 K at 50° N and 3.5 scale heights altitude. Interestingly, it appears to be echoed in the southern hemisphere (near 50° S) at this time, with the same period, and only slightly smaller amplitude, suggesting a globally coherent mode. By $L_s \sim 225°$, this wave has broken away from its partner in the southern hemisphere, and abruptly sped up, becoming a 4 K, 7-sol wave before it dies out at about $L_s \sim 225°$ (see bottom of Fig. 2). Meanwhile, the wave near the surface has a period of about 10 sols at equinox and a maximum amplitude of just

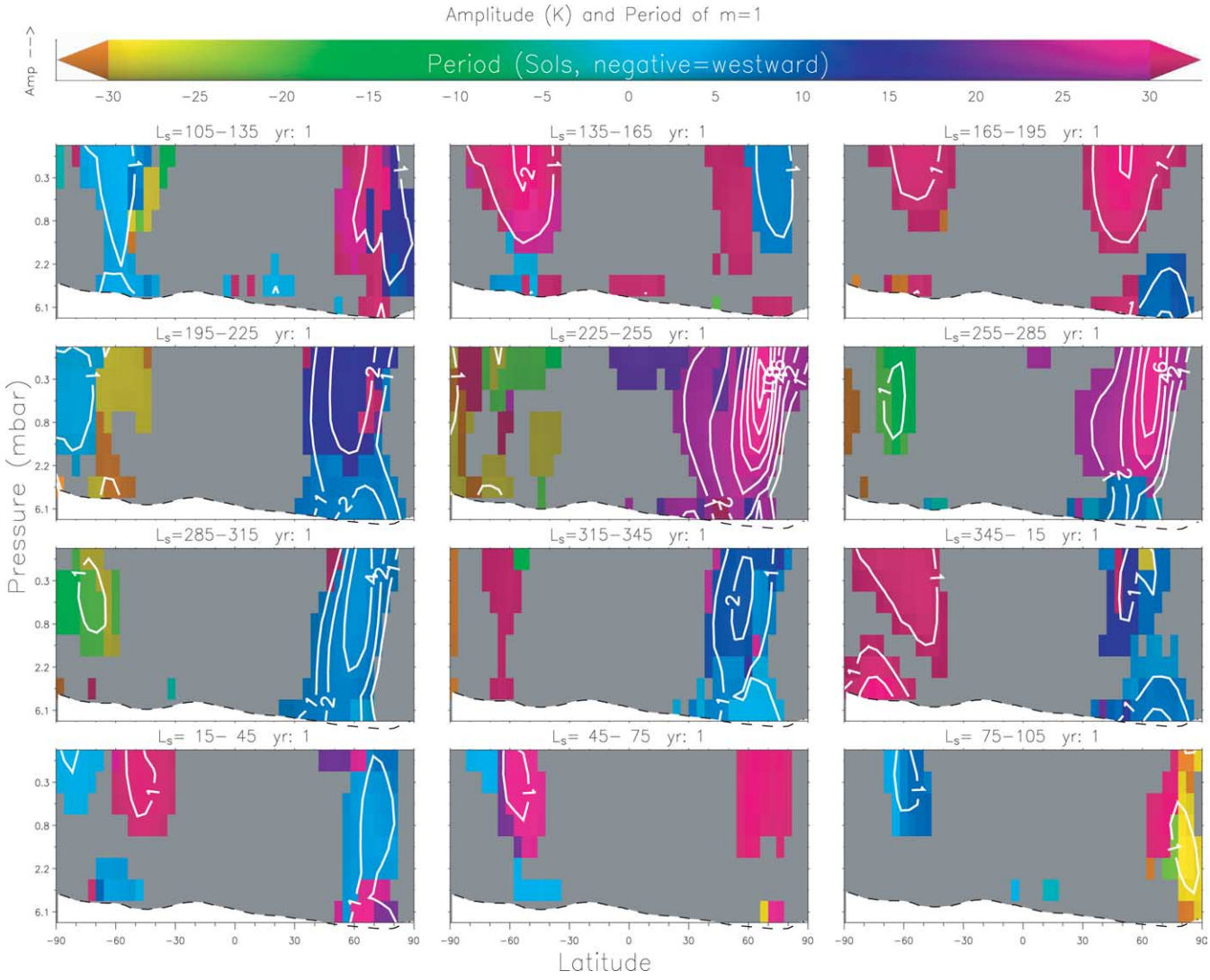

Fig. 5. Amplitude and period of the $m = 1$ wave during the first MGS mapping year. Each panel is like Fig. 3, but for a different 30° L_s bin. Time advances from left to right, then down in this plot. The equinoxes and solstices appear in the right column, with northern fall, winter, spring and summer reading downward. Note the very large waves along the northern polar front in late fall-winter, and their relatively long periods. Note also the small amplitudes in the south, occasionally with westward propagation during southern summer.

over 2 K, but it is strengthening and also slightly speeding up with time. By $L_s \sim 195°$–$225°$, its period is about 7 sols and its maximum amplitude exceeds 3.5 K. Still it is confined to the lowest scale height of the atmosphere, and between the pole and about 30° N. After $L_s \sim 225°$, the faster wave near the surface also disappears.

At about $L_s \sim 225°$, when the two northern hemisphere waves mentioned above die out, another wave appears and quickly grows in strength. This one dominates the whole region of the polar vortex, from the surface to the top of our domain, from 30° to 80° N. This wave, with a period varying between 20–36 sols is the same wave discussed above, particularly in Figs. 2, 3, and 4. It is sharply concentrated along the polar vortex, with the largest amplitudes about 3 scale heights above 64° N, and amplitudes nearly as large at the top of our domain. It quickly grows to over 14 K at $L_s \sim 250°$, then gradually declines until about $L_s \sim 273°$. The behavior is complicated in this region with evidence of both the 20–36 sol wave and a 2.7 sol wave present above 1 scale height (see Figs. 1b and 2). There is also clear evidence of a standing wave with a $\sim$ 18 sol period from $L_s \sim 225°$–$240°$. This is likely related to the dust storm that started at just this time (Smith et al., 2001a).

By about $L_s \sim 260°$ however, a fast (7 sol) wave returns near the surface and dominates from then on through the northern winter. From $L_s \sim 260°$ to $L_s \sim 273°$, only the bottom scale height shows evidence of this faster wave, the rest of the polar vortex region still being dominated by the slow wave. Then, abruptly at $L_s \sim 273°$, the bulk of the polar vortex region rapidly switches to being dominated by the faster (7 sol) wave that first returned at the surface. This transition was examined in some detail in Wilson et al. (2002).

The faster (7 sol) wave evident after $L_s \sim 273°$ is dominant and strong over much the same region as was the slow

wave (i.e., the polar vortex). Its maximum grows from 4 K to above 7 K by $L_s \sim 294°$, then it drops back down to 4 K and below by $L_s \sim 307°$. Eventually, by $L_s \sim 310°$, this wave is no longer dominant and several $m = 1$ waves with various periods are found in the vicinity of the polar vortex; different ones dominating in different regions. Above about 1 scale height, on the equatorward side of the polar vortex, a slow wave with an 11-sol period is dominant. The maximum amplitude of this dominant wave has dropped to 1–3 K, and is located slightly equatorward of where upper level maxima were earlier during northern winter (i.e., 54° N versus 66° N). Slightly more poleward and below this slow wave, the faster wave (now about 6 sols) is still dominant. Closest to the surface on the poleward edge of the polar front there is a very fast wave, with a period of about 2.4 sols that becomes dominant after $L_s \sim 320°$ (see Fig. 6). This very fast wave is likely related to a stronger (3 K versus 2 K) $m = 2$ wave in the same region with half the phase speed, creating a frontal shape and zonal modulation or a storm track (e.g., Figs. 14b and 20). Both the $m = 2$ and the fast $m = 1$ waves near the surface slow down from $L_s \sim 330°$ to $L_s \sim 345°$, eventually abruptly disappearing after reaching a period of 3 sols. They are almost immediately replaced by an $m = 1$ wave with a period of 7 sols and an amplitude of 4 K. A related $m = 2$ wave then has the same phase speed, causing zonal modulation in the wave (e.g., Fig. 20). Meanwhile, the slower wave at altitude grows weaker and slower with a period near 13 sols in some regions, while in other regions a westward wave is dominant, but the low amplitudes make it difficult to be conclusive at this region and time. This wave drops below 1 K amplitude by about $L_s \sim 360°$.

The 7 sol wave nearest the surface speeds up to about a 5 sol period at $L_s \sim 5°$, then slows again to 14 sols by $L_s \sim 30°$. After this, it steadily weakens, dropping below 1 K by $L_s \sim 40°$ maintaining the long period of 14–18 sols. A very weak ($\sim$ 1 K) 7 sol wave is evident in the upper 3 scale heights of our domain from 60° to 80° N between about $L_s \sim 20°$–45°.

Finally, during northern summer solstice, a westward traveling wave with amplitude just over 1 K and a period of roughly 28 sols is evident from 1 to 3 scale heights above 80° N to the pole. This is the last of the northern traveling wave $m = 1$ activity during the first year.

Turning now to the southern hemisphere, at $L_s \sim 105°$–135° the overall dominant zonal wave 1 is that located along the southern polar jet, namely between about 50° and 75° S. In this region, the wave amplitude is between 1 and 2 K (peaking at about 1.9 K) with a period of $\sim$ 3.5 sols. This wave persists until about $L_s \sim 145°$, but is gradually replaced by a much slower wave with a period of about 30 sols that builds starting after $L_s \sim 135°$ to a maximum amplitude of about 3 K (see Fig. 7). The slow wave is localized higher (above 1.5 scale heights) and slightly equatorward (to about 40° S) of the faster wave. There is also a hint of the slow wave being present throughout the tropics at and below about 2 scale heights altitude. The slow wave remains above 1 K and gradually slows, eventually becoming a westward propagating wave after about $L_s \sim 190°$. From $L_s \sim 140°$–185°, the northern hemisphere also shows this same period wave, in phase between the two hemispheres, making it a global mode. After $L_s \sim 185°$, the northern wave speeds up, breaking from the southern wave. The southern wave weakens to roughly 1 K and becomes a faster westward wave, attaining a period of 18 sols by $L_s \sim 230°$. After this, its center of activity shift slightly lower and poleward to 2.5 scale heights above 66° S (see Fig. 8). The amplitude in this region remains just above 1 K from $L_s \sim 255°$–300°, while the period shortens from 24 sols to a minimum of 8 sols westward (at $L_s \sim 278°$). After this time the wave slows again, falling below 1 K as it becomes nearly stationary.

Meanwhile, at $L_s \sim 210°$, a high latitude southern hemisphere $m = 1$, 3-sol wave grows above 1 K amplitude. This wave is centered at about 80° S, above about 1 scale height altitude, and extends as far north as 70° S. By $L_s \sim 230°$, this wave has again receded below 1 K amplitude.

There is an interesting connection between the growth times of the westward waves and the presence of both standing waves and dust storms. At $L_s = 225°$, there are both westward and eastward propagating 20 sol waves evident at 66° S (Fig. 8). The eastward wave diminishes quickly (20 sols), while the westward wave continues on. Strikingly similar behavior occurs simultaneously in the north at 64° N (Figs. 1 and 2) (although there the eastward wave persists). This time also marks the occurrences of a large regional dust storm in the southern hemisphere in the first mapping year of TES. Specifically, one occurred at $L_s = 225°$ and another at $L_s = 309°$ (Smith et al., 2001a); although only the earlier one seems to have generated significant westward traveling waves. Another regional scale dust storm occurred at $L_s = 190°$ of that year, which coincides very well with the first evidence of the westward traveling wave in our data.

The next evident traveling wave in the southern hemisphere during the first TES mapping year occurs at $L_s \sim 345°$ with a very long period, roughly 50 sols. It eventually reaches over 3 K at $L_s \sim 0°$, then dies out sometime after $L_s \sim 10°$ (during a data dropout). This wave is strongest near the surface at 70° S, but also has a region above 1 K above and equatorward (to 40° S) of a diagonal line running from the surface at 45° S to 3 scale heights altitude at the south pole. After the data dropout, the wave is mainly found at altitude, 2–4 scale heights above 30° to 60° S. Here, the wave is just barely over 1 K from $L_s \sim 30°$–105°, and varies quickly in period from very long period westward to as fast as a 6-sol eastward wave. Presumably this eventually corresponds to the short period high latitude wave seen at $L_s = 105°$–135° of the first year discussed above. There is a very notable difference between the strengths of the $m = 1$ waves in the northern winter versus those in the southern winter. While $m = 1$ traveling waves definitely are found in each hemisphere's winter, those in the south have amplitudes always less than 2 K during this year, while those in the north exceeded 12 K at times.

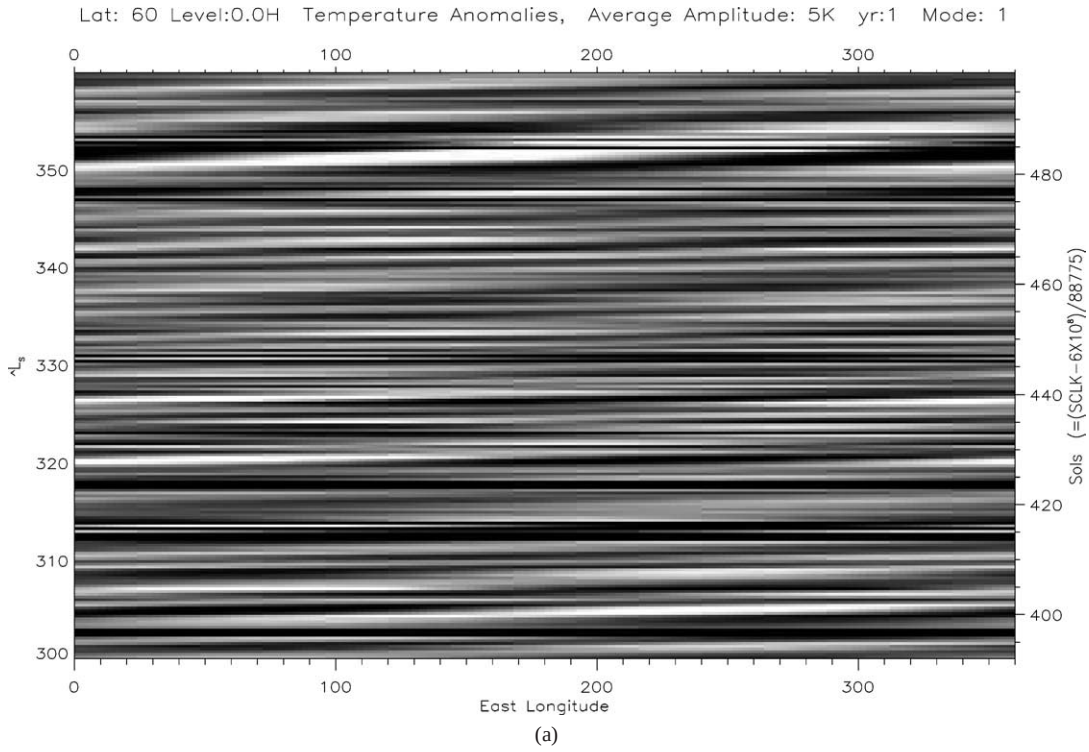

(a)

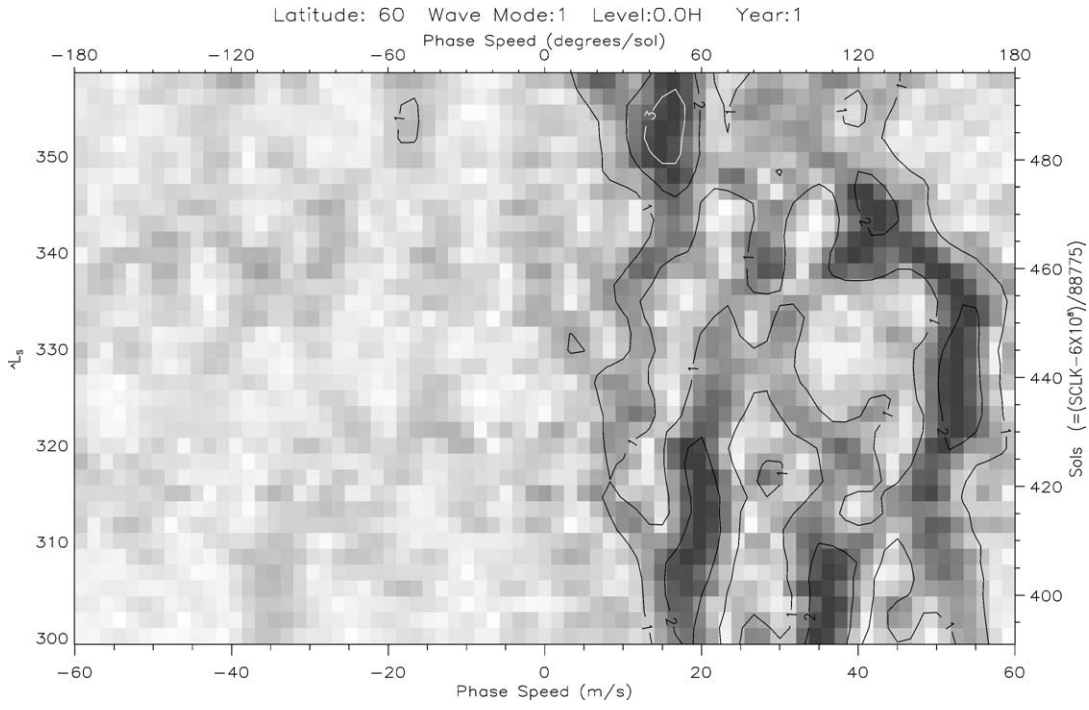

(b)

Fig. 6. Hovmoller diagram and phase speed versus time for $m = 1$ traveling waves from $L_s \sim 300°$–$360°$ of the first MGS mapping year at 60° N and 6.1 mbar. There is complicated behavior here near the surface in northern winter and spring. Slower waves early on give way to very fast waves that then appear to smoothly slow down, ultimately to be replaced by a 7 sol wave. All the waves have amplitude of roughly 2–4 K.

4.1.2. Second year

From the most broad overview, the second year is much the same as the first (see Fig. 9). That is, the northern hemisphere has strong $m = 1$ traveling waves in the vicinity of the polar vortex from fall equinox to spring equinox. The southern hemisphere has only very weak $m = 1$ traveling waves, with some of them propagating westward around the planet during southern summer and fall. The periods of the northern waves vary from 2.5 sols out to 30 sols or longer. Again, there is a suggestion of faster waves dominating near

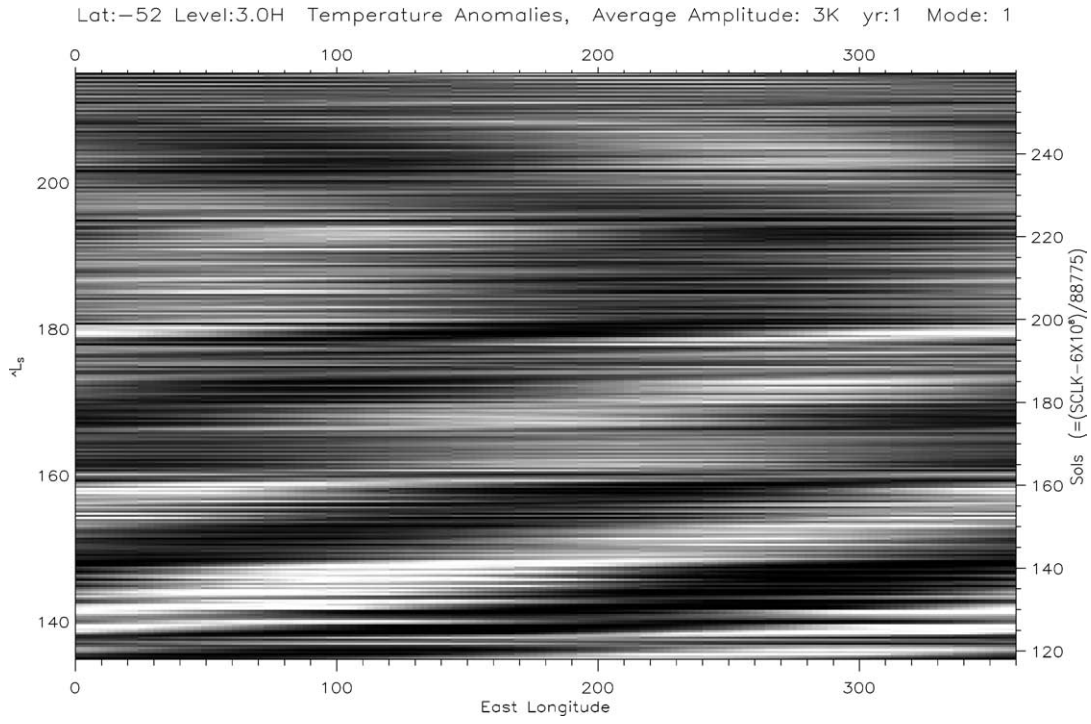

(a)

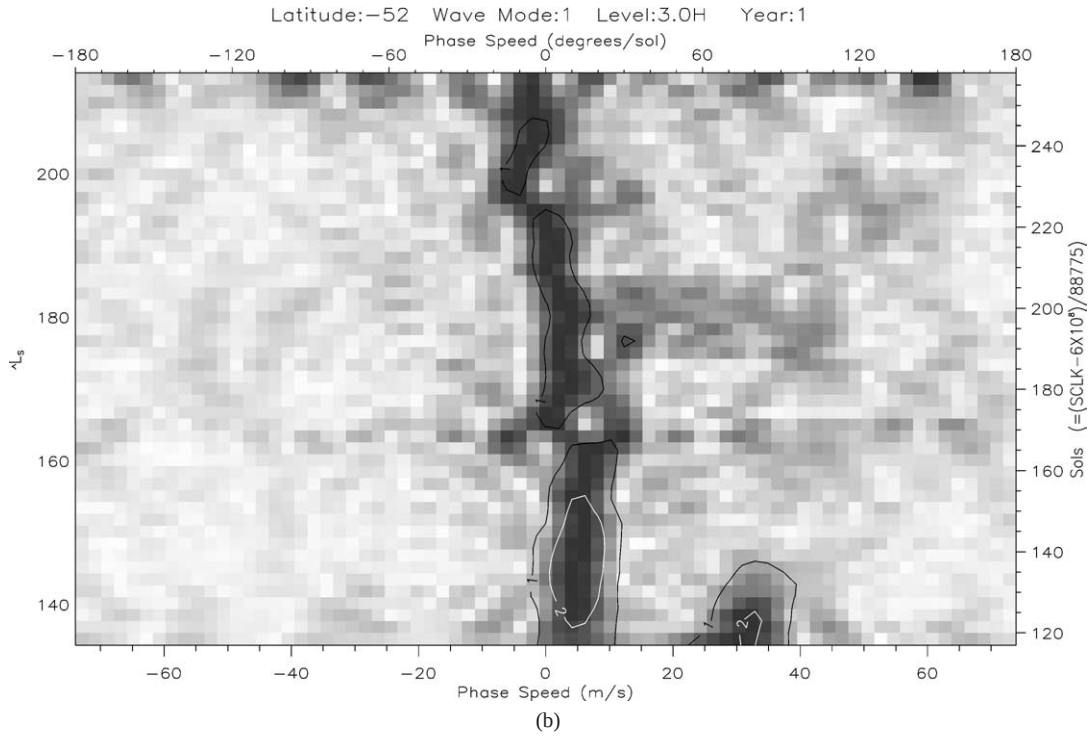

(b)

Fig. 7. Hovmoller diagram and phase speed versus time for $m = 1$ waves from $L_s \sim 135°$–$215°$ of the first MGS mapping year at 52° S and 3 scale heights altitude. The larger amplitude (1–2 K), slow (∼ 30 sol period) wave at the beginning of this interval slowly transitions from an eastward propagating wave to a westward propagating wave after $L_s \sim 190°$.

the surface, with slower waves having greater strength at altitude and extending their influence into the tropics. In general, the behavior of the $m = 1$ traveling waves seems quite similar between the first and second mapping years of TES.

Looking more closely at the differences, the second year has a significantly larger $m = 1$ wave during southern spring equinox ($L_s \sim 165°$–$195°$), centered at about 50° S and above about 1.5 scale heights altitude. It reaches a maximum amplitude of about 5 K with a period of 24 sols at

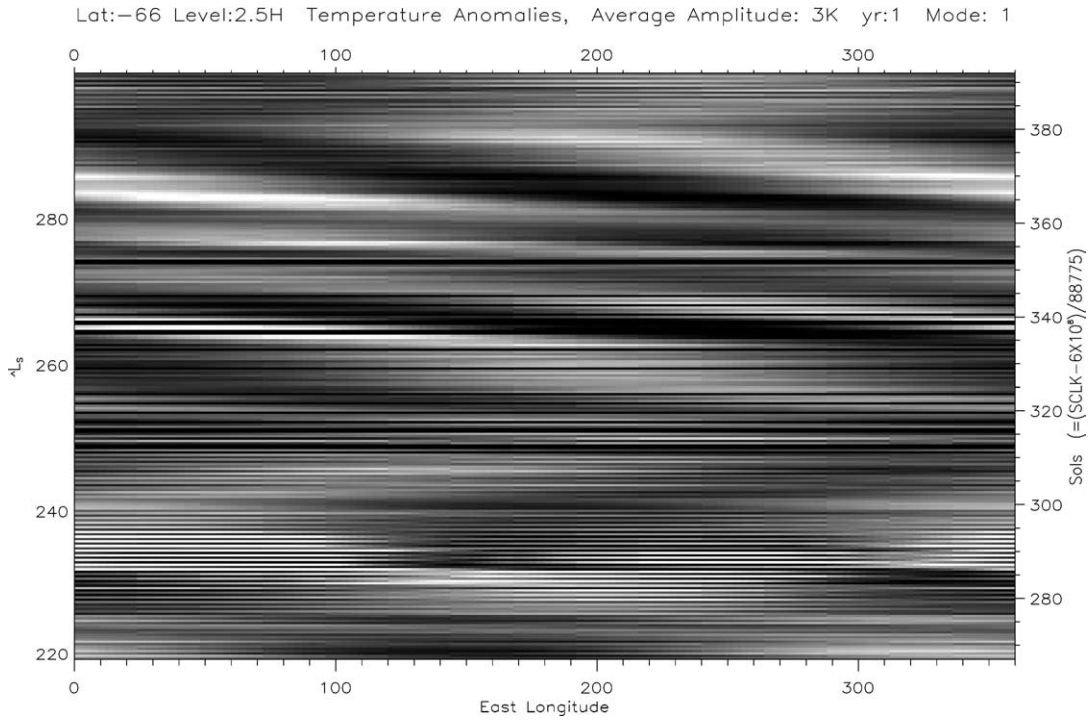

(a)

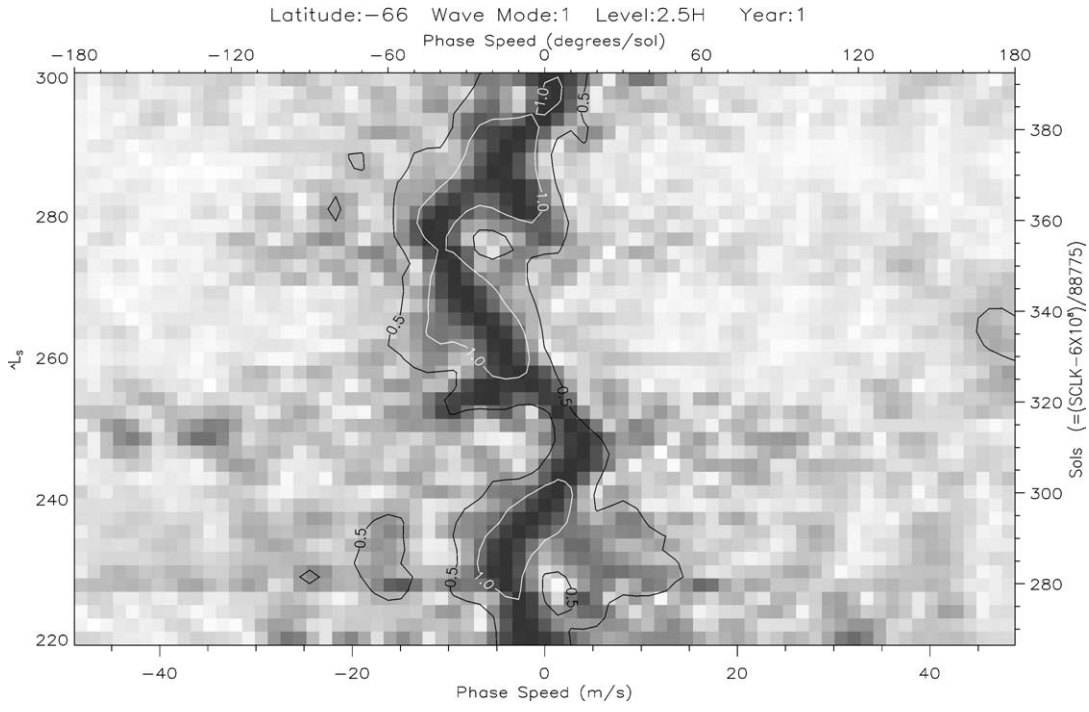

(b)

Fig. 8. Hovmoller diagram and phase speed versus time plots for $m = 1$ traveling waves from $L_s \sim 220°$–$300°$ of the first MGS mapping year at 66° S and 2.5 scale heights altitude. Both weak eastward and stronger westward propagating waves are clearly evident in this sample, with amplitude just over 1 K around $L_s \sim 230°$ and $L_s \sim 255°$–$300°$, and a minimum periods of about 8 sols.

$L_s \sim 195°$ then falls off quickly in amplitude (Fig. 10). The previous year, a much smaller southern $m = 1$ traveling wave was seen at that time (i.e., about 1 K versus 5 K). It is of note that a significant planet-encircling dust storm started at about $L_s \sim 187°$ during the second year (Smith et al., 2001b), just when this southern wave is reaching its maximum of about 5 K. Smith et al. (2001b) note that the dust storm front propagates east with a rough period of 15 sols, similar to the waves we see, but a bit faster than our 24 sols. There is even a suggestion of a standing wave at this time,

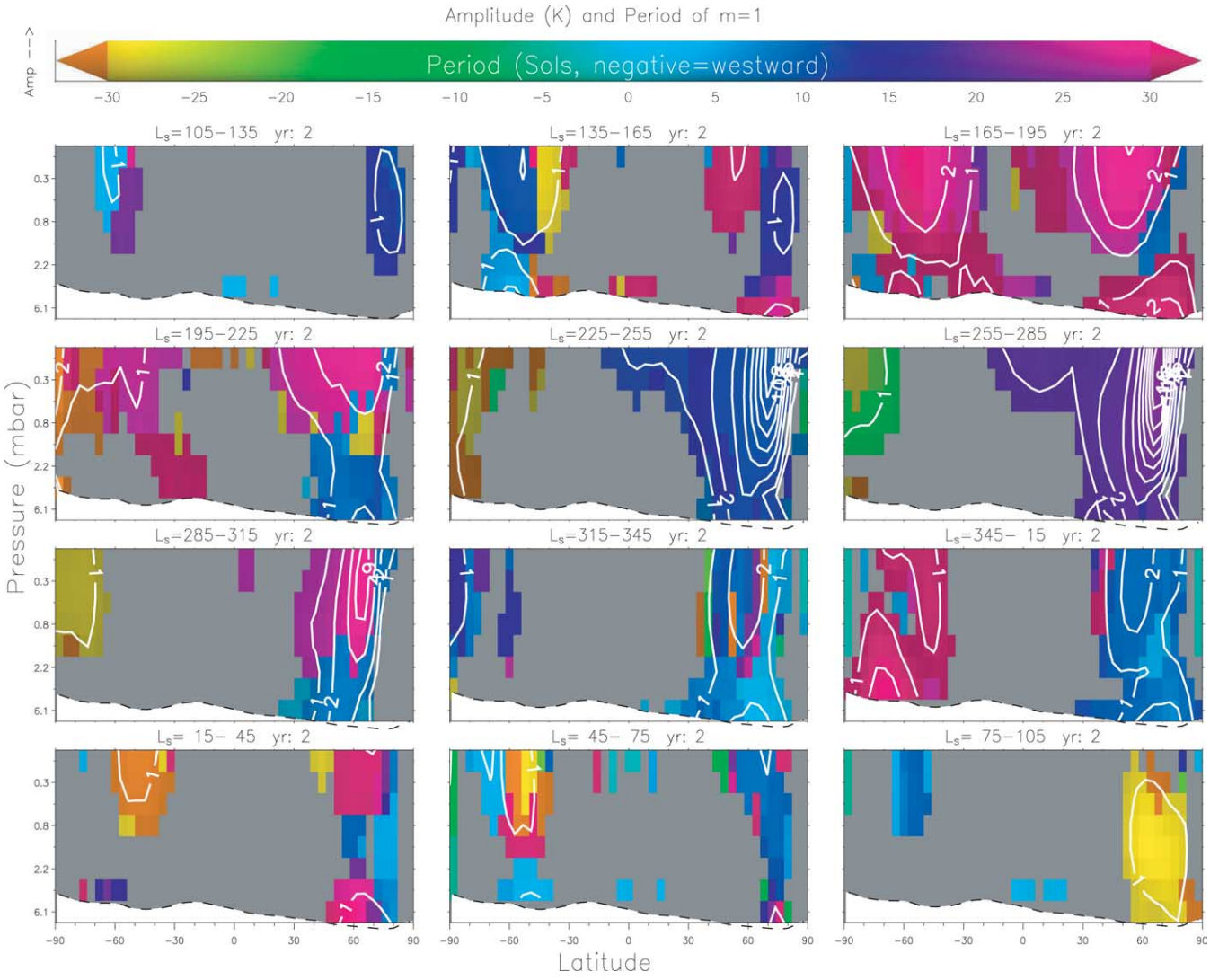

Fig. 9. Meridional cross sections of $m = 1$ traveling wave amplitude and dominant period for the second MGS mapping year. This plot is of the same format as Fig. 5. The behavior during the second year is very similar to the first, but with even stronger waves present in the north during late fall-winter. Some evidence of stronger dust storm effects are also evident for $L_s \sim 165°$–$195°$.

with a westward 20 sol wave with amplitude 1 K evident in the data further poleward (e.g., $\sim 68°$ S). At the same time, in the north, a strong $m = 1$ traveling wave dominates the region near the building polar vortex where there was only a small one the previous year (2 K versus more than 6 K). The southern hemisphere wave shows significant amplitude first in the core (e.g., near 55° S), and then only after it speeds up again on the periphery. This explains the apparent two different periods on Fig. 9 for $L_s \sim 165°$–$195°$, the faster northern region only experiences significant traveling waves when the wave is moving more quickly. However, for the following seasonal bin ($L_s \sim 195°$–$225°$), there *are* two waves simultaneously occurring near the polar vortex. The one that dominates near 50° N is the slow wave from just before, with a period as long as 30 sols. Dominating the regions poleward of about 55° N is a faster wave that begins around $L_s \sim 190°$ (roughly coincident with the onset of the planet-encircling dust storm), and has a period of about 7 sols. Near the surface, only the faster wave is evident.

The development of the dominant $m = 1$ traveling wave in the northern polar vortex during late fall and winter solstice of the second year differs somewhat from the previous year (Fig. 11, compared to Figs. 1 and 2). By about $L_s \sim 210°$, a 2 K wave has developed with a period of about 5 sols. The wave amplitude quickly grows, and by $L_s \sim 235°$ it has already exceeded 16 K. As its amplitude grows, its period is lengthening steadily. By $L_s \sim 235°$ the period has slowed to 9 sols. By $L_s \sim 250°$ the period has slowed to 12 sols, and by $L_s \sim 260°$ the amplitude has peaked at roughly 21 K. By about $L_s \sim 270°$, the amplitude has dropped to about 16 K, and the period has slowed to 20 sols. After this time, the period gently slows to about 30 sols, while the amplitude continues to drop. We call this secular trend in the wave's period a "chirp" adopting the parlance

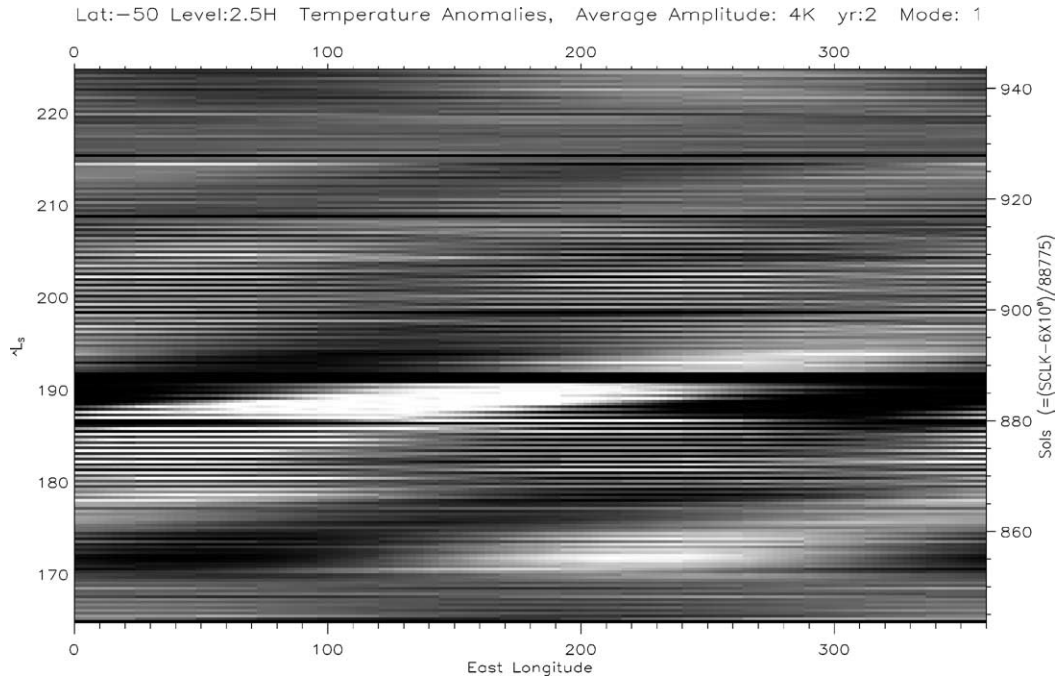

(a)

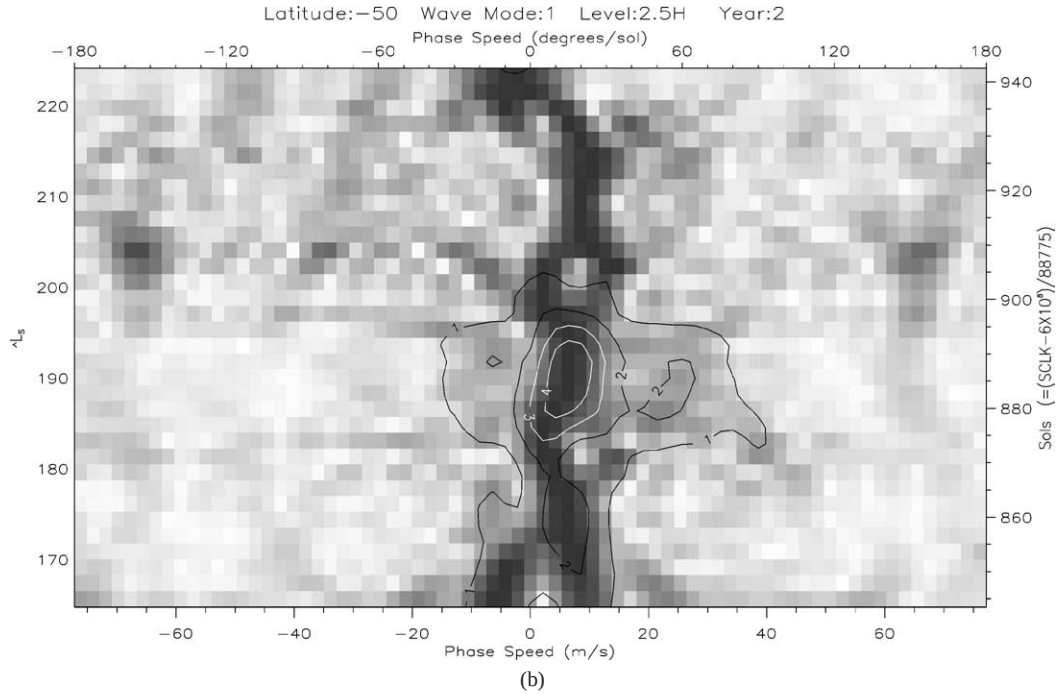

(b)

Fig. 10. Hovmoller diagram and phase speed versus time for $m = 1$ traveling waves from $L_s \sim 165°$–$225°$ of the second MGS mapping year for 50° S and 2.5 scale heights altitude. A relatively strong wave is evident at $L_s \sim 190°$ when a dust storm is growing. The previous year showed a much weaker wave at this time and location, suggesting the dust storm encouraged its growth and possibly vice versa.

of electrical engineering (and ornithology). The significance of this chirping is not clear, but it suggests that some trend in the atmosphere is changing the nature of the waveguide in which the traveling waves propagate. The more dramatic chirping of the dominant $m = 1$ traveling wave in the second year's winter suggests that the large global dust storm that was then waning has some influence on the waveguide. Finally, by about $L_s \sim 290°$, this slow wave is dominated by a different period (~ 7 sol) $m = 1$ wave that may be a harmonic of the slower wave.

The only other notable difference between the first and second year's $m = 1$ traveling waves occurs between 50° and 80° N in the lowest 3 scale heights from $L_s \sim 90°$–$110°$. Here, a 1–2 K westward 30-sol wave is evident. While a similar one was found in the previous year much closer to the pole, this one is larger in amplitude and evident in a broader

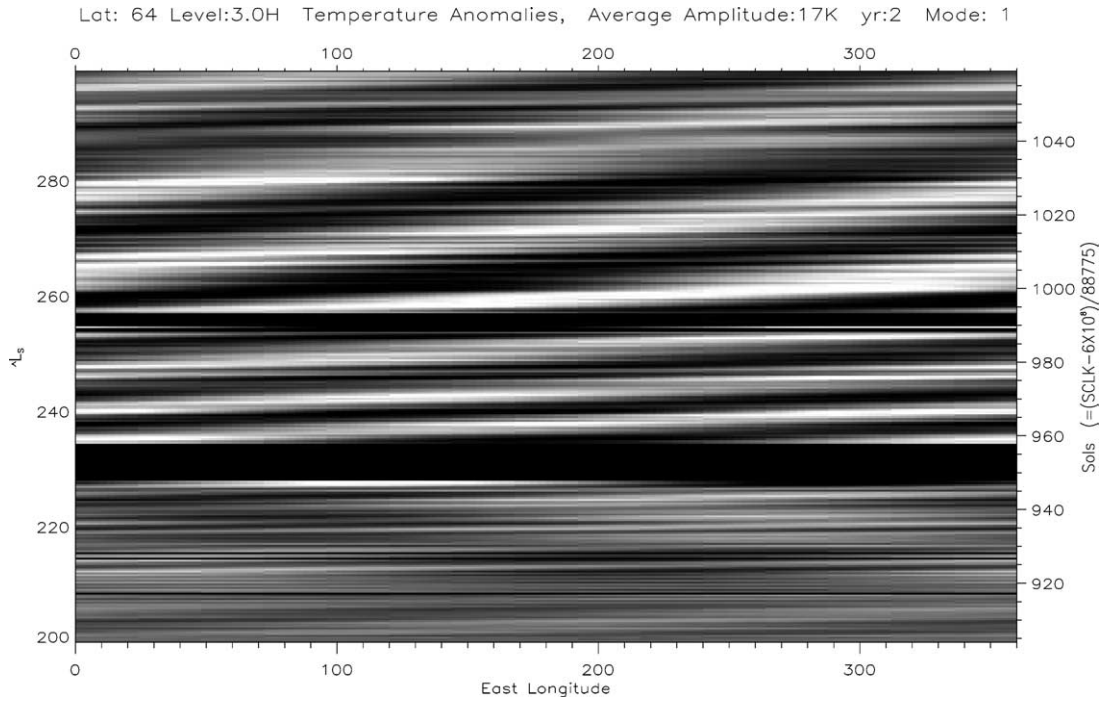

Fig. 11. Hovmoller diagram and phase speed versus time for $m = 1$ traveling waves from $L_s \sim 200°$–$300°$ of the second MGS mapping year at 64° N and 3 scale heights altitude. This plot is analogous to Figs. 1 and 2 for the first year. Note the larger amplitudes (> 20 K) and the secularly changing period ("chirping") of the wave down to a period of about 30 sols. The wave remains coherent for over 80 sols. The dropouts at $L_s \sim 230°$ and $L_s \sim 250°$ introduce more noise in the power spectra, but are short enough for our algorithm to interpolate across with confidence. This is the largest traveling wave observed in our data set.

region. As it weakens, it's period lengthens, eventually becoming a faint eastward wave after about $L_s \sim 110°$. Aside from these noted differences, the first and second year's $m = 1$ traveling waves are very similar.

4.1.3. Relative phases

We now turn to the relative phases of the $m = 1$ traveling waves. We will only discuss relative phases within regions and seasonal bins that are dominated by the same

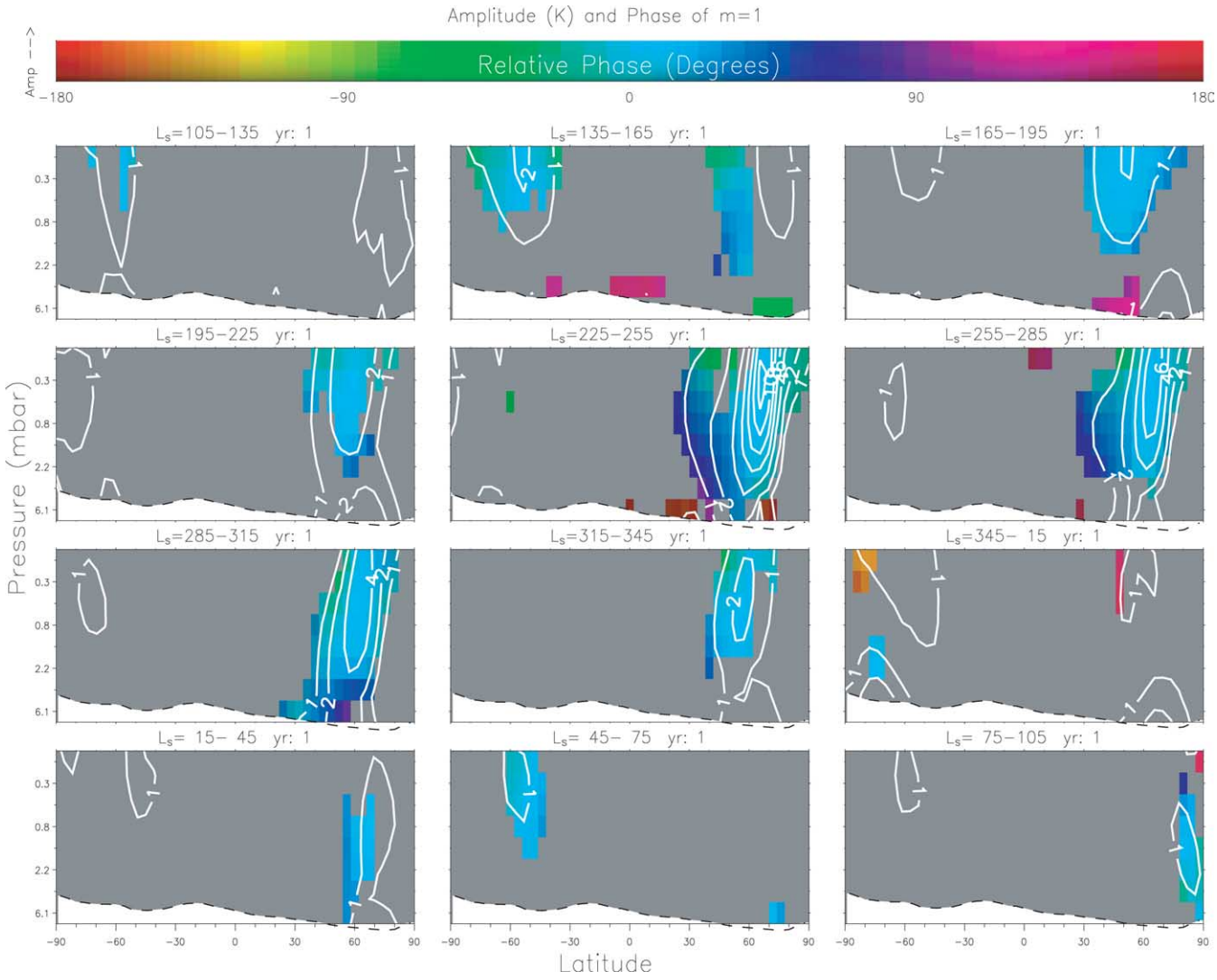

Fig. 12. Amplitude and phase of the $m = 1$ traveling waves during the first MGS mapping year. This plot is similar in structure to Figs. 5 and 9 showing the seasonal evolution of the waves, but each panel is equivalent to Fig. 4, showing the relative phase of the wave over the region where it is dominant. Phases are referenced to the location with maximum amplitude, and values are only presented where the local dominant period matches that at the location of maximum. In general, the northern $m = 1$ wave show a westward phase tilt with height.

phase speed wave as the region with the maximum amplitude. Figure 12 shows the relative phases of the dominant $m = 1$ traveling waves in the first MGS mapping year. In these plots, the light blue color is zero relative phase (relative to the location of maximum amplitude), and the other colors indicate the number of degrees of east longitude that the local maximum there is offset.

Starting at $L_s \sim 135°$–$165°$, the maximum amplitude is about 3 scale heights above 55° S. To the north and south of this location, the phase of this slow eastward propagating wave apparently lags to the west. At lower altitudes, it appears to lead from the east. The region in the northern hemisphere highlighted in the plot is also coherent with the region of maximum amplitude in the south, both dominated by slow eastward waves of the same period. In the north, the relative phase only differs from the location of maximum by less than 45°. Again, it appears that lower altitudes are advanced eastward in phase, while upper altitudes away from the maximum amplitude lag to the west. Slightly later, at $L_s \sim 165°$–$195°$, the slow wave is dominating the northern hemisphere as well. Here, the maximum is in the north, and the phase behavior there is the reverse of that in the south. That is, the regions north and south of the maximum are advanced to the east of the phase of the region of maximum. The southern wave, while essentially coherent with that in the north at this time, computes to a slightly different period, and thus is not included on this plot.

Clear results are found throughout late northern fall and winter along the polar vortex. From $L_s \sim 195°$–$345°$, the behavior is consistent with relative phases nearly constant in the high amplitude region of the wave, and advancing eastward with latitude at high altitudes south of the polar vortex. There is also evidence of a westward phase tilt with height for regions south of the amplitude maximum. However, the

phase tilt with height along the axis of the wave maximum changes twice during this time. At first, from $L_s \sim 195°$–$225°$, there is significant westward tilt with height at 60° N, about 90° over 2 scale heights near 2.2 mbar. From $L_s \sim 225°$–$285°$, the phase tilt with height at 60° N is minimal, if not slightly eastward. Finally, from $L_s \sim 285°$–$345°$, the phase tilt with height at 60° N is again large as it was earlier. Recall that westward phase tilts with height are indicative of poleward heat transports by the wave, and so the heat transport by the waves at 60° N is modulated throughout this season.

Wilson et al. (2002) noted that the slow wave in northern winter of the first year apparently is coherent throughout the tropics at higher altitudes. This is not evident in Fig. 12, as the tropics are dominated by a very slightly different period wave. However, in the second year of data, where the northern slow wave behavior was similar, it is evident (not shown). From $L_s \sim 225°$–$285°$ of the second year, the phase advanced westward with height throughout the tropics with a vertical wavelength of about 6.5 scale heights.

The exact mechanism that extends the influence of the traveling waves from the region of the polar vortex, where a low wave number Rossby wave duct exists (e.g., Banfield et al., 2003), down to the tropics is not yet clear. Speculations based on inertial instability have been put forward by Barnes et al. (1993) and Wilson et al. (2002). Wilson et al. (2002) modeled the slow wave evident in the first year of data, finding good accord between their model results and the amplitude and phase structure observed in the first year. However, the modeled wave period was 10 sols, while the first year's data showed a 20 sol period. Fortunately, at about $L_s \sim 240°$ of the second year, the observed slow wave had a 10 sol period, strengthening our confidence in the applicability of the Wilson et al. (2002) modeling. The axisymmetric model results discussed in Wilson et al. (2002) as an analogue for the slow waves, indicated a shorter wave period for stronger (dustier) thermal forcing. Perhaps the rapid clearing of dust following the major 2001 dust storm ($L_s \sim 187°$, MGS mapping year 2) is then part of the explanation for the chirping of the wave period. These ideas and those in Wilson et al. (2002) will be more fully explored in later work. Here we only speculate that the slow waves may be a fused Rossby–Kelvin wave, propagating westward relative to the eastward mean flow in the mid-latitudes (hence the Rossby wave) and eastward relative to the westward mean flow in the tropics (hence the Kelvin wave). A Kelvin wave in the tropics is consistent with the finite vertical wavelength indicated by the tropical phase structure in our data and the model results in Wilson et al. (2002). This also accounts for the attenuated amplitudes between our results and those of the modeling.

Of note in the second year are the nearly symmetric $m = 1$ traveling waves seen in both hemispheres from $L_s \sim 165°$–$195°$ (e.g., Figs. 9 and 10). These are mainly due to the onset of the planet-encircling dust storm after $L_s \sim 187°$ and at times are both traveling with the same phase speed. In the region where these traveling waves have significant amplitude, their phases are nearly constant (not shown). The only trend being a slight westward phase tilt with latitude in the north. It is also of note that the waves in the two hemispheres are nearly perfectly in phase with one another, with each having maxima at about the same longitude at the same time in their cores. This suggests that this really is a global mode with manifestations in both hemispheres, and may be another manifestation of the same phenomenon causing the large northern winter slow waves. In this case it appears symmetric between the hemispheres because the zonal winds there are both eastward and about equal and thus Rossby waves can propagate in both hemispheres. At northern solstice, Rossby waves are forbidden for the southern midlatitudes with westward winds there, and hence the global mode is asymmetric then.

4.2. Zonal wavenumber 2

4.2.1. First year

Figure 13 shows the amplitude and period for zonal wavenumber 2 from the first mapping year of MGS. This is analogous to Fig. 5, but for $m = 2$.

Starting in the northern hemisphere, at about $L_s \sim 180°$ an $m = 2$ traveling wave greater than 1 K appears at 60° N in the lowest half scale height of our sensitivity. The wave spreads vertically, and by $L_s \sim 200°$ it has reached the top of our domain, still centered above 60° N. By this time the amplitude near the surface exceeds 2 K, and the influence of the wave extends from 30° to 80° N near the surface. The wave initially has a period of about 4 sols, then speeds up after $L_s \sim 180°$, reaching ~ 3 sols by $L_s \sim 200°$. At the southern edge of the region with significant $m = 2$ traveling wave amplitude (e.g., 30°–55° N), a slower (6 sol) wave appears at about $L_s \sim 190°$. This slower wave dominates the region, but the 3 sol wave also is present there and with nearly the same amplitude. This 3 sol wave takes over the behavior along the polar front, and dominates there until about $L_s \sim 222°$. At that time, the dominant period throughout the region with significant $m = 2$ traveling wave amplitude quickly switches to just over 2 sols, then 2.5 sols, and finally ends up at about 3.5 sols after $L_s \sim 240°$ (see Fig. 14b). This 3.5 sol wave then dominates the core of the polar front until about $L_s \sim 320°$, a span of about 130 sols. The northern and southern edges of the polar front also show evidence for slower waves, with periods ranging from 6–12 sols which sometimes dominate over the 3.4 sol wave, but these slower waves are of smaller amplitude and are more intermittent, usually lasting 20 sols at a time. In particular, the slow $m = 2$ waves evident from $L_s \sim 225°$–$255°$ are likely related to the dust storm that started at this time (Smith et al., 2001a, 2001b) which also created a standing $m = 1$ wave noted above.

By northern winter solstice, the $m = 2$ wave duct has narrowed into a sharp zone tilting poleward with the polar front, centered on about 60° N. The $m = 2$ wave amplitudes

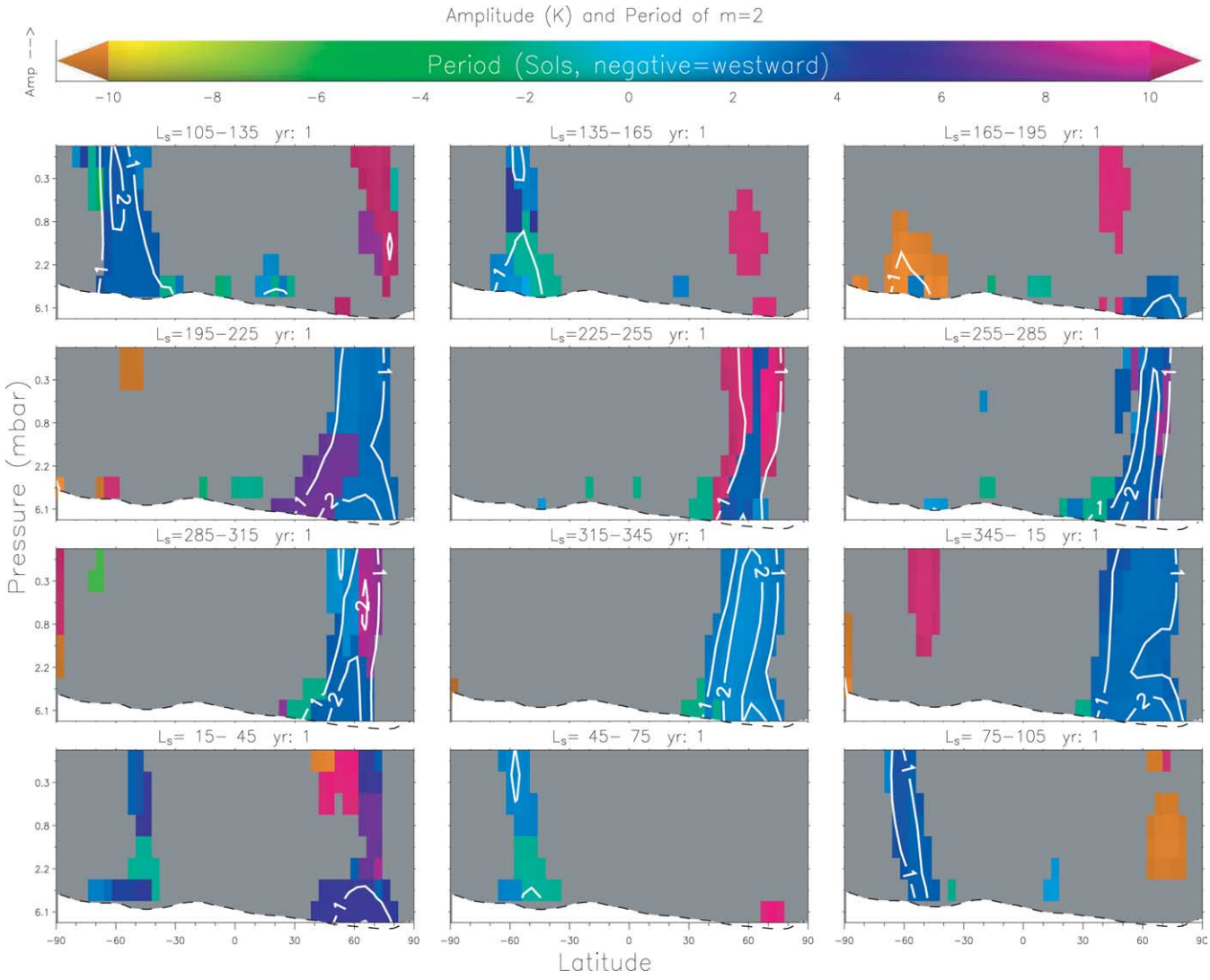

Fig. 13. Amplitude and period of the $m = 2$ waves for the first MGS mapping year. This figure is analogous to Figs. 5 and 9, but for $m = 2$ instead. Note that the color bar now represents a different span of periods. The $m = 2$ waves are generally small (< 4 K), and concentrated closer to the surface. Like $m = 1$, $m = 2$ traveling waves are more evident in the north.

are about 2 K in the core of this region with the dominant period 3.5 sols. However, amplitude clearly exists at other phase speeds as well after $L_s \sim 260°$ (see Fig. 14). Notably, both $\pm 104°$/sol at ~ 1 K at the surface at 50° N, indicating a standing wave with a period of 1.7 sols. This same location also shows amplitude just under 2 K at 78°/sol or 2.3 sols period and about a 1 K wave with a period of about 7 sols. 1.5 scale heights above 60° N also shows the 2.3 sol wave after $L_s \sim 260°$. The highest altitudes on the polar front also show ~ 2 K amplitude with an ~ 8 sol period. At $L_s \sim 320°$, the 2.3 sol wave becomes dominant throughout the region where $m = 2$ traveling waves have significant amplitude. This lasts until about $L_s \sim 338°$ when a 3 sol wave takes over. This one dominates until about $L_s \sim 0°$. After this time, the phase speed of the dominant $m = 2$ traveling wave in the vicinity of the northern polar front appears to decrease in a nearly steady fashion. By $L_s \sim 45°$, it has slowed to a period of about 7 sols. The amplitudes have also been steadily dropping after $L_s \sim 335°$. They fall below 1 K everywhere in the north at $L_s \sim 45°$.

The south has its first signs of significant $m = 2$ traveling waves in early southern winter at $L_s \sim 60°$–$65°$ (at the end of the first year) at 58° S and 3 scale heights altitude. Here, the wave just barely exceeds 1 K, and has a period of 2.5 sols. Stronger southern winter $m = 2$ waves then start in after $L_s \sim 88°$, when a 1 K wave with a period of 3.6 sols appears in a narrow strip along the polar front. This persists until about $L_s \sim 135°$ (jumping back to the beginning of the first year) growing to over 2 K, when the behavior becomes more complex. A 2.5 sol wave dominates the highest altitudes, above 3 scale heights near 56° S. A 4 sol wave of less than 1 K dominates just below that. A standing wave with a period of about 1.7 sols dominates from 2 scale heights to the surface trending northward to 40° S. This appears on the period plot as a westward wave with a 1.7 sol period because the westward wave slightly

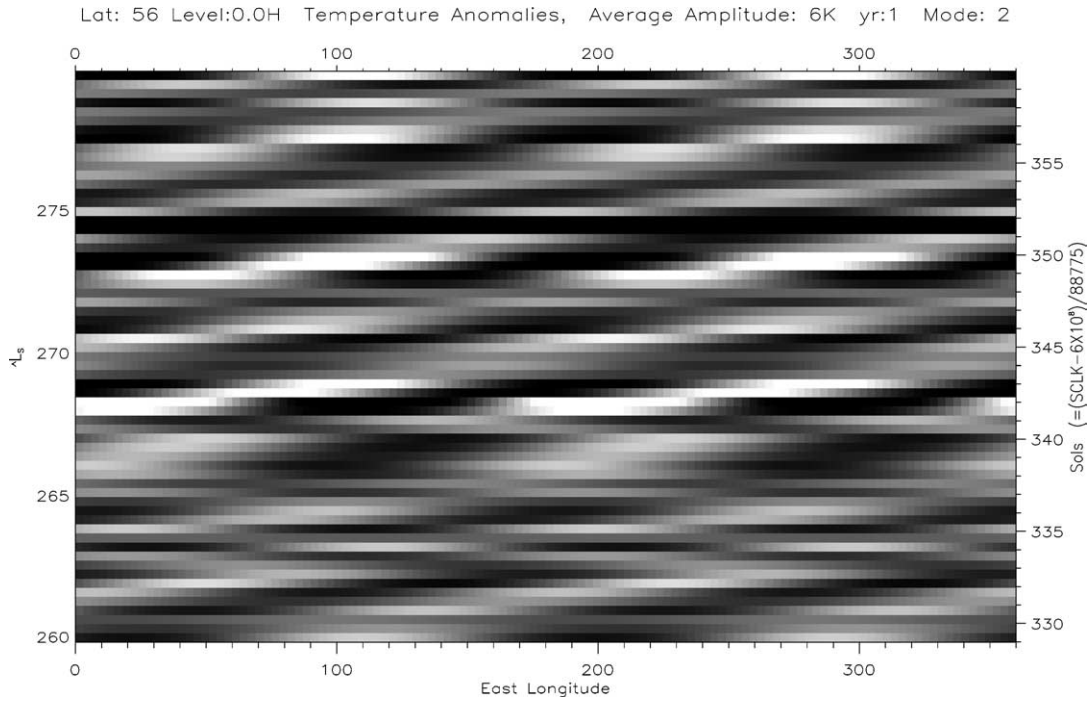

(a)

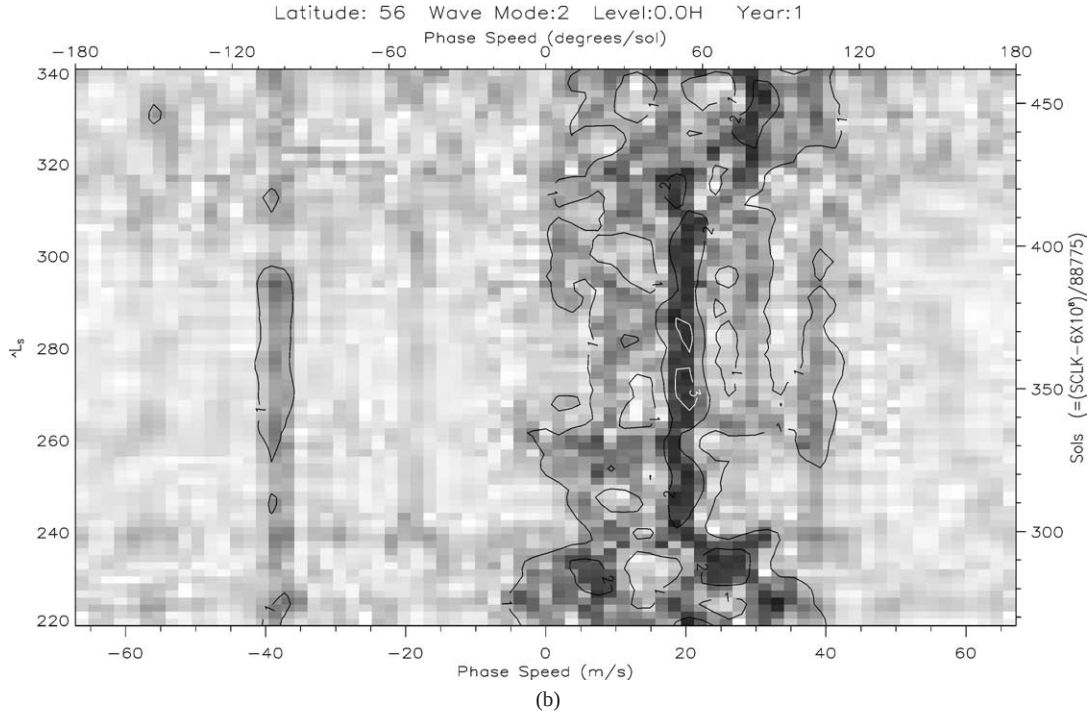

(b)

Fig. 14. Hovmoller and phase speed versus time plot for $m = 2$ traveling waves at 56° N and 6.1 mbar. The Hovmoller diagram only shows $L_s \sim 260°$–$280°$ of the first MGS mapping year for clarity, while the phase speed versus time plot shows $L_s \sim 220°$–$340°$. In this case, the Hovmoller diagram only shows the $m = 2$ component of the data. The behavior here is complex, with a dominant wave of about 2.5 K and 52°/sol (3.5 sols). However, there are also simultaneously waves present with phase speeds ~ 78, ~ 104, and $-104°$/sol.

dominated the eastward wave comprising the standing wave. Finally, near the surface at 60° S, a 2.4 sol wave dominates. After this, the $m = 2$ wave is only seen closer to the surface in the south, below about 2 scale heights altitude. At $L_s \sim 175°$, the southern hemisphere $m = 2$ traveling wave amplitude is below 1 K in all but the lowest scale height above 60° S. Here a nearly stationary, slow westward wave competes with moderate eastward waves, first with a 4 sol period, then with a 2.9 sol period, all of them dying out after $L_s \sim 195°$.

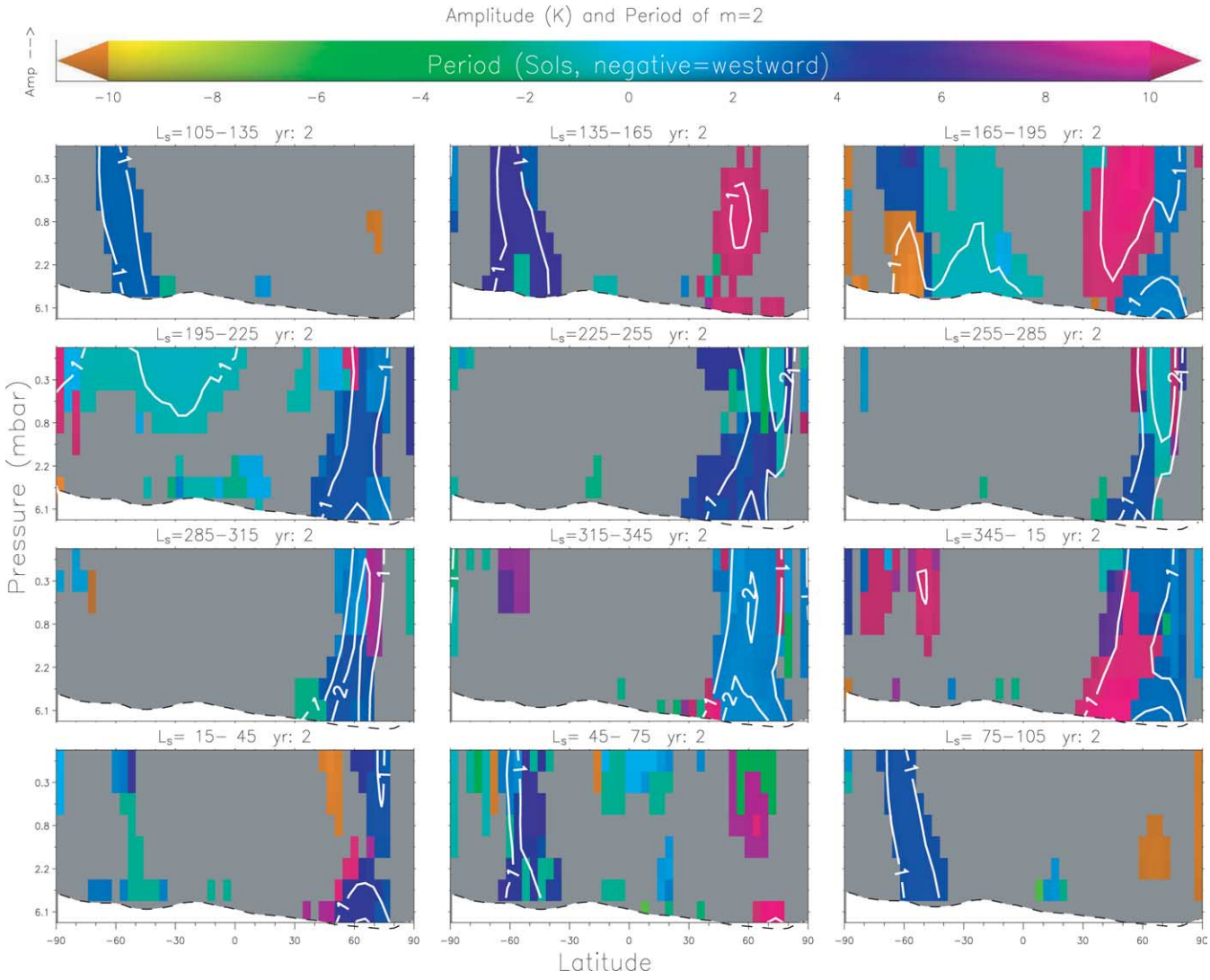

Fig. 15. Amplitude and period of $m = 2$ traveling waves during the second MGS mapping year. This figure is analogous to Fig. 13, but for the second year of data. Interannual variability is relatively small, with some differences evident during the large second year dust storm, and in the core of the region with the strongest $m = 1$ northern winter traveling waves.

4.2.2. Second year

Much like the $m = 1$ traveling waves, the second year's behavior of the $m = 2$ traveling waves are very similar to that of the first year (see Fig. 15). The northern hemisphere has strong $m = 2$ traveling waves in the vicinity of the polar front from fall equinox to spring equinox. Amplitudes peak at just over 2 K, and the regions with notable amplitude are confined slightly more near the surface than for the $m = 1$ traveling waves. Periods are again between about 2.3 sols and about 4.3 sols. Before and during the planet-encircling dust storm (i.e., $L_s \sim 140°$–$195°$) a very long period (~ 30 sols) wave appears in the data above 1 K. There were hints of a similar wave the previous year, but below 1 K. The southern hemisphere has weaker $m = 2$ traveling waves, peaking at just over 1 K in only a very few places and times. These too have periods near 3 sols. For $L_s \sim 195°$–$225°$ of the first year, it was noted that slower $m = 2$ traveling waves were dominant on the lower and southern edges of the polar front than those dominant in the core of the polar front. This trend is repeated in the second year, at the same time. Note that this is somewhat the reverse of the behavior seen with the $m = 1$ traveling wave, where the secondary waves at the bottom edges of the duct were usually faster waves than those dominating the bulk of the polar front. There are several other instances of subtleties in the $m = 2$ traveling wave behavior that are similar in the first and second years. In general, the behavior of the $m = 2$ traveling waves seems quite similar between the first and second mapping years of TES.

Among the differences between the first and second years for the $m = 2$ traveling waves in the MGS TES nadir data are the fast westward propagating waves seen in the upper altitudes of the northern polar front just before and during northern winter solstice and in southern midlatitudes from $L_s \sim 165°$–$225°$. For $L_s \sim 240°$–$275°$ of the second year, our analysis shows 2–5 K amplitude traveling waves mov-

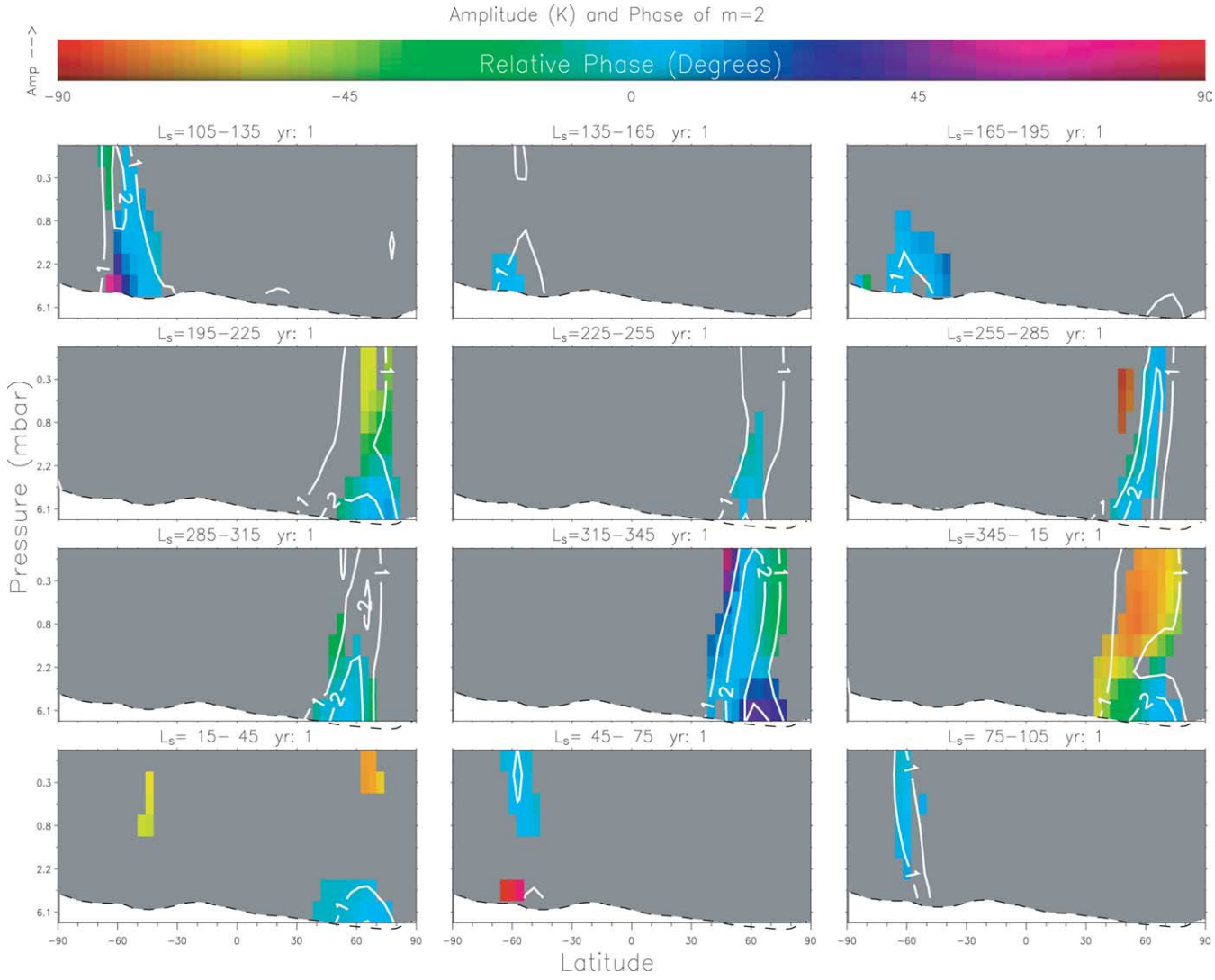

Fig. 16. Amplitude and relative phases of the $m = 2$ traveling waves during the first MGS mapping year. This plot is the same as Fig. 12, but for $m = 2$ waves.

ing with a phase speed of 165°–170°/sol westward in the region 2 scale heights and higher above 70° N. At this time, this is the dominant $m = 2$ wave in this region, which is also simultaneously experiencing very large $m = 1$ traveling waves (10–20 K). This $m = 2$ traveling wave is moving almost half as fast westward as the Sun (1.1 sol period), and could perhaps be an artifact of incomplete tide removal, or an overtone of the strong $m = 1$ traveling wave. We do not understand why it is not a multiple of the Sun's speed if it is indeed a tidal artifact. Adding to the suspicion that it might be an aliased tide, most of the tropics are dominated by a wave with this same period (but amplitudes only occasionally exceeding 1 K, more often in the southern tropics) for $L_s \sim 175°$–$220°$ of the second year. Recall that this period includes the beginning of a planet-encircling dust storm that might significantly enhance the strength of the tidal modes. However, the westward mode appears in the tropics before the dust storm commences, yet reaches its maximum amplitudes in the first days of the dust storm. We are unsure whether this apparent traveling wave is a true free wave, or an aliased forced tide mode or an overtone of the strong $m = 1$ traveling wave.

4.2.3. Relative phases

We now turn to the relative phases of the $m = 2$ traveling waves. As before with the $m = 1$ traveling waves, we will only be addressing the relative phases of those regions that, for each seasonal bin, are locally dominated by the same phase speed wave as the region that has the maximum amplitude. Figure 16 shows the relative phases of the dominant $m = 2$ traveling waves in the first MGS mapping year. In the north, when the amplitude is largest, and the polar front is mainly dominated by a single phase speed $m = 2$ wave (i.e., $L_s \sim 315°$–$15°$), the relative phases generally show a westward tilt with height of less than or about 60° longitude over 3.5 scale heights on the poleward side of the polar front. Eastward phase shifts with height are apparent on the southern edge of the polar front in early northern

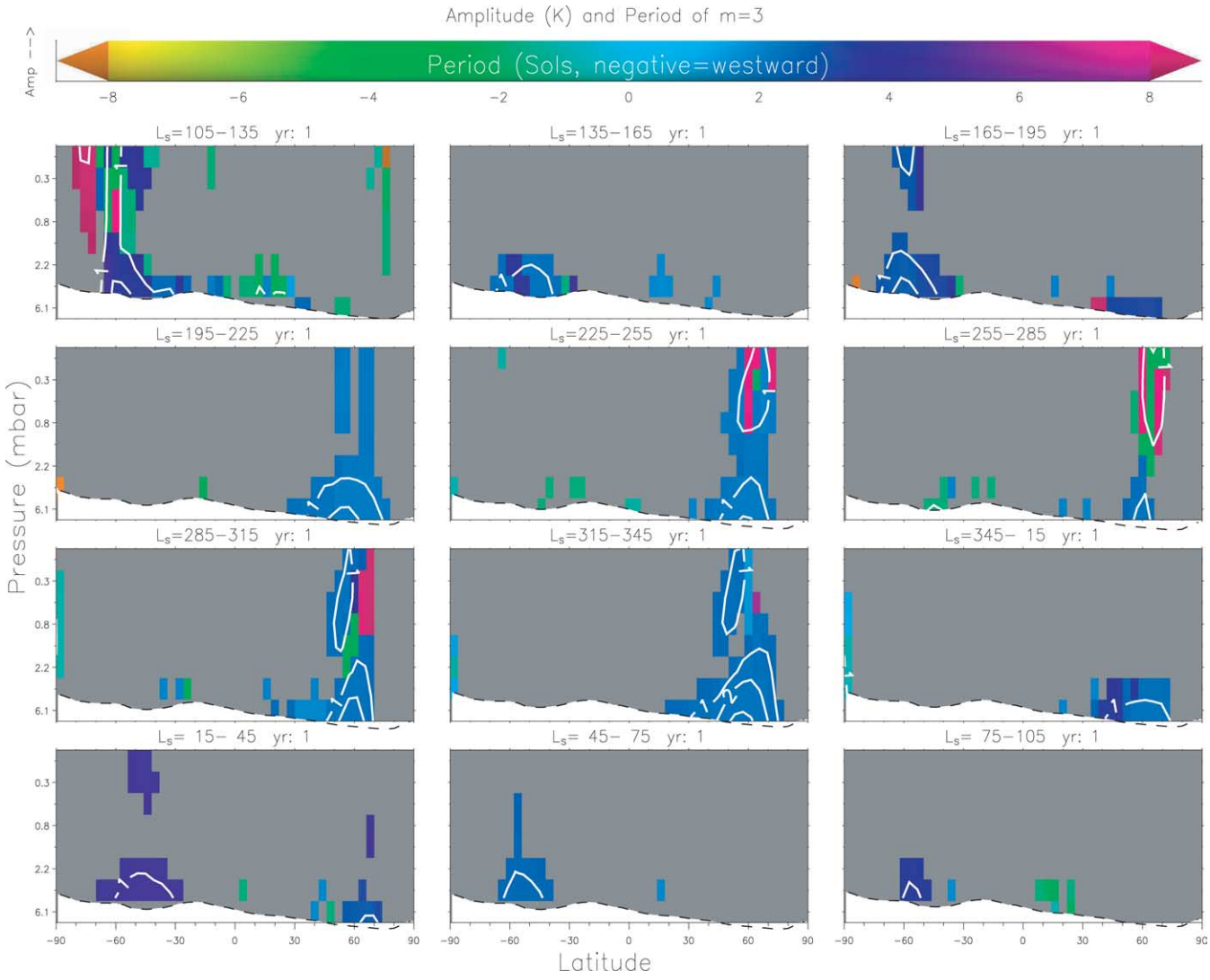

Fig. 17. Amplitude and period of the $m = 3$ traveling waves for the first MGS mapping year. This figure is analogous to Figs. 5 and 13, but for $m = 3$. The $m = 3$ waves are more strongly trapped near the surface than either $m = 1$ or $m = 2$. Amplitudes are comparable to the $m = 2$ waves, less than about 4 K. In both hemispheres, $m = 3$ waves appear to be favored in fall and late winter rather than mid-winter.

spring (i.e., $L_s \sim 315°$–$345°$). This causes this time to show a strong westward phase tilt with latitude, suggesting the possibility of significant meridional momentum transfers in the region above 2 scale heights. The southern hemisphere shows nearly the same as the north, including the amounts of the phase shifts and their spatial distribution, although the smaller amplitudes make it less conclusive. The second year (not shown) is very similar to the first, suggesting that interannual variability on the eddy fluxes due to $m = 2$ traveling waves are small.

4.3. Zonal wavenumber 3

4.3.1. First year

Figure 17 shows the amplitude and period for zonal wavenumber 3 from the first mapping year of MGS. This is analogous to Figs. 5 and 13, but for $m = 3$. Most evident for the $m = 3$ traveling waves is their significantly limited vertical extent compared to the $m = 1$ or $m = 2$ traveling waves. Maximum amplitudes are confined to the lowest scale height throughout the year, and amplitudes are less than 5 K everywhere. More typically maxima are about 2 K.

A 2 K $m = 3$ wave is first evident in the northern fall for $L_s \sim 195°$–$225°$. Amplitude greater than 1 K runs from 35° to 75° N in the bottom scale height, greater than 2 K from 50° to 60° N in the bottom half scale height. This wave initially ($L_s \sim 190°$) has a period of about 2.8 sols, then after $L_s \sim 215°$, it speeds up to 2.2 sols and grows in amplitude abruptly to about 5 K for a period of about 16 sols from $L_s \sim 220°$–$230°$ throughout which it retains phase coherence. By $L_s \sim 240°$, this wave has disappeared below 1 K.

At about $L_s \sim 270°$ a $m = 3$ traveling wave with a period of about 2.3 sols appears at the surface at 60° N. This wave remains remarkably steady in period, staying at 2.3 sols until about $L_s \sim 355°$, a span of about 140 sols, although the wave does not maintain phase coherence over this time. Typ-

ical phase coherence intervals range from 10–40 sols for this wave. The amplitude slowly grows to 2 K by $L_s \sim 300°$, then 4 K by $L_s \sim 315°$. The amplitude then starts to decline after $L_s \sim 338°$, more quickly than it grew. At its peak, amplitude is over 1 K in the bottom half scale height from 30° to 75° N, and up as high as 1.5 scale heights above 65° N. Interestingly, there is a separated region with amplitude greater than 1 K and the same period above 2 scale heights over 55° N in a band about 10° of latitude wide. This separated region of significant amplitude lasts from about $L_s \sim 300°$–335°. After $L_s \sim 355°$, the $m = 3$ wave at the surface near 60° N slows to a period of about 3.4 sols with an amplitude of less than 2 K. This lasts only until $L_s \sim 20°$ when it speeds up to about 2.7 sols. Finally, after $L_s \sim 30°$, the northern $m = 3$ traveling wave amplitude drops below 1 K until the next fall. However, there is a suggestion that weak $m = 3$ waves persist in this region with ever slowing period until they are truly lost in the noise at about $L_s \sim 65°$. Similarly, in the following year, $m = 3$ traveling waves are suggested in this region above the noise but below 1 K starting at $L_s \sim 140°$ with a very long period (∼ 20 sols) slowly speeding up.

The southern hemisphere first shows $m = 3$ traveling waves that are clearly distinct from noise in southern fall. For $L_s \sim 18°$–48°, a $m = 3$ traveling wave is seen in the bottom scale height above 35° to 60° S with a period of about 4.5 sols, and an amplitude of nearly 2 K. From $L_s \sim 48°$–65°, the period shortens to 2.5 sols, after which the amplitude drops below 1 K, but there is a suggestion the wave continues with this period above the noise until about $L_s \sim 90°$. After $L_s \sim 90°$, the wave again grows above 1 K, but now with a period of about 3.4 sols. Jumping back to the beginning of the MGS TES mapping year 1, starting at about $L_s \sim 120°$ we find an $m = 3$ traveling wave in the same region, with nearly the same period and amplitude. This wave has amplitude greater than 1 K between 30° and 65° S, and extending to the top of our domain in a very narrow channel above 60° S. It continues until about $L_s \sim 145°$, when it changes to a 2.5 sol period. At $L_s \sim 150°$, a second $m = 3$ wave is also evident in this region, this one also above 1 K, and with a period of about 3.4 sols. These two waves exist together until $L_s \sim 170°$ when the slower wave takes over, growing to 3 K, and slowly speeding up. By $L_s \sim 185°$, it has a period of 2.8 sols, but is starting to weaken in amplitude, and slow again in period. By $L_s \sim 200°$, the $m = 3$ traveling waves have disappeared in the south until the following southern fall.

It is worth noting here that Hinson and Wilson (2002) have reported traveling waves in the martian southern hemisphere for this same period of time. They found $m = 3$ waves, with a period of about 2 sols and amplitude less than 7 K. Their data pertained to 67°–70° S, 3 mbar and $L_s = 134°$–148° of the first mapping year. Figure 18 shows a Hovmoller diagram of our data for this same period of time, with waves $m = 1$–4 composited together. Combining the first four waves reproduces a more realistic representation of the true structure of the waves. The higher zonal wavenumbers contribute modestly to the overall structure. Note that our data, with less than 12 longitudes covered per half sol, cannot reliably resolve zonal wavenumbers greater than $m = 4$. The data in Fig. 18 is centered on 68° S (with a 4° wide bin), and 0.5 scale heights above 6.1 mbar (3.7 mbar). Evident in our data is a short wavelength wave ($m \sim 2-4$), most prominent for $L_s \sim 144°$–147°. The amplitudes of modes 1–4 are all similar (∼1–2 K each) throughout this period. The wave's period is about 2.4 sols, consistent with the 2 sols reported by Hinson and Wilson (2002) considering the limitations of their data set. The storm track behavior that they note is also evident in our data, with the amplitude mainly appearing between about 180°–360° E, similar to their observations. Our measured amplitudes are consistent with those of Hinson and Wilson (2002). They report amplitudes of up to 7 K, while we see an average amplitude of about 4 K, with peaks reaching as high as ±10 K particularly in the storm track. We return to this below, presenting the storm tracks.

4.3.2. *Second year*

The $m = 3$ traveling wave behavior during the second year of MGS mapping (not shown) is notably similar to that of the first. The spatial distributions, amplitudes and wave periods seen during southern hemisphere spring almost perfectly echo those of the previous year, including the occasional period changes. The northern fall and early winter had smaller $m = 3$ traveling wave amplitudes than the preceding year. The northern waves do not exceed 1 K near the surface until $L_s \sim 290°$, after which they are again very similar to the preceding year in the north.

4.4. *Relative phases*

We do not address the relative phases of the $m = 3$ traveling waves, as their amplitude are typically only significant in our analysis in our lowest levels. In the few locations where we can solve for the meridional structure of the relative phases of the $m = 3$ traveling waves, the phase differences are small where the amplitudes are significant.

5. Storm tracks and fronts

Storm tracks, regions of enhanced variability in the transient temperature perturbations, were first discussed for Mars in Hollingsworth and Barnes (1996). Their model simulations suggested that martian topography controls the storm tracks in Mars during northern winter. In our work, we noted the storm track behavior in the southern winter/spring (see Fig. 18) while comparing to the results of Hinson and Wilson (2002). This shows up in our results as the $m = 1, 2$, and 3 waves all having the same period, in this case about 2.4 sols. Again, it shows up in our data for $L_s \sim 140°$–160° of the second mapping year in the bottom scale height above 50° S (not shown). Here, the periods

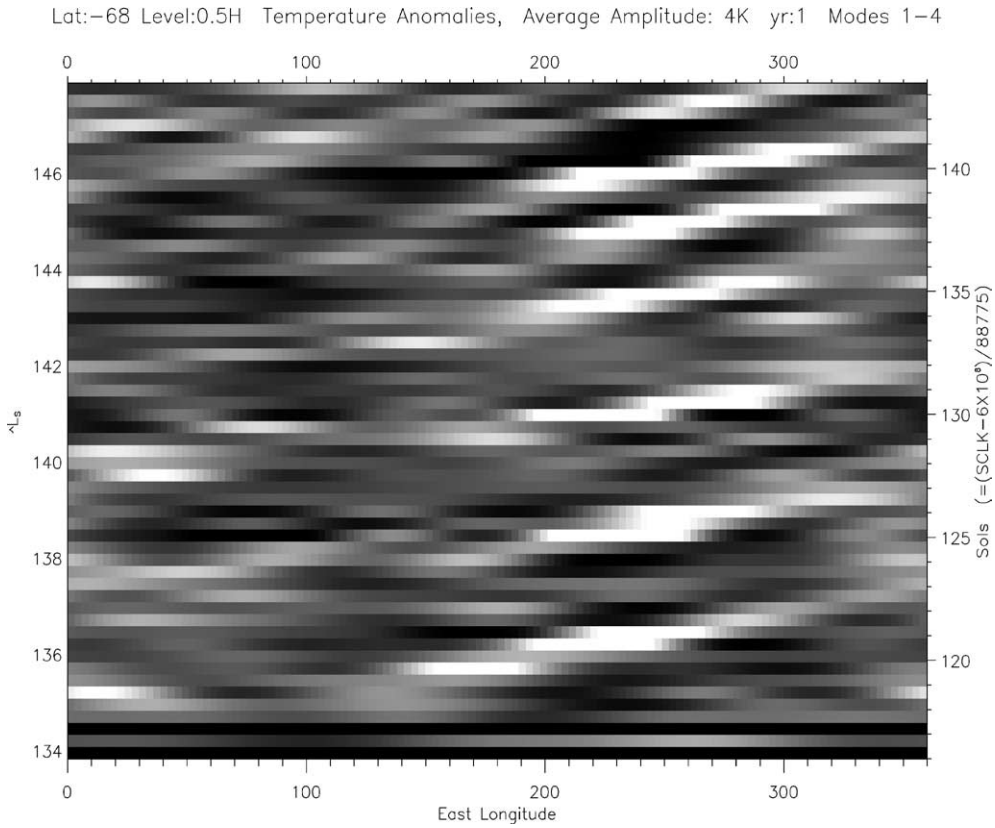

Fig. 18. Hovmoller diagram of zonal modes 1–4 for $L_s \sim 134°$–$148°$ from 68° S and one half scale height altitude (3.7 mbar). Rather than just one zonal mode, this plot includes the contributions from $m = 1$–4. A clear storm track behavior is evident, centered at about 260° E. This is also contemporaneous with the data presented in Hinson and Wilson (2002), and shows behavior similar to what they found, although with reduced amplitudes.

are slower, about 5.2 sols, and the region of accentuated wave amplitudes is centered at about 300° E. In this case, the $m = 3$ component is dominant over the other modes by about a factor of 2.

More generally, Fig. 19 shows the southern hemisphere's storm tracks during the first MGS mapping year as a function of latitude and longitude for each 30° of L_s. We have plotted the standard deviation of the time varying temperature perturbations half a scale height above 6.1 mbar (i.e., 3.7 mbar). The amplitude of the traveling waves is enhanced in regions where this quantity is large, and in that way this can be used to define the storm tracks. The region and time that were highlighted in Hinson and Wilson (2002) exhibit a notably strong storm track in this representation as well (i.e., $L_s \sim 135°$–$165°$, 60° S, 190°−320° E). This region's storm track actually appears to persist in our data from $L_s \sim 15°$ through to $L_s \sim 195°$, with nearly the same behavior in the second year (not shown). The origin of this storm track is unclear as the region is not sharply defined by topographic or thermal inertia features, however it does lie generally south of the Tharsis ridge and over Argyre. There is also a region of enhanced variability of transient temperatures in the south between about 70° S and the pole, particularly near 60° E from $L_s \sim 345°$–$15°$. This is roughly over the Chasma Australe and due south of Hellas, but the origin of this storm track is also unclear.

This phenomenon is also observed in our data in the northern traveling waves. Figure 20 shows northern hemisphere storm tracks during the second MGS mapping year. The most prominent storm track behavior occurs around northern winter ($L_s \sim 195°$–$15°$) and along the edge of the polar vortex near the surface (i.e., $\sim 50°$–$70°$ N). The exact structure of the storm tracks varies with season, and even exhibits interannual variability (not shown). However, the most persistent region of enhanced variability in our data at 6.1 mbar is near 280° E, particularly from $L_s \sim 285°$–$15°$. This storm track may arise from its association with Alba Patera, with enhanced transient wave amplitude poleward and in the lee (eastward) of the northern reaches of Alba Patera (which, with Tharsis, appear as the white column of pixels near 260° E in Fig. 20). From $L_s \sim 315°$–$15°$ of the second year, there was another clear region of enhanced transient wave amplitude between 0° and 100° E. Similarly, this region may be associated with Arabia Terra. These boundaries for the storm tracks roughly coincide with those identified from modeling by Hollingsworth and Barnes (1996). It is also somewhat difficult to compare with the results of Hollingsworth and Barnes (1996) as they present $1/2(u'^2 + v'^2)$ and $v'T'$, but not the directly measurable T'. While they identified 3 distinct storm zones in northern winter, all lying in the low altitude regions near 50° N, we only identify 2 regions, more associated with north facing

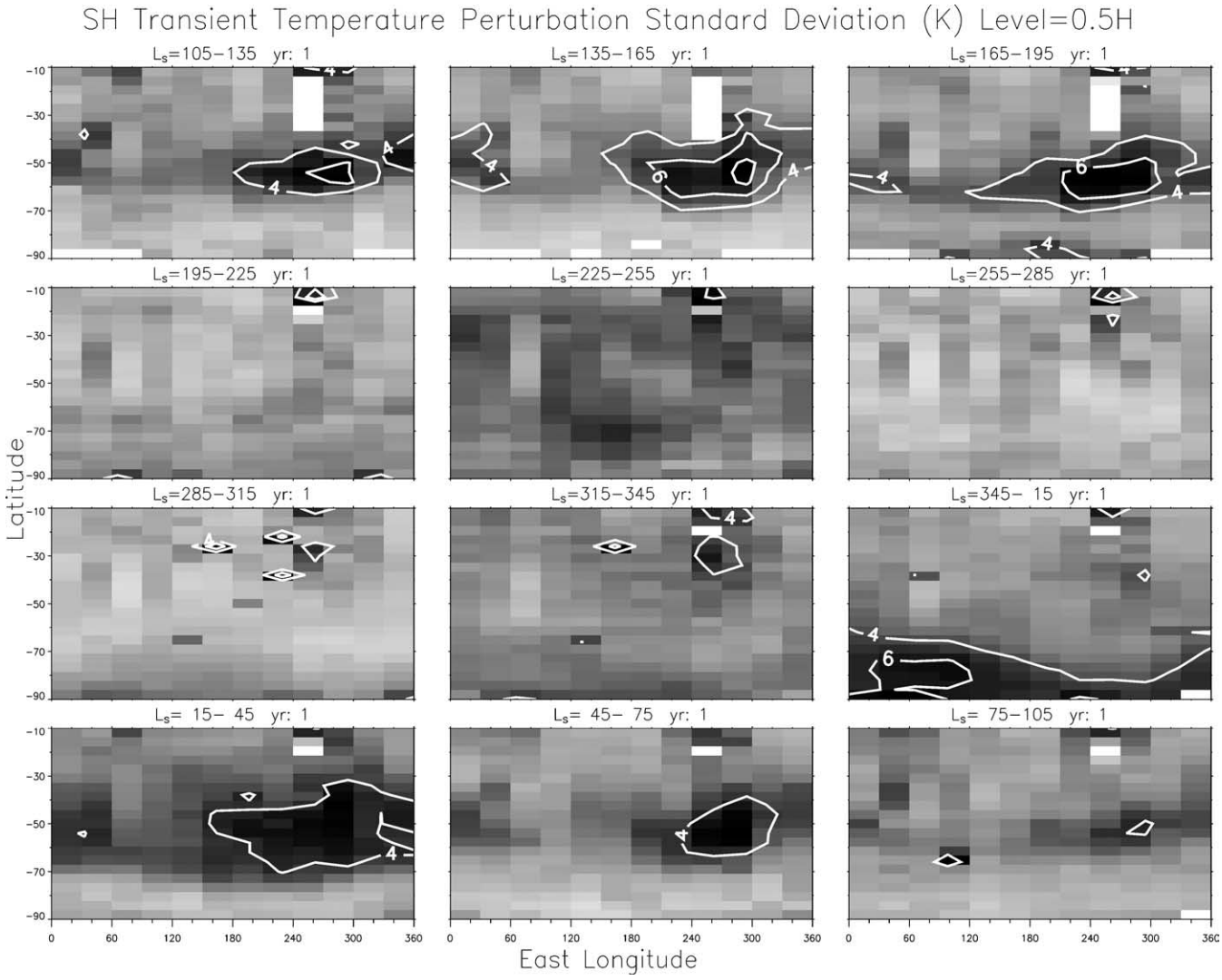

Fig. 19. Southern hemisphere latitude–longitude maps of the standard deviation of the transient temperature perturbations as a function of season for one half scale height above 6.1 mbar (3.7 mbar) during the first MGS mapping year. The overall structure of this figure is like that of Fig. 5. Dark represents high standard deviation (in units of K), and contours are shown at 4, 6, and 8 K. The storm tracks are identified by the regions of enhanced variability on these plots. A persistent storm track exists around southern winter between 45° and 65° S and 210° and 300° E.

slopes than absolute altitudes. It is possible that our western hemisphere region (centered on 300° E) may simply be an undifferentiated conglomeration of their two western hemisphere storm tracks. With this level of agreement, it seems Hollingsworth and Barnes (1996) were probably correct in identifying the meridional topographic slopes relative to isentropic slopes (Blumsack and Gierasch, 1972) as the modulator of baroclinic instability,

Another phenomenon can occur when the waves all have the same phase speed. For example, in the northern winter ($L_s \sim 275°$–$290°$) of the first mapping year, at the surface at 55° N, the $m = 1, 2$, and 3 traveling waves all have a dominant phase speed of about 52°/sol. In this case, the period of the $m = 1$ wave is 6.9 sols, the period of the $m = 2$ wave is 3.4 sols, and the period of the $m = 3$ wave is 2.3 sols (see Fig. 21). This scenario does not limit the expression of the wave to certain longitudes, but rather modifies the shape of the wave structure from a simple sinusoid. In this example, the result is a sharpening of the zonal gradients relative to the envelope of the perturbations, i.e., fronts (e.g., Tillman et al., 1979).

6. Composited structures

While all of the information needed to describe the spatial distribution of the traveling waves is contained in the amplitude-phase plots (e.g., Figs. 4, 12, and 16), it is helpful to see them rendered as well. Compositing the waves more clearly indicates the spatial structures formed by the waves, and their peak amplitudes. We did this for the Hovmoller diagrams showing the storm tracks and frontal sharpening (e.g., Figs. 18 and 21), but these are limited to one latitude and altitude. We have produced two figures showing spatial

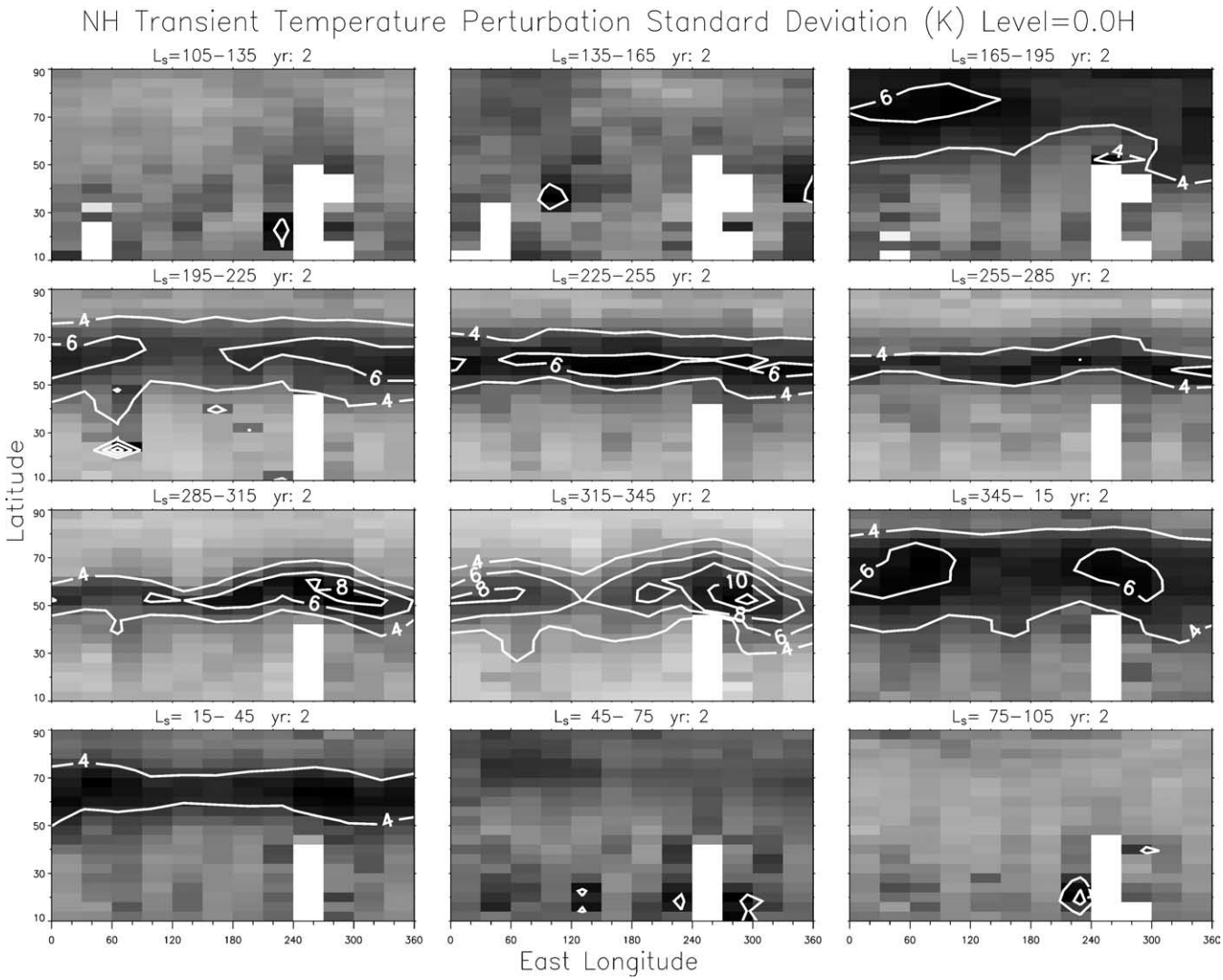

Fig. 20. Northern hemisphere latitude–longitude maps of the standard deviation of the transient temperature perturbations as a function of season at 6.1 mbar (one half scale height deeper than in Fig. 19) during the second MGS mapping year. This is analogous to Fig. 19. Note the persistent storm track around northern winter near 60° N and 280° E.

cross sections of the traveling waves in the northern hemisphere for $L_s \sim 262°$ of the second mapping year, the time of the strongest $m = 1$ (14-sol) wave observed so far. As in the Hovmoller diagrams of Figs. 18 and 21, we again composited the zonal harmonics up to $m = 4$. Harmonics higher than this are not reliably resolved in our data.

Figure 22 shows the longitude–latitude cross section of the waves at three different altitudes (0.5, 1.5, and 3.0 scale heights above 6.1 mbar) and three different times (separated by 2° of L_s, or about 3 sols at this season). Only the northern hemisphere is shown, as that is where significant wave activity is located at this time. The eastward propagation of the wave, centered at about 64° N is clearly evident in the figure (about 150° over 6 sols, consistent with the ∼ 14 sol period evident in Fig. 9), as well as its growing strength with altitude. The horizontal structure of the wave changes significantly as time progresses, making this form of display of the wave (effectively instantaneous views) poorly suited to studying the mean properties of the wave. Nevertheless, some westward tilt of the wave with latitude can be seen in this figure, particularly between about 40° and 64° N in the 1.5 H (middle) row (middle timestep). There is also a suggestion of eastward tilt with latitude for 50° to 70° N for the highest row. Finally, a nearly 180° phase shift between 50° and 70° N is evident in the lowest row (first timestep). These observations are completely consistent with the relative phase structure inferred through our analysis of the zonal wavenumber 1 portion of this data (e.g., Fig. 12 for the equivalent time in year 1, with little interannual differences in phase structure).

Figure 23 shows the same interval, but cross sections in longitude-height for three different latitudes (56°, 64°, and 72° N) and the same three times as Fig. 22. Again, the spatial structure of the wave is seen to vary considerably from

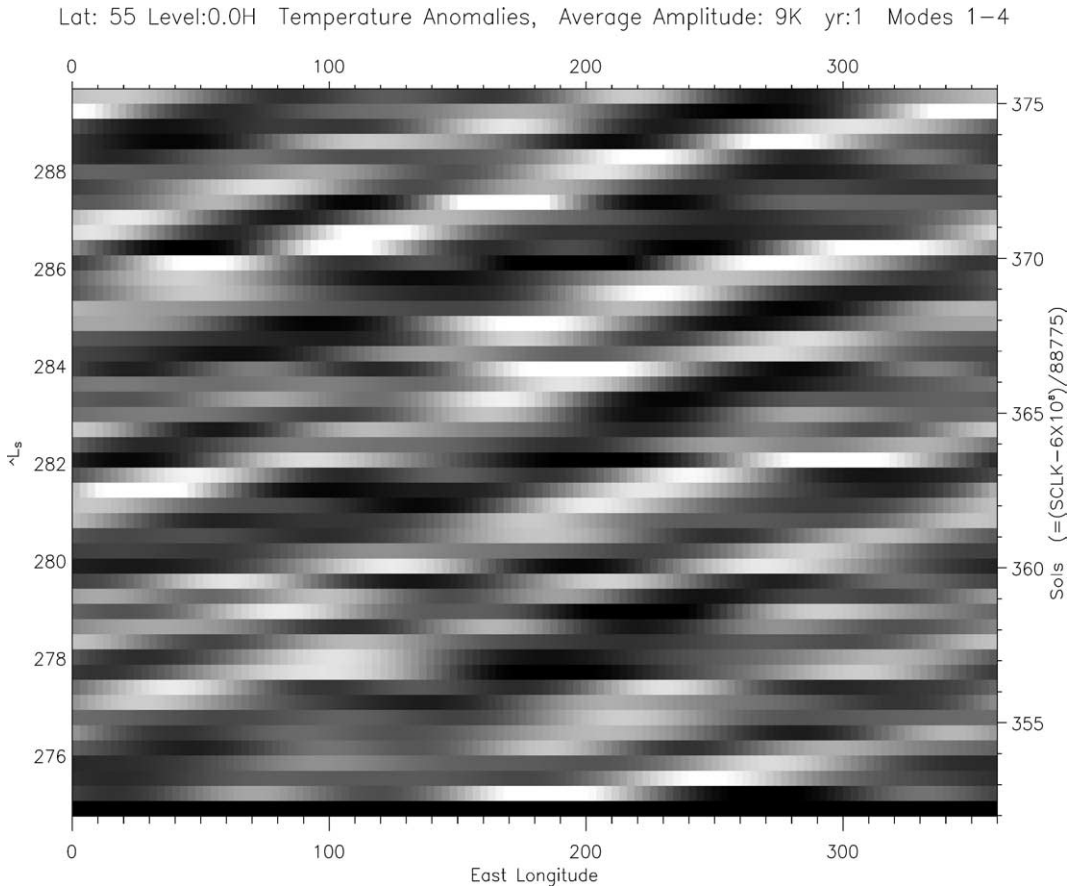

Fig. 21. Hovmoller diagram for zonal modes 1–4 from $L_s \sim 275°$–290° of the first MGS mapping year at 55° N and 6.1 mbar. In this case, we see a sharpening of zonal gradients into what might represent a frontal system propagating around the planet.

one time to the next. Nevertheless, the westward phase tilt with height is evident in the figure, particularly at lower altitudes for the northern (top and middle) rows. Here, the analysis (Fig. 12 is a very similar proxy from the previous year) suggests a phase shift of 150° or more in the bottom scale height at 72° N, completely consistent with that shown in the snapshots in Fig. 23. Similarly, a phase shift of 140° in the bottom half scale height is indicated in both figures for 64° N. A slight westward phase tilt more gradual with height of about 45° is suggested by both figures for 56° N.

7. Meridional transports

The westward phase tilts of the waves with altitude and latitude imply meridional transport of heat and negative zonal momentum (respectively) by the wave. These are important components of the heat and momentum balances of the polar regions during winter, combined with the transports due to stationary waves, the meridional circulation and the condensation flow. There is indication that the stationary wave heat transport is significantly different between the hemispheres (e.g., Banfield et al., 2003; Barnes et al., 1996; Hollingsworth and Barnes, 1996). With our results we can examine the symmetry and magnitude of the heat and momentum fluxes due to the traveling waves.

It is important to note that our calculations of the heat and momentum transports are limited by our poor ability to resolve wave amplitudes and their phase variations in the bottom scale height. The winds at altitude are based on integrations of the conditions below, making it possible that our results could be skewed because of our inability to resolve fully the bottom of the atmosphere. Additionally, we are forced to make an assumption for the surface winds, which are unconstrained from the temperature profiles. We assume zero winds near the surface, an assumption which is clearly not always correct, but which should have negligible influence at higher altitudes. We have used gradient-wind balance to compute the zonal mean zonal wind, as the Rossby number is near or exceeds 1 in the strong jets. We have also used a new approach to solve for the zonal and meridional perturbation winds which is consistent with the assumptions used in the gradient wind approximation for the zonal mean zonal wind. This approach is detailed in the appendix. Unfortunately, this approach is not able to return a balanced solution for the winds in certain locations, further eroding our capability to estimate the wave transports. This problem becomes more serious for the higher wavenumbers, so we limit our traveling wave transport discussion to $m = 1$. Sim-

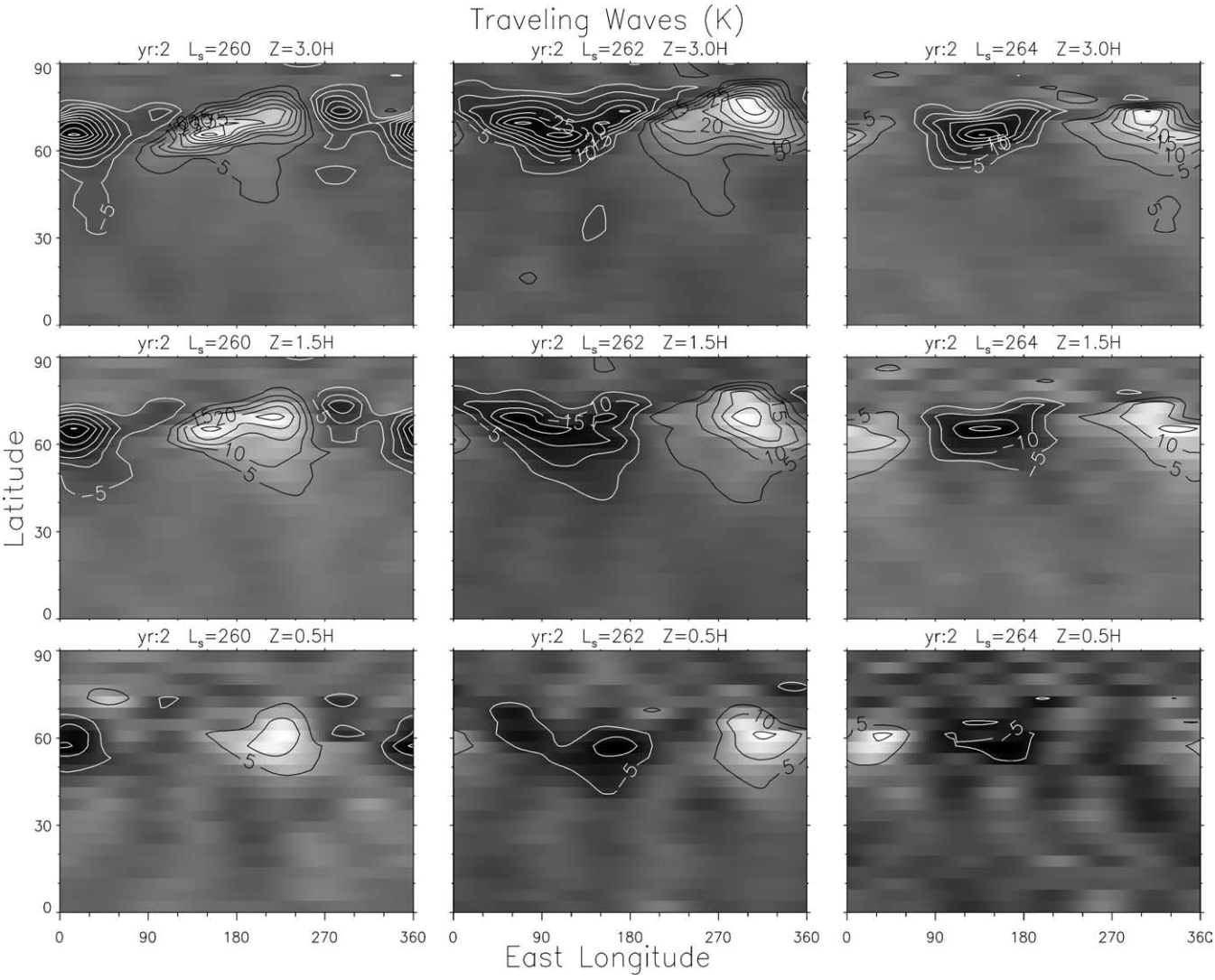

Fig. 22. Latitude–longitude maps of the traveling wave temperature anomalies constructed from zonal modes 1–4 for $L_s \sim 260°$–$264°$ of the second MGS mapping year. Each panel in this figure is a map of the perturbation temperatures at a given altitude and time as a function of latitude and longitude. All longitudes are shown, but only in the northern hemisphere. Altitudes decrease reading down columns in this plot, from 3 scale heights altitude to 1.5 scale heights, to 0.5 scale heights altitude at the bottom. Time increases to the right in this figure, from $L_s \sim 260°$–$262°$–$264°$, or about 3 sols between each column. The temperature perturbations are indicated by the gray scale (bright=hot) and the contours (with contours at 5 K intervals except 0). Note the eastward propagation of the wave with time, and its greater amplitude with height.

pler (geostrophic) estimates of the winds and their transports suggest that the $m = 1$ transports usually dominate those of the higher wavenumbers, especially near winter solstice when the $m = 1$ components are large and the transports are large as well. Because of this, we believe that reporting the $m = 1$ results still captures the essence of the traveling wave transports, at least at higher altitudes. Nevertheless, there are regions on our plots where the solutions are not well founded. These regions are clearly marked on the diagrams, and their effect considered in our conclusions.

The meridional heat flux is given by $\rho C_p \overline{v'T'}$, and the meridional momentum flux is given by $\rho \overline{u'v'}$. Respectively, these two terms then make up the vertical and meridional components of the quasi-geostrophic Eliassen–Palm flux. We have chosen to present the divergence of the Eliassen–Palm flux, as that is the net effect of the heat and momentum fluxes that contribute to accelerating the zonal flow. Just examining either the heat or momentum transport alone could overlook a partial cancellation between them in their net effect on the zonal flow. For a discussion of the Eliassen–Palm (or EP) flux, see, e.g., Andrews et al. (1987). While we have done a careful job with the zonal mean and perturbation winds in light of the large Rossby number, our forms for the EP flux are still quasi-geostrophic. Because of this, our fluxes may be in error in regions where the Rossby number is large.

In our results, there are three different influences that the $m = 1$ traveling waves have on the zonal jets: a decaying and broadening of the core, a tendency to move the core of the jet poleward, and a tendency to move the core of the jet equa-

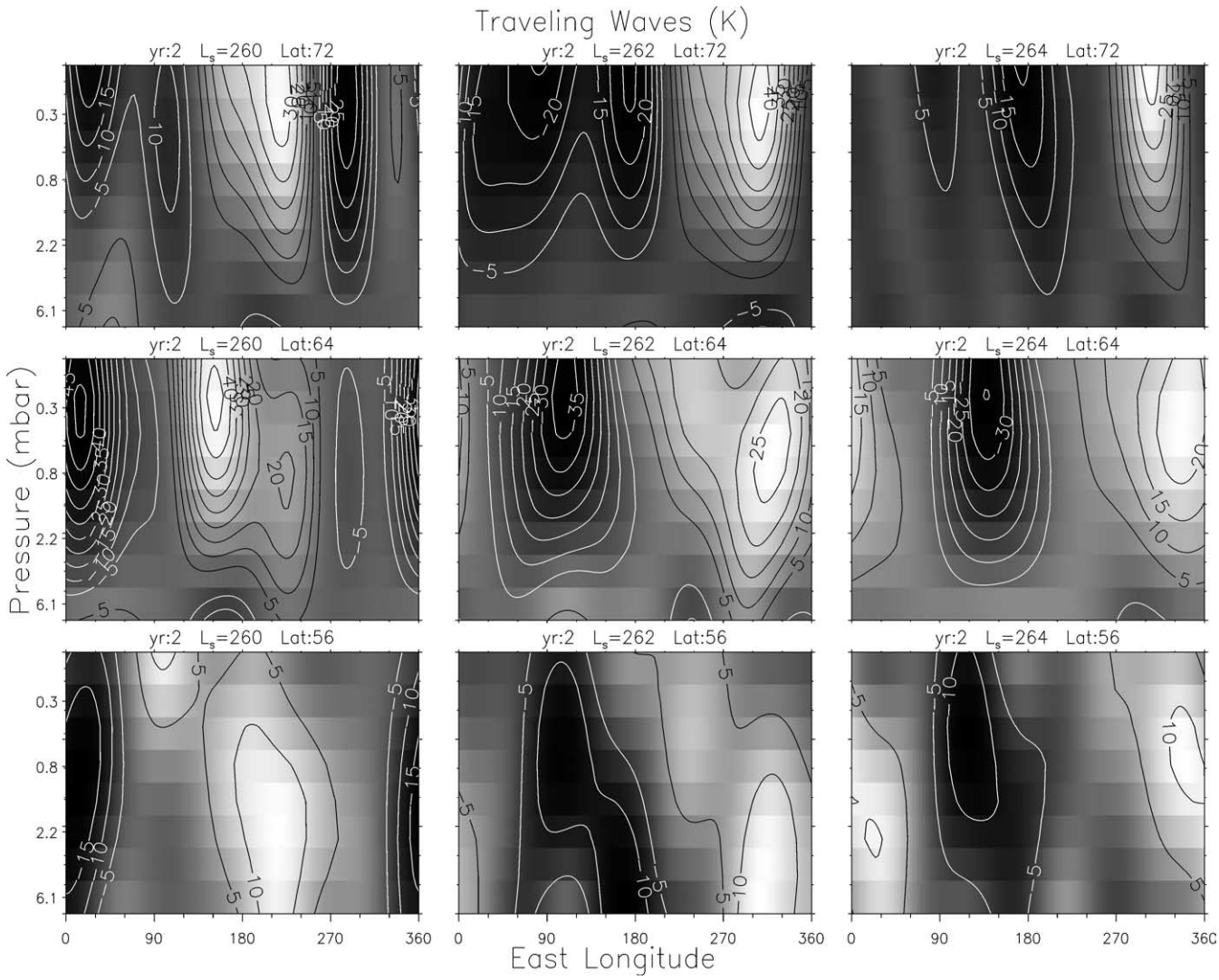

Fig. 23. Longitude–altitude cross sections of the traveling wave temperature perturbations from $L_s = 260°$–$264°$ of the second MGS mapping year. This figure is analogous to Fig. 22, but shows vertical cross sections with longitude rather than map views of the perturbations. Time still increases to the right, but latitude decreases reading down a column. The top column is at 72° N, the middle at 64° N and the bottom at 56° N, spanning the main region of strong traveling waves. Again, note the eastward propagation of the waves and their increasing strength with altitude.

torward. In the 9 of our 24 seasonal bins where the $m = 1$ waves imparted a significant acceleration on the northern hemisphere zonal jet, we see the waves decaying and broadening the jet in 4 of them, shifting it equatorward in 3 of them and shifting it poleward in 2 of them. The effects are strongest centered on the northern winters, when the waves are strongest there, but beyond that no systematic seasonal change from one behavior to another is evident. Typical accelerations for the 3 different behaviors were between -32 and 20 m/(s sol). In the southern hemisphere, significant effects from the $m = 1$ traveling waves were only seen in 2 of our seasonal bins, both during the first MGS mapping year. In both cases, the $m = 1$ traveling waves appeared to move the southern hemisphere zonal jet equatorward, with typical accelerations between about -4 and 5 m/(s sol). This behavior was observed from $L_s \sim 45°$–$105°$ of the first MGS mapping year.

The EP flux divergence is indicative of the net effect of the meridional heat *and* momentum fluxes, but it is of note that all of our results with significant eddy accelerations are dominated by the meridional momentum flux. That is, the component of the EP flux divergence that is due to the meridional momentum flux is notably larger than that due to the meridional heat flux where we can discern them. This suggests that while the ($m = 1$) eddies themselves are drawing energy both from the meridional shear of the zonal wind and the meridional temperature gradient (i.e., they are mixed barotropic/baroclinic), they are mainly powered via the barotropic conversion of zonal mean kinetic energy into eddy kinetic energy. This differs somewhat from the model results presented in Barnes et al. (1993). They noted the mixed character of their modeled waves, but found the eddy momentum fluxes only 50% as large as the eddy heat fluxes, and thus a dominance by baroclinic processes. The explana-

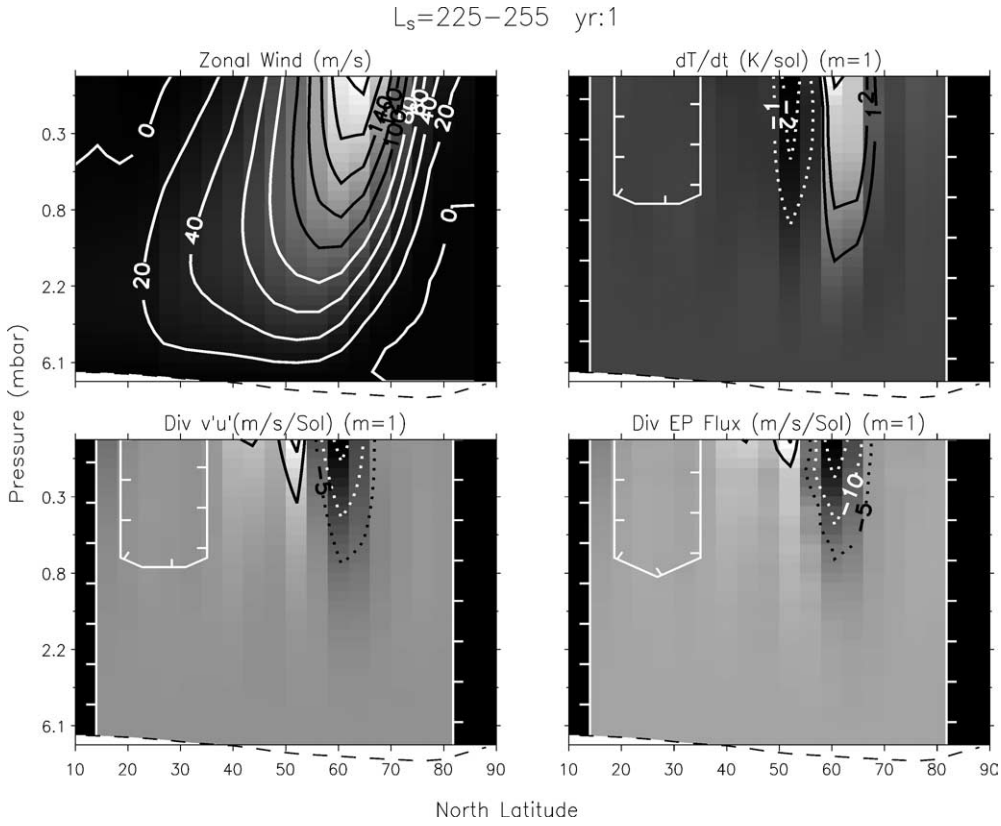

Fig. 24. $m = 1$ traveling eddy accelerations to the mean flow for $L_s \sim 225°$–$255°$ of the first mapping year. Regions with hatching on the thin solid contours are regions in which the perturbation winds (and derived quantities) could not be derived. The lower right panel is the divergence of the EP flux, which represents an acceleration to the zonal mean zonal wind from the $m = 1$ traveling eddies. Comparing this with the upper left panel, the zonal mean zonal wind, suggests that the jet is being moved equatorward by the traveling eddies. The upper right shows the divergence of meridional eddy heat flux, while the lower right shows the divergence of the meridional eddy momentum flux. Both of these contribute to the divergence of the EP flux, but clearly the momentum flux dominates.

tion of this may lie in our insensitivity to structure in the bottom scale height. As noted above, the majority of the meridional heat flux in their modeling was observed in the bottom scale height, the traditional source of baroclinic instability near the surface. Because we do not resolve that region, our results may be skewed against the baroclinic energy conversions that may be occurring in Mars' atmosphere.

The lower right panel of Fig. 24 shows the divergence of the EP flux for $m = 1$ waves for $L_s \sim 225°$–$255°$ of the first MGS mapping year. This is an example where the net effect of the traveling waves was to try to move the jet core equatorward. This can be seen by comparing with the zonal mean zonal wind in the upper left panel. There is acceleration evident on the equator-ward flank of the jet core, and deceleration evident in and on the poleward flank of the jet core. Hence, the effect of the traveling waves at this time was to move the jet equatorward and slightly decrease its strength. This behavior differs from that noted by Haberle et al. (1993) in their GCM modeling of northern winter, where they found the waves effectively pushing the jet poleward. While the spatial distributions of accelerations differed in their work, the amplitudes are roughly similar (see their Fig. 35b). Also shown in Fig. 24, in the upper right panel is the divergence of the meridional eddy heat flux from the $m = 1$ traveling wave. Finally, in the lower left, we have plotted the accelerations due to just the meridional momentum flux from the $m = 1$ wave, i.e., the divergence of the $v'u'$ correlations. Comparing this with the total EP flux divergence, it is clear that this is the dominant term in the total eddy accelerations at this time.

Figure 25 is very similar to Fig. 24, except that it is for the *second* MGS mapping year, for $L_s \sim 255°$–$285°$. This is another example of the waves shifting the polar jet equatorward and significantly damping it. The eddy accelerations are strongly negative (30 m/(s sol)) right at the core of the zonal jet. These are the largest traveling wave eddy accelerations seen in our data, coincident with the largest $m = 1$ traveling waves. This should cause the jet to quickly decrease in peak intensity and move south. These large accelerations due to the waves are apparently balanced by another opposing torque (perhaps the mean meridional circulation or mountain torques), as the jet does not change as quickly as these would indicate. The lower left panel of Fig. 25 demonstrates that again, it is the eddy momentum flux divergences that dominate the total eddy accelerations at this time. Finally, the upper right panel shows the correlations between v' and u'. The divergence of this field is the lower left panel. We have chosen to plot $v'u'$ directly to highlight the merid-

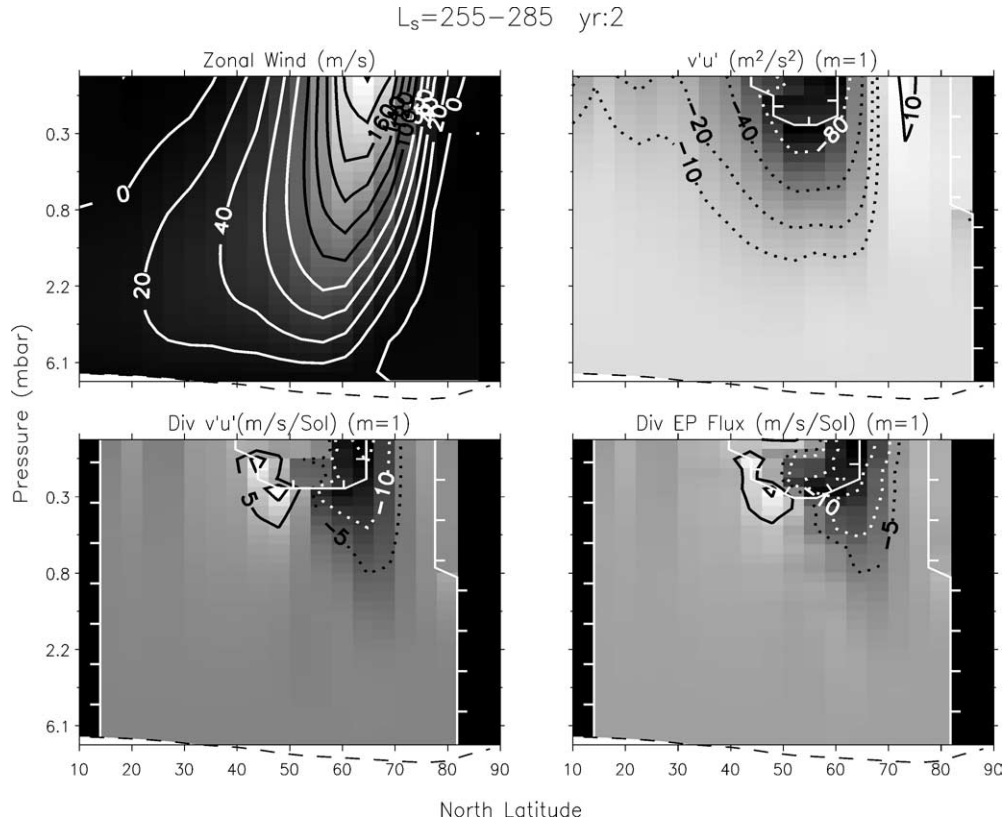

Fig. 25. $m = 1$ traveling eddy accelerations to the mean flow for $L_s \sim 255°$–$285°$ of the second mapping year. This figure is analogous to Fig. 24, but for the second mapping year and slightly later, in the middle of winter. In this case, the eddies are again acting to move the jet equatorward, and weaken it, with strong decelerations of order 30 m/(s sol) at the peak of the jet. Again, the meridional eddy momentum flux divergence dominates over the meridional eddy heat flux divergences. This time, the upper right figure is the meridional momentum fluxes rather than the heat flux divergences to highlight their significant values all the way down to tropical latitudes.

ional momentum flux that is still significant even at tropical latitudes. This is consistent with the modest amplitudes for the $m = 1$ traveling wave we saw at this time (and also the previous year) extending to the tropics at higher altitudes. As discussed in Barnes et al. (1993) and Wilson et al. (2002), this is likely a connection between the eddies centered on the polar front and inertial instabilities in the northern tropics.

We can also compare the EP flux divergences (zonal mean zonal wind accelerations) with those induced by the stationary waves reported in Banfield et al. (2003). In that work, only heat fluxes were reported, but the same EP flux calculations can be carried out on the stationary wave fields as has been done here. Again, the cleanest results are only for $s = 1$ (where we use s for the stationary waves' zonal wave number), but simpler (geostrophic) estimates suggest that $s = 1$ and $s = 2$ effects are comparable and that both dominate $s = 3$. It turns out that for the stationary waves, most of the significant accelerations occur in the southern hemisphere, where the weaker jet produces less problems for our perturbation wind solver. Thus, while the $s = 2$ accelerations in the north are poorly defined in our analysis, the bulk of the accelerations (those in the south) are still fairly well determined with our analysis. So as with the traveling waves, this analysis captures the essence of the EP flux divergences due to the stationary waves.

The total accelerations given by the $s = 1$ and $s = 2$ waves (not shown) are typically of order 15 m/(s sol), with a maximum of about 40 m/(s sol) during the second mapping year southern winter ($L_s \sim 45°$–$135°$). The stationary waves tended to tighten and strengthen the south polar jet during southern winter. In early southern winter, their effect was to align the jet more vertically, that is, strengthening the jet in its core at lower altitudes, and moving it equatorward at higher altitudes effectively tending to remove the poleward tilt with height of the jet. In late southern fall and early southern spring, the stationary waves tended to move the jet equatorward. As with the traveling waves, the meridional momentum fluxes dominate the overall EP flux divergences for the stationary waves, although meridional heat fluxes in the southern stationary waves are significant, producing heating rates as high as ~ 8 K/sol during southern winter. These significant heat fluxes are in agreement with the observations of Banfield et al. (2003) and the modeling in Barnes et al. (1996) and Hollingsworth and Barnes (1996). In summary, the typical accelerations imparted on the northern polar jet due to the stationary eddies are much smaller than those due to the traveling eddies. In the south, the sit-

uation is the opposite, where the stationary waves dominate the zonal jet accelerations, and the traveling wave effects are much smaller.

8. Instabilities

In this section we will present some simple criteria derived from the data that have a bearing on identifying where and when the instabilities that generate the observed traveling waves likely are found. For a more complete discussion, see Barnes et al. (1993), and also Wilson et al. (2004, in preparation).

Barnes et al. (1993) noted that in their models, the traveling waves had amplitude extending all the way into the tropics (and perhaps midlatitudes) of the summer (southern) hemisphere. This is consistent with our results for late northern fall and early northern winter, when the $m = 1$ wave is seen to extend slightly into the southern tropics at altitudes above about 2.5 scale heights. Barnes et al. suggested that this was a form of inertial instability that was perhaps forced by the midlatitude Rossby waves. They presented a plot showing an indicator of inertial instability (basically $f \times$ PV), which was negative at high altitudes just north of the equator, indicating instability there. Their modeled temperature perturbations in the tropics were larger than what we observed, but it is likely that we are seeing an attenuated version of the real waves at these altitudes. Wilson et al. (2002) noted the tropical extension of the $m = 1$ wave in the first year of MGS TES data, and also discussed it in the context of inertial instability. They argued that it was different than the phenomenon identified in Barnes et al. because Wilson et al.'s modeling did not show the fine vertical layering in the eddy meridional wind that Barnes et al. did. Barnes et al.'s results were also all dominated by what we would call a fast $m = 1$ wave ($\sim$ 6 sol period), while the waves that extend into the tropics are most definitely slower ($\sim$ 10–30 sol period).

In our data, at those times when wave amplitude bridges from tropics to midlatitudes, the mean structure above the tropics does not usually appear to be unstable to inertial instability. Figure 26 shows the quantity $f \times$ PV (where PV is Ertel's PV, calculated via the angle between constant Θ and angular momentum surfaces as in (Allison et al., 1994), equivalent to $(\zeta \cdot \nabla\Theta)/\rho$ (e.g., Gill, 1982) where ζ is the absolute vorticity, Θ is the potential temperature, and ρ is the density) for $L_s \sim 255°$–$285°$ of the second MGS mapping year. There is a region where inertial instability is clearly permitted (the plotted quantity goes negative), but it lies above 3 scale heights over 50°–60° N. This time interval is representative of the map of this quantity in northern winter. In the tropics, this quantity is typically positive, suggesting inertial instability is not generally possible there. However, a notable exception is $L_s \sim 255°$–$285°$ of the first year where do we see inertial instability possible at altitude in the southern tropics.

While in general we do not directly see the inertial instability criterion met in the tropics during northern late fall-winter, it is worth noting that the value is near zero in that region. Presumably this suggests that it would not require much of an external forcing to yield behavior similar to a true inertial instability. Additionally, our PV fields are based on a

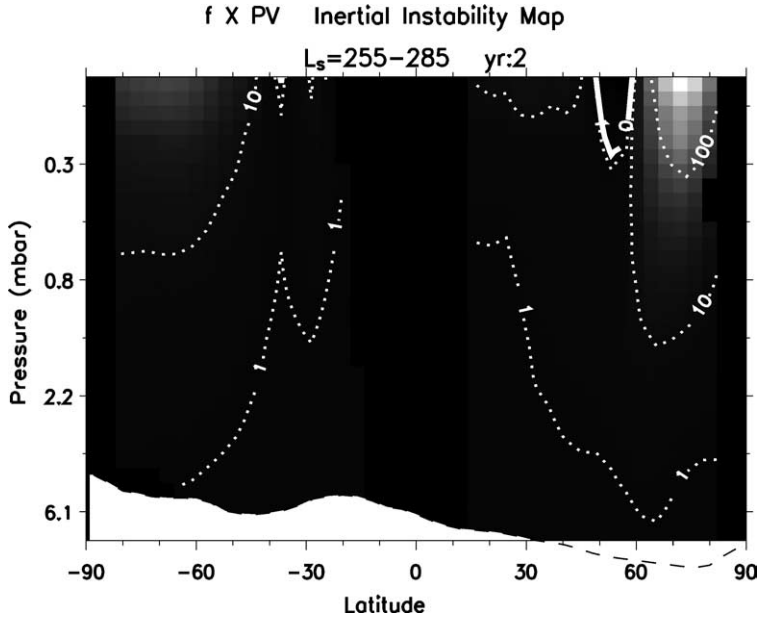

Fig. 26. Inertial instability map for $L_s \sim 255°$–$285°$ of the second mapping year. Contours and the grayscale represent the quantity $f \times$ PV, which when it goes negative suggests that inertial instability is possible. Contours are at 0, 1, 10, and 100, with the 0 contour highlighted. This quantity goes negative frequently on the equatorward side of the polar jets, but only rarely in the tropics. Nevertheless the value is small in that region, suggesting that either errors in our surface wind assumption or a moderate perturbation could trigger inertial instabilities in the tropics, possibly explaining our $m = 1$ traveling wave amplitudes in that region.

wind field assumed to be zero at the surface and in gradient wind balance. If this is not the case (and it likely is not), then our PV could be significantly perturbed, particularly near the equator. Thus, we conclude that the hypothesis presented in Barnes et al. (1993) and Wilson et al. (2002) of a connection between the midlatitude eddies and the tropics with a form of inertial instability is plausible. This is indeed bolstered by the one case where the tropical instability is seen while these slow waves propagate there from $L_s \sim 255°$–$285°$ of the first year. We speculated above that this phenomenon is in fact a fused Rossby–Kelvin wave, each component propagating in the latitude of its own preferred zonal wind regime. Presumably the structure of the separate ducts conspire to maintain spatial coherence in the fused normal mode, allowing it to propagate as one.

It is of note that we also occasionally see evidence of inertial instability in the southern hemisphere, typically during late southern summer and fall, and more frequently during the second year. This appears near 40° S, also at altitude. In the example in Fig. 26, it just barely sneaks into our results at the top of our domain near 37° S. Nevertheless, we do not find the same strong, slow waves in the south as are evident in the north, suggesting that inertial instability alone is not enough to produce such strong, slow waves. This again suggests a coordination between the regions of inertial instability and the properties of the polar jet that control the formation of these waves.

The EP flux divergences indicated that baroclinic and barotropic energy conversions were taking place in the vicinity of the polar vortex. The quasi-geostrophic necessary condition for instability is that either the meridional gradient of the PV is less than zero somewhere in the domain, or else the vertical shear of the zonal wind must be positive at the lower boundary (e.g., Pedlosky, 1979). We will assume for purposes of the following quantitative discussion that the Ertel PV gradient, rather than the quasi-geostrophic PV gradient is the appropriate instability indicator for the relatively high speed martian flow. Positive vertical shear of the zonal wind at the lower boundary is frequently satisfied, but the meridional PV gradient is not always greater than zero throughout the domain. In fact, it frequently has zero crossings on the flanks of the polar jets. This is the traditional source of barotropic instability, and its widespread presence near the strong winter jets is consistent with our findings of its dominance in the energy conversion from zonal mean to eddy kinetic energy.

Figure 27 shows meridional cross sections of several quantities at the time of the strongest observed $m = 1$ trav-

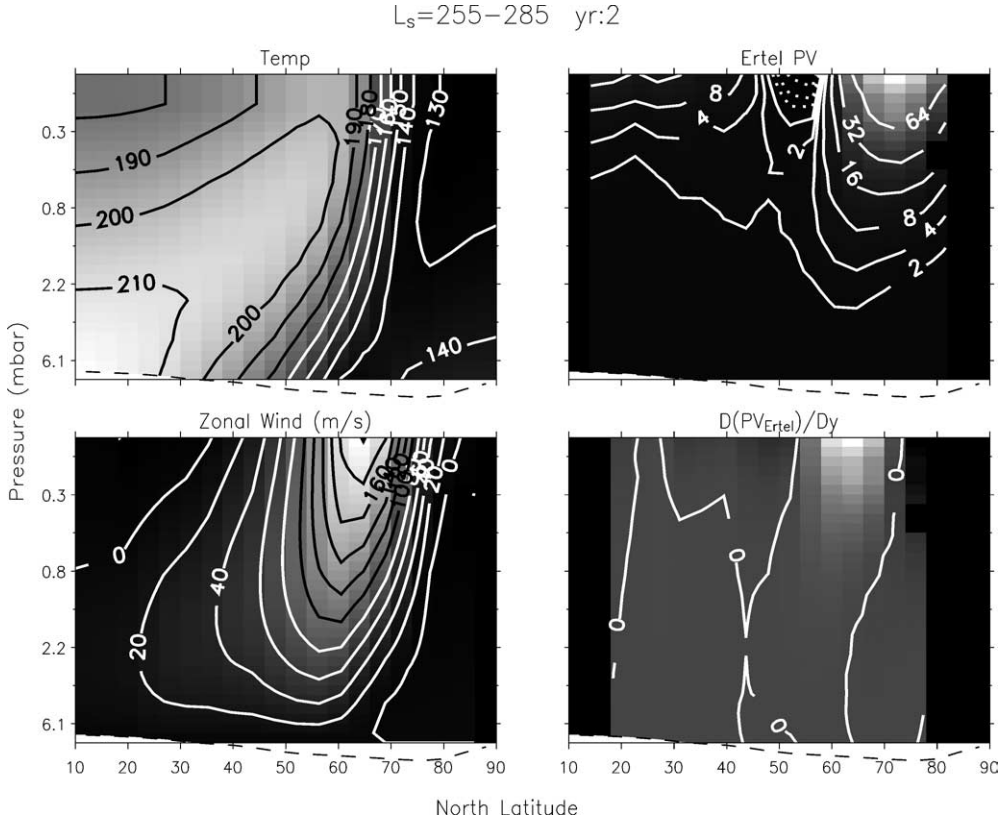

Fig. 27. Instability map for $L_s \sim 255°$–$285°$ for the second mapping year. We have plotted the zonal mean temperature in the upper left, and the resultant zonal mean zonal wind in the lower left, the Ertel PV in the upper right, and finally the meridional gradient of the PV in the lower right. For all quantities, grayscales and contours indicate the values. Units for the PV are in terms of $\Omega g 200$ K/6.1 mbar, where Ω is the angular rate of the planet's rotation, and g is the surface gravity. The meridional gradient of the PV is only indicated with a zero contour, as sign changes in this quantity are indicative of possible instability. Here two regions of instability are present surrounding the polar jet, one covering all altitudes on the poleward flank of the polar jet, and the other covering almost all altitudes on the equatorward flank of the polar jet. Note that unlike the Earth, PV decreases again toward the pole away from the polar jet.

eling waves in the second mapping year, $L_s \sim 255°$–$285°$. Shown in Fig. 27 are the temperature (upper left), zonal mean zonal wind (lower left), Ertel's PV (upper right) and its meridional gradient (lower right). This interval is an extreme case, with the strongest shears found in our data set, but it is grossly representative of generic PV structure for both hemispheres around winter. Unlike on Earth, where the PV inside the polar vortex reaches a maximum value at the center, on Mars instead it has its maximum value in the polar jet and decreases toward the pole. The effect of this is that the meridional gradient of PV is negative on both flanks of the jet. The poleward region of $dPV/dy < 0$ extends all the way to the surface, creating a large region where instabilities can develop. In the jet itself, the strong meridional shears cause the PV to have a region of negative meridional gradient on the equatorward flank as well. This region of possible instability does not typically reach the surface, but rather is usually confined above about 2 scale heights altitude. In this extreme example, it has connected with a similar region near the equator, and very nearly reaches another unstable region at the surface. The poleward region of possible instability lies right along the polar front, while the equatorward, upper region lies along the core of the warm horn due to the meridional overturning.

We hypothesize that the segregation of these two large regions of possible instability on either side of the polar jet, one reaching the surface and the other typically not may be the cause of the dual nature of the traveling waves seen at certain times in our analysis. Occasionally we identified distinct waves, with different phase speeds but the same zonal wavenumber ($m = 1$), propagating in the vicinity of the polar jet (e.g., Figs. 3, 5, and 9). Typically, one was concentrated at altitude and the other closer to the surface. In Figs. 5 and 9, it is even clear that the wave concentrated at altitude is typically equatorward of the lower wave. Thus we suggest that these two separate regions of long-lived instability may generate their own traveling waves that at times have independent phase speeds. The faster waves, including the fast $m = 1$ waves and all the $m = 2, 3$ waves may be rooted to the region of instability on the poleward edge of the jet, exploiting both baroclinic and barotropic energy conversions. The slow waves, only recently identified in TES data (Wilson et al., 2002, and this work) may be rooted in the region of instability on the equatorward side of the jet, and also incorporating regions of inertial instability extending into the tropics. The slow waves then are a combination of mixed barotropic/baroclinic energy conversions and inertial instabilities.

9. Conclusions

We have characterized the annual evolution of martian atmospheric traveling waves in the MGS TES data set from the first two martian years of mapping. There is a high degree of repeatability between the two years. They are dominated by strong low zonal wavenumber, zonally coherent waves with amplitudes peaking in the vicinity of the polar jets. The strongest amplitudes are seen in late northern fall and early northern winter, dominated by zonal wavenumber $m = 1$. These waves have amplitudes up to about 20 K, are vertically extended (at least 4 scale heights), and occasionally extend even into the tropics. Typical periods for the $m = 1$ waves are of order 2.5 sols to 30 sols, with secular trends in the period seen in both years. The coherence time of the slow waves can be up to 80 sols or more. The fastest $m = 1$ waves may actually be linked to dominant $m = 2$ or $m = 3$ waves, creating storm tracks or frontal shapes. There is a tendency for the dominant wave period to abruptly change, similar to that identified in Collins et al. (1996). Much weaker waves were identified in the south, with amplitudes of less than about 3 K, but similar spatial distribution and slightly shorter periods for $m = 1$. Traveling waves with $m = 2$ and $m = 3$ are also seen, but their amplitudes are typically limited to about 4 K, and are generally more confined near the surface than the $m = 1$ waves.

Some evidence of storm tracks has been identified in the data, with accentuated weather-related temperature perturbations near longitudes 200° to 320° E for both the southern and northern hemispheres near latitude ±60° at the surface. Away from the surface, the storm track behavior was notably weaker, but still occasionally identifiable. Some evidence was also found for a sharpening of longitudinal gradients into what may be frontal systems. Occasionally, waves of $m = 1, 2$ or 3 were seen to move with the same phase speed, as a group, perhaps indicative of frontal systems.

In addition to the amplitudes and dominant phase speeds of the traveling waves in the data set, we have also quantified the relative phases of the waves in an average sense over moderate intervals. These allowed us to infer the meridional heat and momentum fluxes, and then EP fluxes for the $m = 1$ waves. We generally found the waves to extract energy from the zonal mean winds, sometimes damping and broadening the jets, other times trying to push them poleward or equatorward. Rarely did we find the traveling waves strengthening the zonal jet. Decelerations of the zonal jet from the $m = 1$ traveling waves of order 30 m/(s sol) were measured. However, as the jet strength clearly does not change this fast, other forcings must resupply energy to the jet that is lost to the eddies. In the north, it is the traveling waves that generate the greatest EP flux divergences, while in the south, the stationary waves dominate. The waves, in the regions accessible to TES retrievals (i.e., above 1 scale height altitude), extract energy from the jet predominately through barotropic processes, but their character is overall mixed barotropic/baroclinic. Inertial instabilities may exist at altitude on the equatorward flanks of the polar jets, and marginal stability extends through to the tropics. This may explain the coordination of the tropical behavior of the waves with that centered along the polar jet, consistent with the ideas expressed in Wilson et al. (2002) and similar to those in Barnes et al. (1993). Large regions with the meridional gradient of

PV less than zero exist throughout the year, but are strongest near winter solstice. Poleward of the jet, this region extends to the surface, equatorward it usually does not. These regions, satisfying a necessary criterion for instability, likely explain the genesis of the waves, and perhaps also their bimodal character between surface (faster waves) and altitude (slow $m = 1$ waves).

Acknowledgment

This work was supported by NASA's Mars Data Analysis Program.

Appendix A

A.1. Gradient wind-perturbation winds

For Mars, the zonal mean winds are large enough that the Rossby number is not small. In our results, it exceeds 1 in the cores of the winter polar jets during the second year of MGS mapping. Because of this, the usual wind balance of geostrophy is not accurate. Instead, gradient wind balance must be used. In this case, not only are pressure forces and Coriolis forces in balance, but inertial forces must also be included in the mix. The winds are strong enough that centripetal accelerations cannot be ignored. We have used gradient wind balance to compute the zonal mean zonal winds, but a new scheme must be developed to compute the perturbation winds beyond the zonal mean winds. This scheme must also include inertial terms in the balance.

We start with the zonal and meridional momentum equations. We will ignore both vertical winds and time derivatives; generally a safe assumption for the regions studied in this work. Using the standard symbols, we define the zonal wind with a zonal mean part and a perturbation part: $U(x, y, z) = \bar{U}(y, z) + u'(x, y, z)$, and a meridional wind which has no zonal mean (we ignore the condensation flows) but does have a perturbation part: $V(x, y, z) = v'(x, y, z)$. The perturbation winds are assumed to be small compared to the zonal mean zonal wind $\bar{U}$. Similarly, the pressure can be expressed as a zonal mean part and a perturbation part: $P(x, y, z) = \bar{P}(y, z) + p'(x, y, z)$. Inserting these definitions into the zonal and meridional momentum equations, and ignoring second order terms, to zeroth order we find the equation for gradient wind balance for the zonal mean zonal wind. To first order, we find a set of coupled equations for the perturbation winds:

$$\bar{U}\frac{\partial u'}{\partial x} + \frac{1}{\rho}\frac{\partial p'}{\partial x} = v'\left(f - \frac{\partial \bar{U}}{\partial y} + \bar{U}\frac{\tan\phi}{a}\right), \tag{A.1}$$

$$\bar{U}\frac{\partial v'}{\partial x} + \frac{1}{\rho}\frac{\partial p'}{\partial y} = u'\left(-f - 2\bar{U}\frac{\tan\phi}{a}\right), \tag{A.2}$$

where ρ is density, $f = 2\Omega\sin\phi$, Ω is Mars' angular rotation rate, ϕ is latitude, a is Mars' radius, and the cardinal directions have their usual meaning.

We then convert to isobaric coordinates, using

$$\frac{1}{\rho}\frac{\partial p'}{\partial x}\bigg|_z = \frac{\partial \Phi'}{\partial x}\bigg|_P \quad \text{and} \quad \frac{1}{\rho}\frac{\partial p'}{\partial y}\bigg|_z = \frac{\partial \Phi'}{\partial y}\bigg|_P,$$

where Φ' is the perturbation component of the geopotential. We also multiply through by $P\partial/\partial P$, and use

$$\frac{\partial \Phi}{\partial P} = -\frac{RT}{P} \quad \text{and} \quad P\frac{\partial}{\partial P} = \frac{\partial}{\partial \ln P}.$$

This yields:

$$\begin{aligned}\frac{\partial \bar{U}}{\partial \ln P}\frac{\partial u'}{\partial x} + \bar{U}\frac{\partial^2 u'}{\partial \ln P \partial x} - R\frac{\partial T'}{\partial x} \\ = \frac{\partial v'}{\partial \ln P}\left(f - \frac{\partial \bar{U}}{\partial y} + \bar{U}\frac{\tan\phi}{a}\right) \\ + v'\left(\frac{\tan\phi}{a}\frac{\partial \bar{U}}{\partial \ln P} - \frac{\partial^2 \bar{U}}{\partial \ln p \partial y}\right),\end{aligned} \tag{A.3}$$

$$\begin{aligned}\frac{\partial \bar{U}}{\partial \ln P}\frac{\partial v'}{\partial x} + \bar{U}\frac{\partial^2 v'}{\partial \ln P \partial x} - R\frac{\partial T'}{\partial y} \\ = \frac{\partial u'}{\partial \ln P}\left(-f - 2\bar{U}\frac{\tan\phi}{a}\right) - 2u'\frac{\tan\phi}{a}\frac{\partial \bar{U}}{\partial \ln P}.\end{aligned} \tag{A.4}$$

Note that the temperature has also been broken down into a zonal mean part and a perturbation part, $T(x, y, z) = \bar{T}(y, z) + T'(x, y, z)$. These form a set of coupled differential equations for u' and v'.

Because our analysis is separated into zonal harmonics, it is useful to consider the separate zonal harmonics of the terms in these equations. This will allow us to consider each zonal harmonic independently, and also allow computation of the zonal derivatives, reducing the dimensionality of the problem. This means that we consider the perturbation zonal wind, meridional wind and temperatures as a sum of Fourier components in the zonal direction, e.g., $u' = \Re[\sum_m u'_m(y, z)e^{im\theta}]$ with similar expressions for v' and T'. In this case, $u'_m(y, z)$ is the (complex-valued) amplitude of the m zonal harmonic of the perturbation zonal wind. With this definition, we can substitute for derivatives in the x direction using $\frac{\partial \Psi}{\partial x} = \frac{im}{a\cos\phi}\Psi_m$.

Breaking the analysis down by zonal harmonic, and rewriting the above coupled equations into a simpler matrix form yields:

$$\begin{bmatrix} 1 & A \\ E & 1 \end{bmatrix}\begin{bmatrix} \frac{\partial u'_m}{\partial \ln P} \\ \frac{\partial v'_m}{\partial \ln P} \end{bmatrix} = \begin{bmatrix} B & C \\ F & G \end{bmatrix}\begin{bmatrix} u'_m \\ v'_m \end{bmatrix} + \begin{bmatrix} D\frac{\partial T'_m}{\partial y} \\ HT'_m \end{bmatrix}, \tag{A.5}$$

where

$$A = \frac{im}{a\cos\phi}\bar{U}\Big/\left(f + 2\bar{U}\frac{\tan\phi}{a}\right),$$

$$B = -2\frac{\tan\phi}{a}\frac{\partial \bar{U}}{\partial \ln P}\Big/\left(f + 2\bar{U}\frac{\tan\phi}{a}\right),$$

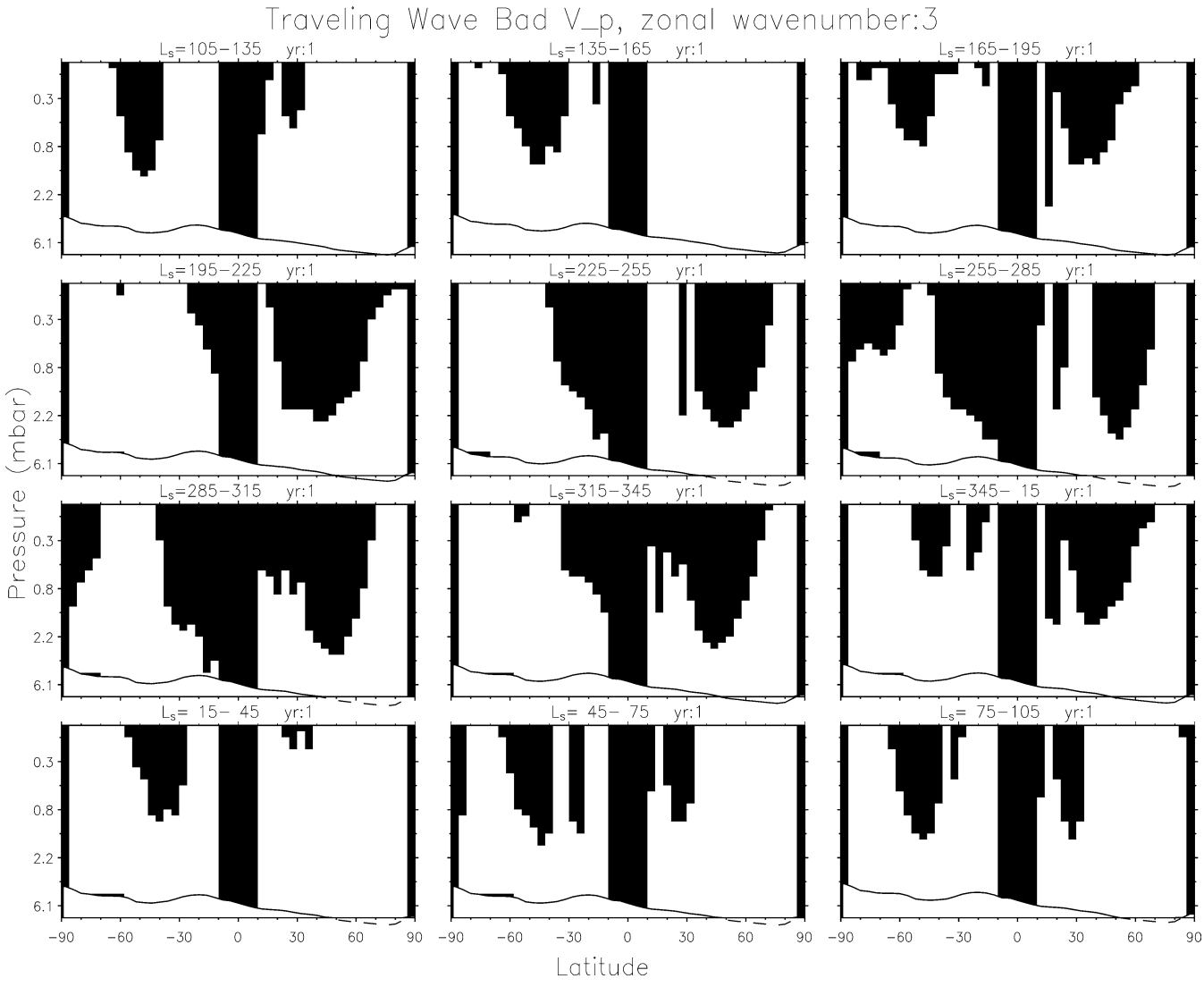

Fig. 28. Latitude-height cross sections with season of the regions in which we were able to solve for the $m = 3$ perturbation winds for the first MGS mapping year. The structure of this plot is the same as many preceding plots. White regions are those in which the perturbation winds could be estimated. Black regions lie on or above a region in which our perturbation wind estimation algorithm broke down. The excluded regions are excessive for $m = 3$, but much less bad for $m = 1$.

$$C = \frac{-im}{a\cos\phi}\frac{\partial\bar{U}}{\partial\ln P}\Big/\left(f + 2\bar{U}\frac{\tan\phi}{a}\right),$$

$$D = R\Big/\left(f + 2\bar{U}\frac{\tan\phi}{a}\right),$$

$$E = \frac{-im}{a\cos\phi}\bar{U}\Big/\left(f - \frac{\partial\bar{U}}{\partial y} + \bar{U}\frac{\tan\phi}{a}\right),$$

$$F = \frac{im}{a\cos\phi}\frac{\partial\bar{U}}{\partial\ln P}\Big/\left(f - \frac{\partial\bar{U}}{\partial y} + \bar{U}\frac{\tan\phi}{a}\right),$$

$$G = \left(\frac{\partial^2\bar{U}}{\partial\ln P\,\partial y} - \frac{\tan\phi}{a}\frac{\partial\bar{U}}{\partial\ln P}\right)\Big/\left(f - \frac{\partial\bar{U}}{\partial y} + \bar{U}\frac{\tan\phi}{a}\right),$$

$$H = \frac{-im}{a\cos\phi}R\Big/\left(f - \frac{\partial\bar{U}}{\partial y} + \bar{U}\frac{\tan\phi}{a}\right).$$

This matrix equation can be solved for $\frac{\partial u'_m}{\partial\ln P}$ and $\frac{\partial v'_m}{\partial\ln P}$ as functions of u'_m, v'_m, T'_m, and $\frac{\partial T'_m}{\partial y}$:

$$\frac{\partial u'_m}{\partial\ln P} = \frac{1}{1-AE}\left[(B-AF)u'_m + (C-AG)v'_m\right] + \frac{1}{1-AE}\left[D\frac{\partial T'_m}{\partial y} - AHT'_m\right], \tag{A.6}$$

$$\frac{\partial v'_m}{\partial\ln P} = \frac{1}{1-AE}\left[(F-EB)u'_m + (G-CE)v'_m\right] + \frac{1}{1-AE}\left[HT'_m - ED\frac{\partial T'_m}{\partial y}\right]. \tag{A.7}$$

If we then integrate these equations up from an assumed perturbation wind at the surface, we have a solution for each zonal harmonic of the perturbation winds consistent with the gradient wind approximation for the zonal mean zonal

wind. Unfortunately, there are several cases where this approach can fail. The first is if the determinant on the left of (5) is zero, i.e., $1 - AE = 0$. In this case, the two coupled equations are degenerate, and we do not have enough information to separate them. The second possibility is that the denominator in A, B, C, and D goes to zero, and these coefficients blow up, i.e., $f + 2\bar{U}\tan\phi/a = 0$. This is the equivalent of the problem with geostrophy near the equator, in this case it is the Coriolis and curvature terms that are canceling each other out and leaving the winds without a balanced solution. The third possibility is much like the second, but where the denominator in E, F, G, and H goes to zero, i.e., $f - \partial\bar{U}/\partial y + \bar{U}\tan\phi/a = 0$. In this case, the Coriolis, curvature and inertia terms all cancel, leaving the perturbations without a balanced solution. We have considered cases where the determinant is less than 0.72 or the absolute value of either denominator is less than $2\Omega\sin(10°)$ to be bad. Empirically, these limits seem to minimize the effects of the ill-defined solution regions for the perturbation winds.

The combined effects of these problematic conditions for solution of the perturbation winds are greater for the higher zonal harmonics. They are a nuisance for the $m = 1$ case, but devastating to the $m = 3$ case (see Fig. 28). For this reason, we do not present solutions for the perturbation winds except for the $m = 1$ cases. Even for those, we carefully indicate the regions where this algorithm breaks down. To enhance the readability of our figures, we have horizontally interpolated across regions where the algorithm breaks down. This is a reasonable approximation to the winds for small gaps, but in general the results in these regions are of unknown accuracy.

References

Allison, M., DelGenio, A.D., Zhou, W., 1994. Zero potential vorticity envelopes for the zonal-mean velocity of then Venus, Titan atmospheres. J. Atmos. Sci. 51, 694–702.

Andrews, D.G., Holton, J.R., Leovy, C.B., 1987. Middle Atmospheric Dynamics. Academic Press, San Diego. 489 p.

Banfield, D., Conrath, B.J., Smith, M.D., Christensen, P.R., Wilson, R.J., 2003. Forced waves in the martian atmosphere from MGS TES nadir data. Icarus 161 (2), 319–345.

Barnes, J.R., 1980. Time spectral analysis of midlatitude disturbances in the martian atmosphere. J. Atmos. Sci. 37, 2002–2015.

Barnes, J.R., 1981. Midlatitude disturbances in the martian atmosphere: a second Mars year. J. Atmos. Sci. 38, 225–234.

Barnes, J.R., 1984. Linear baroclinic instability in the martian atmosphere. J. Atmos. Sci. 41, 1536–1550.

Barnes, J.R., Pollack, J.B., Haberle, R.M., Leovy, C.B., Zurek, R.W., Lee, H., Schaeffer, J., 1993. Mars atmospheric dynamics as simulated by the NASA Ames general-circulation model 2. Transient baroclinic eddies. J. Geophys. Res. 98, 3125–3148.

Barnes, J.R., Haberle, R.M., Pollack, J.B., Lee, H., Schaeffer, J., 1996. Mars atmospheric dynamics as simulated by the NASA Ames general circulation model. 3. Winter quasi-stationary eddies. J. Geophys. Res. 101, 12753–12776.

Blumsack, S.L., Gierasch, P.J., 1972. Mars: the effects of topography on baroclinic instability. J. Atmos. Sci. 29, 1081–1089.

Briggs, G.A., Leovy, C.B., 1974. Mariner 9 observations of the Mars north polar hood. Bull. Am. Met. Soc. 55, 278–296.

Collins, M., Lewis, S.R., Read, P.L., Hourdin, F., 1996. Baroclinic wave transitions in the martian atmosphere. Icarus 120, 344–357.

Conrath, B.J., 1981. Planetary-scale wave structure in the martian atmosphere. Icarus 48, 246–255.

Conrath, B.J., Pearl, J.C., Smith, M.D., Maguire, W.C., Christensen, P.R., Dason, S., Kaelberer, M.S., 2000. Mars Global Surveyor Thermal Emission Spectrometer (TES) observations: atmospheric temperatures during aerobraking and science phasing. J. Geophys. Res. 105, 9509–9519.

Gill, A.E., 1982. Atmosphere–Ocean Dynamics. Academic Press, San Diego. 662 p.

Haberle, R.M., Pollack, J.B., Barnes, J.R., Zurek, R.W., Leovy, C.B., Murphy, J.R., Lee, H., Schaeffer, J., 1993. Mars atmospheric dynamics as simulated by the NASA Ames general circulation model 1. The zonal-mean circulation. J. Geophys. Res. 98, 3093–3123.

Hess, S.L., 1950. Some aspects of the meteorology of Mars. J. Meteorol. 7, 1–13.

Hinson, D.P., Wilson, R.J., 2002. Transient eddies in the southern hemisphere of Mars. Geophys. Res. Lett. 29. doi:10.1029/20011GL014103.

Hinson, D.P., Wilson, R.J., Smith, M.D., Conrath, B.J., 2003. Stationary planetary waves in the atmosphere of Mars during southern winter. J. Geophys. Res. 108. #5004.

Hollingsworth, J.L., Barnes, J.R., 1996. Forced stationary planetary waves in Mars's winter atmosphere. J. Atmos. Sci. 53, 428–448.

Hourdin, F., Forget, F., Talagrand, O., 1995. The sensitivity of the martian surface pressure and atmospheric mass budget to various parameters—a comparison between numerical simulations and Viking observations. J. Geophys. Res. 100, 5501–5523.

Leovy, C.B., 1969. Mars: theoretical aspects of meteorology. Appl. Optics 8, 1279–1286.

Leovy, C., Mintz, Y., 1969. Numerical simulation of the atmospheric circulation and climate of Mars. J. Atmos. Sci. 26, 1167–1190.

Leovy, C.B., 1979. Martian meteorology. Annu. Rev. Astron. Astrophys. 17, 387–413.

Michelangeli, D.V., Zurek, R.W., Elson, L.S., 1987. Barotropic instability of midlatitude zonal jets on Mars, Earth and Venus. J. Atmos. Sci. 44, 2031–2041.

Murphy, J.R., Leovy, C.B., Tillman, J.E., 1990. Observations of martian surface winds at the Viking Lander-1 site. J. Geophys. Res. 95, 14555–14576.

Pedlosky, J., 1979. Geophysical Fluid Dynamics. Springer-Verlag, New York. 710 p.

Pollack, J.B., Leovy, C.B., Greiman, P.W., Mintz, Y., 1981. A martian general circulation experiment with large topography. J. Atmos. Sci. 38, 3–29.

Ryan, J.A., Henry, R.M., Hess, S.L., Leovy, C.B., Tillman, J.E., Walcek, C., 1978. Mars meteorology—3 seasons at surface. Geophys. Res. Lett. 5, 715–718.

Salby, M.L., 1982. Sampling theory for asynoptic satellite-observations 2. Fast Fourier synoptic mapping. J. Atmos. Sci. 39, 2601–2614.

Schofield, J.T., Barnes, J.R., Crisp, D., Haberle, R.M., Larsen, S., Magalhaes, J.A., Murphy, J.R., Seiff, A., Wilson, G., 1997. The Mars Pathfinder atmospheric structure investigation meteorology (ASI/MET) experiment. Science 278, 1752–1758.

Smith, M.D., Pearl, J.C., Conrath, B.J., Christensen, P.R., 2001a. Thermal Emission Spectrometer results: Mars atmospheric thermal structure and aerosol distribution. J. Geophys. Res. 106, 23929–23945.

Smith, M.D., Conrath, B.J., Pearl, J.C., Christensen, P.R., 2001b. Thermal Emission Spectrometer observations of martian planet-encircling dust storm 2001A. Icarus 157, 259–263.

Tillman, J.E., Henry, R.M., Hess, S.L., 1979. Frontal systems during passage of the martian north polar hood over the Viking Lander 2 site period to the first 1977 dust storm. J. Geophys. Res. 84, 2947–2955.

Wilson, R.J., Banfield, D., Conrath, B.J., Smith, M.D., 2002. Traveling waves in the northern hemisphere of Mars. Geophys. Res. Lett. 29. #1684.